PETROLEUM RESEARCH JOURNAL

TECHNICAL PAPERS

ENGINEERING

Restriction conditions in well log interpretation ..... *G. Szigeti* 1

The effects of WAG process on the areal sweep efficiency .....
A.Y. Zekri and S.K. El Mabrouk 9

Failure investigation of weld joint between Manurite 36X and Incology 800H tubes in ethylene plant cracking furnace .....
M.L. Mahta and A.T. Hassan 18

EXPLORATION

Comparison: Semblance spectra and velocity function techniques of velocity analysis ..... *M.M. Elazezi* 32

Hilbert transform and image sharpening techniques as a tool of interpreting 3-D potential field (Gravity) data ..... *A.M. Ushah* 44

Seismic confirmation of a new tectonic element, south-central Sirt basin Libya ..... *M.M. Elazezi and R.N. Sinha* 52

Remote sensing as a tool to study the geology of the northeastern part of Tibesti Mountain, Libya ..... *K.M. Abdulnasser* 67

Reservoir quality analysis—An overview with examples from the Sirt Basin ..... *R.C. Thom* 75

CHEMISTRY

Bioremediation of terestrial fuel spills .....
I. Ahmad, M. Gaja and N. Kumar 85

SHORT NOTES

Effect of the gravity sedimentation and chemical precipitation on the concentration of heavy metals in the refinery effluent .....
M.A. Khawaja, M.N. Oun and S. Alosta 91

ABSTRACTS

Of papers presented at the First Symposium, Sedimentary Basins of Libya, Geology of Sirt Basin, Tripoli, G.S.P.L.A.J.
10–13 October, 1993. 96

VOLUME 6–1994

Petroleum Research Centre
P.O. Box 6431 Tripoli
Great Socialist People's Libyan Arab Jamahiriya

PRJ, Vol. 6 (January 1994); P. 1–8, 5 FIGS, 3 TABLES.

RESTRICTION CONDITIONS IN WELL LOG INTERPRETATION

G. Szigeti*

الظروف المقيدة لاستقراء سرود الآبار

ج. زيقيتي

عند مقارنة السرود المقاسة والمستنبطة في عملية الاستقراء لا بد وأن تستوفى معايير الصخور بعض الظروف المحددة.

تبين هذ الورقة كيفية تناول الظروف المقيدة بحصر التعريف في نطاق صلب محذب (متعدد السطوح) على رقعة مساحية كبيرة. وتقدم هذه الورقة حلا رياضيا ولوغارتميا للتقليل من عدم الترابط بين مجموعتين من السرود على هذا النطاق الصلب المحدب.

وتثبت الدراسة صحة عملية التقليل هذه وتوضحها على مثال هندسي حي كما توصف أسس التجسيم الحاسوبي للوغارتم. كذلك تم تبيان الظروف المقيدة المختلفة للإستقراد بالصخور الجرانيتية.

ABSTRACT

In comparing the measured and response logs during the process of complex well log interpretation, the parameters of the rock model must fulfill certain restriction conditions.

The present paper shows how the different types of restriction conditions can be handled by constraining the domain of definition on a convex solid (Polyhedron) of higher dimensional space. The paper offers and realizes complete mathematical and algorithmic solution for the minimization of incoherency between the two set of logs on this convex solid. The paper proves the correctness of the process of minimization, demonstrates it on a vivid, geometrical example and describes the basic concepts of computer realization of the algorithm.

Application of different restriction conditions for an interpretation in granite rock is also given.

INTRODUCTION

One of the main aspects of the complex well log interpretation is the comparison of the measured logs and the response logs. The latter one is created by the log analyst on the basis of geological, petrophysical knowledge using the rock model of the area and the response functions of the measurements. The aim of the comparison is the determination of the parameters of the rock model.

The parameters undergo certain restrictions such as any fraction of unit volume is between zero and one. For most wells and for most log intervals when we have a successful trial of methodology, instrument and interpretation, these restrictions are fulfilled automatically (i.e. without any special mathematical arrangement during the process of minimization of the difference between measured and theoretical logs). After all, if because of the erroneous character of the measurements or because of approximate character of rock model the result of minimization breaks the restrictions it does not necessarily mean that the given field material could not be explained on the basis of the used rock model. This question finally must be judged on the basis of the measure of incoherency between the two quantities. The aim of the computerized interpretation should be to gain all the useful information from the field material. That is why in the case of the above mentioned difference we

*Petroleum Research Centre, P.O. Box 6431, Tripoli, G.S.P.L.A.J.

have to form and solve a more special mathematical minimization task.

From purely mathematical point of view the task elaborated in the present paper is the minimization of a quadratic function on a convex body of k-dimensional Euclidian space, where the body is a polihedron, convex hull of a finite point set. The offset of the existing unique minimum is to be found by the aid of a series of projections of different dimensions. With growing k, the number of projections that might be necessary grows very fast in a non polynomial order.

In bore hole geophysics we have only a limited number of adequate logs, thus the number of parameters to be determined could not be too high. Consequently there is a strict connection between the applied mathematical solution and the geophysical task: our algorithm is fully applicable, even in a relatively modest computer, until four, five, six unknowns, which cover the needs of loganalysts. This is, definitely, inapplicable if the number of unknowns is more than ten. On this price we get a rather exact solution of the problem of restrictions without the necessity of introducing penalty term containing subjective construction.

TYPE OF RESTRICTIONS

Suppose we have m different measured log values at a given fixed depth point, each one is normalized by its own standard deviation, $\boldsymbol{b}^{\mathrm{T}}=(b_1, b_2, \ldots, b_m)$, and suppose that we have already accepted that our rock model consists of one fluid and k solid unknown components $\boldsymbol{x}^{\mathrm{T}}=(x_0, x_1, \ldots, x_k)$, where $k \leqslant m$ and $\boldsymbol{x}^{\mathrm{T}}$ is the transposed row vector of the column vector $\boldsymbol{x}$. We approach each tool response function in a linear form using the normalized, zone parameter matrix A having m rows and $k+1$ columns.

Our aim is to find the parameter vector $\boldsymbol{x}$ for which $A \cdot \boldsymbol{x}$ is the possible closest to the measured vector $\boldsymbol{b}$ on the set of Euclidian space $Q \subset \mathbb{R}^{k-1}$:

$$\hat{x}_Q=\{\boldsymbol{x} \in Q \mid \| \boldsymbol{b}-A\boldsymbol{x} \|^2 \rightarrow \min\}, \tag{1}$$

where $\| \ \|^2$ is the square of the distance in the $\mathbb{R}^m$ vector space.

The simplest condition for the set Q is given by the material balance equation according to which the sum of all the components is unity (we involve this equation into the definition of set Q instead of adding one more term to the function to be minimized, because by this way we fulfill the material balance equation exactly and not only approximately).

We speak about interpretation *without restrictions* if we define set Q as

$$Q=Q_{nr}=\{\boldsymbol{x} \in \mathbb{R}^{k+1} \mid x_0+x_1+\cdots+x_k=1\} \tag{2}$$

Definition (2) does not guarantee that all x_i are positive, or x_i are less than one, i.e. $O \leqslant x_i \leqslant 1$ is not necessarily valid for all x_i. If we prescribe together with the material balance equation that $O \leqslant x_i$ for $i=0, 1, \ldots, k$ then it trivially follows that $x_i \leqslant 1$ $(i=0, 1, \ldots, k)$, thus we speak about *logical restrictions* when we define Q as

$$Q=Q_{lr}=\left\{\boldsymbol{x} \in \mathbb{R}^{k+1} \,\middle|\, \begin{array}{l} O \leqslant x_i, (i=0, 1, \ldots, k) \\ x_0+x_1+\cdots+x_k=1 \end{array}\right\} \tag{3}$$

It should be noted here, that if we project points of Q_{lr} to the $(O, x_1, x_2, \ldots, x_k)$ hyperplane of $\mathbb{R}^{k+1}$, then the projection is the k-dimensional simplex of the $(x_1', x_2', \ldots, x_k')$ $\mathbb{R}^k$ space, given by the points $P_0=(0, 0, \ldots, 0)$; $P_1=(1, 0, 0, \ldots, 0)$; …; $P_k=(0, 0, \ldots, 1)$. This projection allows inversion in the form $x_0=1-x_1'-x_2', \ldots, -x_k'$; $x_1=x_1'$; $x_2=x_2'$; …; $x_k=x_k'$, and in this sense we say that Q_{lr} is a k-dimensional simplex (embedded into the $k+1$-dimensional space).

In definition (3) of Q_{lr} we speak about logical restrictions, because this allows to change x_i in the wider logically possible interval. Another situation is when e.g. from core lab data we can prescribe more strict limits for certain components x_i. In connection with this, we speak about *geological restrictions* if we define Q as

$$Q=Q_{gr}=\left\{\boldsymbol{x} \in \mathbb{R}^{k+1} \,\middle|\, \begin{array}{l} a_i \leqslant x_i \leqslant b_i, (O \leqslant a_i < b_i \leqslant 1), \\ (i=0, 1, \ldots, k) \\ x_0+x_1+\cdots+x_k=1 \end{array}\right\} \tag{4}$$

First we notice that definition (4) contains no contradiction, i.e. set Q_{gr} is nonempty, if and only if

$$\sum_{i=0}^{k} a_i \leqslant 1 \quad \text{and} \quad 1 \leqslant \sum_{i=0}^{k} b_i \tag{5}$$

Second let's examine again the $\boldsymbol{x}=(x_0\, x_1, \ldots, x_k) \rightarrow (O, x_1, x_2, \ldots, x_k)=(x_1', x_2', \ldots, x_k')=\boldsymbol{x}'$ projection of the set Q_{gr}. Denoting the projection of Q_{gr} by Q_{gr}', it is not difficult to realize that Q_{gr}' can be represented in the following form:

$$Q_{gr}'=T_k \cap H_{1-b_0, 1-a_0}, \tag{6}$$

where

$$T_k=\{\boldsymbol{x}' \in \mathbb{R}^k \mid a_i \leqslant x_i' \leqslant b_i, (i=1, 2, \ldots, k)\}, \tag{7}$$

$$H_{c,d}=\left\{\boldsymbol{x}' \in \mathbb{R}^k \mid c \leqslant \sum_{i=1}^{k} x_i' \leqslant d\right\} \tag{8}$$

which means that Q_{gr}' is the intersection of the k-dimensional rectangular parallelepiped T_k and the

$H_{c,d}$ strip like domain $\mathbb{R}^k$ (domain bounded by two parallel hyperplanes) with parameters $c=1-b_0$, $d=1-a_0$. Figure 1 demonstrates different possible Q'_{gr} restriction sets for the $k=2$ dimensional case, when we have two solid components in our rock model.

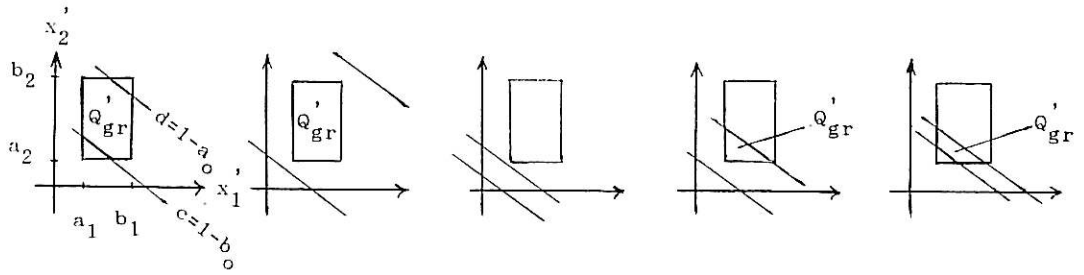


FIG. 1. Different restriction sets for two solid components model.

The projection above allows inversion in the form $x'=(x'_1, x'_2, \ldots, x'_k)\to(1-\Sigma_{i=1}^{k} x'_i, x'_1, x'_2, \ldots, x'_k)=(x_0, x_1, \ldots, x_k)=x$ and in this sense we say that Q_{gr} is a k-dimensional polyhedron (embedded into the $k+1$ dimensional space).

It is not difficult to realize, that Q_{nr}, Q_{lr} and Q_{gr} are convex sets, i.e. from $x_0, x_1 \in Q$ it follows that $\alpha x_0+(1-\alpha)x_1 \in Q$ for any $0\leqslant\alpha\leqslant 1$.

During the process of minimization a pivotal point is the characterization of the Q sets by his vertexes, i.e. representation of Q as the convex hull $\kappa(P_1, P_2, \ldots, P_n)$, which is the narrowest convex set containing all the P_i points. For Q_{nr} this representation is not possible and not necessary, for Q_{lr} we have already described the vertexes of the simplex. Let's find the vertexes of the Q_{gr} set. As the representation (6) of Q_{gr} shows in order to reach this aim we have to examine whether the jth edge of the rectangular parallelepiped T_k is completely inside, completely outside or intersects once or twice the strip $H_{1-b_0,1-a_0}$. The only difficulty at this stage is to create an algorithm, which runs over all the edges of the rectangular parallelepiped.

For the sake of simplicity let's examine instead of block T_k the equivalent in this respect to the unit cube. The k-dimensional unit cube has $k\cdot 2^{k-1}$ edges, and two peak points of the cube are connected by edge if and only if there is exactly one coordinate where the two peak points differ. Figure 2 shows the edge system of the unit cube of $\mathbb{R}^4$. Ordering the peak points of Fig. 2 from up to down and if the two points are on the same level then from left to right and directing edges from the smaller to the higher points, i.e. $\overrightarrow{P_iP_j}$ is directed edge if $\overrightarrow{P_iP_j}$ is edge and $P_i<P_j$, we can order the edges by stating $\overrightarrow{P_iP_j}<\overrightarrow{P_lP_k}$ if $P_i<P_l$ or in the case $P_i=P_l$ if $P_j<P_k$.

The n value in the $\kappa(P_1, P_2, \ldots, P_h)$ representation of Q_{gr} depends on the a_i, b_i values of definition (4). It is not difficult to prove that the possible maximum value for n is $n_{\max}=2^k+2\cdot k-2$, while for the simplex Q_{lr} evidently $n_{\max}=k+1$. The comparison of these two expressions of $n_{\max}$ explains how more complicated the task becomes for the case of geological restrictions, and the reason for restricting our solution to lower dimensions.

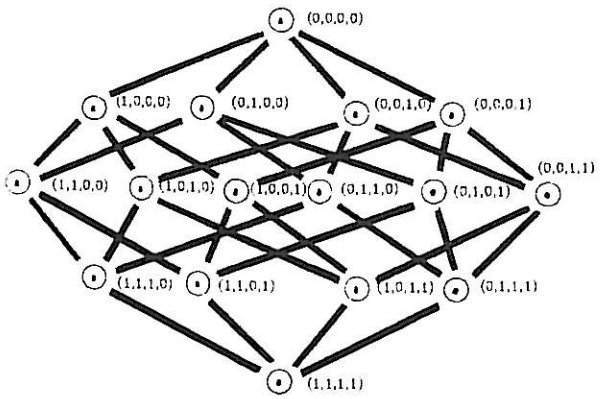


FIG. 2. Edge system of unit cube of four dimensional Euclidian space.

In their study (Mayer and Sibit, 1980) [1] introduced other nonlinear restrictions (constraints) as well. Comparing the technique of the present paper to that of [1], we notice that even thought the method described in this paper can only be applied to linearized restrictions, it is not necessary to introduce a second term in expression (1) which contains subjective parameters.

ALGORITHM OF MINIMIZATION

Our aim is to minimize the quadratic function in expression (1) on the set $Q=\kappa(P_1, P_2, \ldots, P_n)$ which is a convex hull of points $P_i \in \mathbb{R}^k$.

In the three-dimensional space we know that a convex solid is surrounded by two-dimensional polygons, by one dimensional edges and by the zero-dimensional P_i points itself. For the sake of conciseness of description of our algorithm, we state that Q has a three-dimensional surrounding solid as well, namely itself. For example any tetrahedron of $\mathbb{R}^3$ surrounded by the tetrahedron itself, by four triangles, by six edges, and by its four vertices (peak points). This complete system of surrounding

configurations we refer as system of boundary hyperplane configurations.

Similar construction can be done in the Euclidian spaces of higher dimension. Basic concepts of this construction are that of the linear algebra and the rank concept of matrices, see e.g. [2]. The exact mathematical construction is reported in [3]. A computer program has been developed to find the system of boundary hyperplane configurations of the $\kappa(P_1, P_2, \ldots, P_n) \subset \mathbb{R}^k$ convex solid. We have checked the result of the program for a number of two- and three-dimensional solids, for the cubes and simplexes of higher dimensions, since these are the bodies for which the results are known from theoretical consideration. For example the system of boundary hyperplane configuration of the unit cube of space $\mathbb{R}^4$ consists of the cube itself, 8 pieces three-dimensional (ordinary) cubes, 24 pieces of squares, 32 sections, and 16 peak points. This is the result of the computer program but it can be proved theoretically as well or, in principle, it can be checked directly from Fig. 2.

Knowing the complete system of boundary hyperplane configurations of the convex solid we can describe the algorithm of the minimization. First we note that if matrix A in expression (1) is not singular on the Q set, then the system of boundary hyperplane configuration of Q preserves its structure after the $AQ=\{Ax \mid x \in Q\}$ injection of Q into the space of normalized measurements $\mathbb{R}^m$. Secondly, we know, as the result of convex analysis, that our quadratic function has one and only one minimum value on a convex body, in other words $\hat{x}_Q$ of expression (1) consists of one and only one point.

Now let us study together with each element of the boundary hyperplane configuration the hyperplane of this configuration, i.e. the smaller dimensional translated linear subset of the $\mathbb{R}^m$ space which contains the whole configuration. On this plane we can divide the points of the given configuration into inner and boundary points. Let us state that the zero dimensional P_i peak point's interior is the P_i point itself. Then by finding the interior of every configuration of the AQ convex solid, we create the division of the convex solid AQ into disjoint sets. In this way, from the relation $Ax_Q \in AQ$, it follows that $A\hat{x}_Q$ is an element of the interior of one and only one configuration.

Now, let us study the following algorithm. We project the measured vector $\boldsymbol{b}$ of (1) for all the boundary hyperplane. If the projection, related to the given hyperplane configuration, is outer point or boundary point then we drop this point. Let us denote the set of projections of $\boldsymbol{b}$, if the projected point turned to be inner related to the jth hyperplane configuration by $\{\boldsymbol{b}_j, j \in J\}$, where J is an index set of the configurations. Note that for any zero-dimensional hyperplane the projection of $\boldsymbol{b}$ is P_i, that is an inner point, thus the J set is nonempty, $i \in J$.

Let us suppose that $A \cdot \hat{x}_Q$ belongs to the interior of the configuration enumerated by index $j_0 \in J$. Projecting $\boldsymbol{b}$ to this hyperplane, the projection $\boldsymbol{b}_{j_0}$ is also in the interior of the configuration, otherwise the intersection of the section $[A \cdot \hat{x}_Q, \boldsymbol{b}_{j_0}]$ and the boundary of the j_0th configuration is closer to $\boldsymbol{b}$ than $A \cdot \hat{x}_Q$, which is in contradiction to the definition of $\hat{x}_Q$ of (1). Because $\boldsymbol{b}_{j_0}$ is in the interior of the j_0th configuration, so $A\hat{x}_Q = \boldsymbol{b}_{j_0}$. The j_0 index is not known in advance, but we can choose it easily from the set of those projections where $\boldsymbol{b}_j$ is inner point, getting in this way the solution of minimization problem (1) in the form

$$A \cdot \hat{x}_Q = \{\boldsymbol{b}_j; j \in J \mid \| \boldsymbol{b} - \boldsymbol{b}_j \|^2 \to \min\} \tag{9}$$

A is not singular on the set Q, thus the mapping of Ax allows inversion on the set $\{A \cdot x \mid x \in Q\} \subset \mathbb{R}^m$, therefore knowing point $A\hat{x}_Q$ we easily find $\hat{x}_Q$ itself.

The algorithm above is correct and complete, but we can speed it up considerably by the following additional considerations. If we find that the projection of $\boldsymbol{b}$ for the jth boundary hyperplane configuration is inner, then it is meaningless to project $\boldsymbol{b}$ for any further configuration which is a part of the jth configuration. Because in this case the further projection necessarily gives a higher distance, as the minimum in a subset of a set is not lower (in the given case definitely higher) than the minimum on the set itself. This observation also means that we organize the order of projections not arbitrarily, but going from the higher to the lower dimensions. For example if the first projection of $\boldsymbol{b}$ to the k-dimensional hyperplane of AQ configuration turns to be inner, then we can finish the process, because all the other (lower dimensional) hyperplane configurations are parts of the complete body, consequently this first projection gives the $A \cdot \hat{x}_Q$ point. This will be the more frequent case if the field material and theoretical curves fit each other, especially working with logical restrictions Q_{lr}.

To illustrate the work of the algorithmic steps let us study the situation below designed for simple but substantial geometrical presentation. Let $k=m=3$ the normalized measured vector $\boldsymbol{b}=(-\frac{1}{4}, -\frac{1}{4}, -\frac{1}{4})$, and consider the logical restrictions $Q_{lr} \subset \mathbb{R}^4$ defined by the conditions

$$\begin{aligned} &x_0+x_1+x_2+x_3=1, \\ &x_i \geqslant 0, (i=0,1,2,3) \end{aligned} \tag{10}$$

Projecting Q_{lr} for the $x=(O, x_1, x_2, x_3)=(x_1', x_2', x_3') \subset \mathbb{R}^3$ hyperplane we get Q_{lr}' by the inequations

$$\begin{aligned} &x_1'+x_2'+x_3' \leqslant 1, \\ &x_i' \geqslant 0, (i=1,2,3) \end{aligned} \tag{11}$$

and there is a one-to-one correspondence between Q_{lr} and Q'_{lr}. The inequation system (11) indicates that Q'_{lr} is a tetrahedron, the convex hull of the $P_0=(0,0,0)$; $P_1=(1,0,0)$; $P_2=(0,1,0)$; $P_3=(0,0,1)$ points, $Q'_{lr}=\kappa(P_0,P_1,P_2,P_3)$. Now, for the aim of getting a vivid geometrical picture let us choose matrix A in the form

$$A=\begin{pmatrix}0&1&0&0\\0&0&1&0\\0&0&0&1\end{pmatrix}, \tag{12}$$

which is nonsingular on Q_{lr} and on the $x_0+x_1+x_2+x_3=1$ hyperplane. In this case AQ_{lr} is completely identical with Q'_{lr}, so our task is to find the nearest point of Q'_{lr} to the $\boldsymbol{b}=(-\frac{1}{4},-\frac{1}{4},-\frac{1}{4})$ point, see Fig. 3. We remark that for a less artificial matrix A than that of (12) the character of the minimization process remains similar.

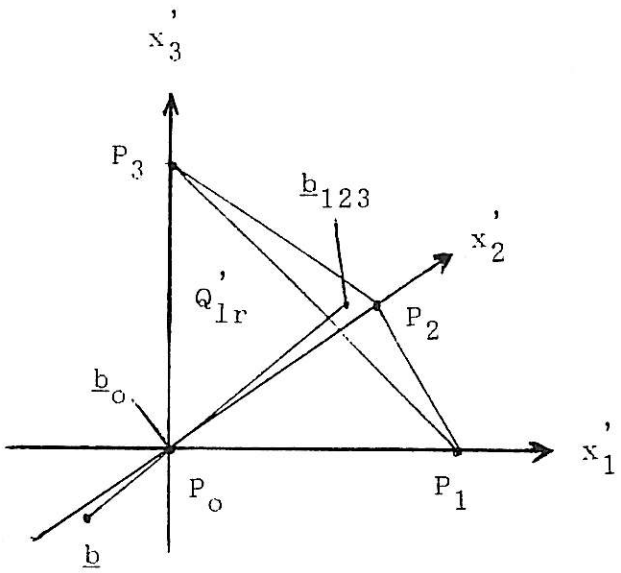


FIG. 3. Geometrical representation of the process of minimization for the case of logical restrictions for three solid components model.

Following our algorithm first we realize, that $\boldsymbol{b}$ is outer point to the tetrahedron $P_0P_1P_2P_3$, thus we have to project $\boldsymbol{b}$ to the four boundary triangles. We found that projection of $\boldsymbol{b}$ is outer to triangles $P_0P_1P_2, P_0P_1P_3, P_0P_2P_3$. Let us denote the projection of $\boldsymbol{b}$ for the $P_1P_2P_3$ triangle by $\boldsymbol{b}_{123}$. Because of symmetry $\boldsymbol{b}_{123}=(\frac{1}{3},\frac{1}{3},\frac{1}{3})$ which is an inner point of the triangle and $\|\boldsymbol{b}-\boldsymbol{b}_{123}\|=1/\sqrt{3}+\sqrt{3}/4$. Now as was pointed out earlier it is needless to project $\boldsymbol{b}$ for the sections P_1P_2, P_1P_3, P_2P_3 and for the points P_1, P_2, P_3 because these boundary configurations are parts of the triangle $P_1P_2P_3$. There is no more two dimensional configurations, so we project $\boldsymbol{b}$ for the sections P_0P_1, P_0P_2, P_0P_3, and we found again that all these projected points are outer related to the given sections. Thus according to our algorithm we project $\boldsymbol{b}$ to the only remaining vertex P_0 and the result of it is trivially $\boldsymbol{b}_0=P_0=(0,0,0)$ with distance $\|\boldsymbol{b}-\boldsymbol{b}_0\|=\sqrt{3}/4$. In this way the set $\{\boldsymbol{b}_j, j\in J\}$ now looks like $\{\boldsymbol{b}_{123},\boldsymbol{b}_0\}$, i.e. consists of two elements. Because $\|\boldsymbol{b}-\boldsymbol{b}_0\|<\|\boldsymbol{b}-\boldsymbol{b}_{123}\|$, thus from (9) we get that the minimum point is $A\hat{x}_Q=\boldsymbol{b}_0=(0,0,0)$, from which using (10) and (12) we get the final result $\hat{x}_Q=(1,0,0,0)$.

As to the computer realization of the algorithm we made the following arrangement. We define a table, each line of which is related to one of the boundary hyperplane configurations, and we associate to each line the so called status variable of logical character, which may have the following values: '*U*' if the projection is Unexamined yet, '*O*' if the result of the projection is Outer, '*I*' if the result of the projection is Inner, and '*N*' if the realization of the projection is Negligible. Using the scheme presented in Table 1, the realization of the algorithm is the following: As initial value we set the status of each line for '*U*'. Then we repeat the only step until there is at least one status '*U*' in the table. This step is to find the higher dimensional line in the table with status '*U*', then project $\boldsymbol{b}$ to the hyperplane associated to that line and decide whether the projection is Inner or Outer. If the status is '*O*' then we drop the result of the projection, if the status is '*I*' then we keep it and we set the status of all sub-configurations for '*N*'. After completing this loop we choose the minimum distance from the lines with status '*I*'. Table 1 is the realization of the algorithm for the geometrical illustration above. The column St_0 denotes the initial status values and actually we made nine projections, thus St_9 is the column where the main loop of our algorithm is ended. In Table 1 we marked with a circle the only two places where we kept the result of projection and we calculated the appropriate distances. Of course for more complicated bodies and for higher dimensions the size of the defined table is extended.

APPLICATION

Let us see the practical consequences of the use of different restriction conditions at the evaluation of volumetric components of a fractured granite rock. The logs involved to the quantitative interpretation are the neutron density, the neutron porosity, the acoustic, the photoelectric index, the thorium and the potassium spectral gamma logs, so in the given case $m=6$. For the sake of accurate porosity estimation we divide the rock matrix for the quartz, the feldspar, the mica and heavy minerals and the pyrite components ($k=4$). The normalizing measure of uncertainty of the logs and the used, slowly changing, parameters

Table 1. Computer Realization of the Process of Minimization for the Case of Fig. 3

$P_0P_1P_2P_3$	Min. value	Min. offset	St_0	St_1	St_2	St_3	St_4	St_5	St_6	St_7	St_8	St_9
1 1 1 1			U	O	O	O	O	O	O	O	O	O
1 1 1 0			U	U	O	O	O	O	O	O	O	O
1 1 0 1			U	U	U	O	O	O	O	O	O	O
1 0 1 1			U	U	U	U	O	O	O	O	O	O
0 1 1 1	$\frac{1}{\sqrt{3}}+\frac{\sqrt{3}}{4}$	$\left(\frac{1}{3},\frac{1}{3},\frac{1}{3}\right)$	U	U	U	U	U	I	I	I	I	I
1 1 0 0			U	U	U	U	U	U	O	O	O	O
1 0 1 0			U	U	U	U	U	U	U	O	O	O
1 0 0 1			U	U	U	U	U	U	U	U	O	O
0 1 1 0			U	U	U	U	U	N	N	N	N	N
0 0 1 1			U	U	U	U	U	N	N	N	N	N
0 1 0 1			U	U	U	U	U	N	N	N	N	N
1 0 0 0	$\sqrt{3}/4$	(0,0,0)	U	U	U	U	U	U	U	U	U	I
0 1 0 0			U	U	U	U	U	N	N	N	N	N
0 0 1 0			U	U	U	U	U	N	N	N	N	N
0 0 0 1			U	U	U	U	U	N	N	N	N	N

are close to that published in [4] with exception of the parameters of the pyrite which in the above order of the logs are (4.07 g/cm^3, −0.03 unit, 38 μsec/foot, 15.77 barn/electron, 2.0 ppm, 0.7%).

For completeness we include to our discussion the following heuristic approximate solution of the problem of logical restrictions (1) and (3) which, as far as we know, is incorporated in many log analyzing programs. This solution consists of two steps. First we calculate as a result of one simple projection the vector solution $\hat{x}_{Q_{nr}}=(x_0, x_1, \ldots, x_k)$ of the problem (1) and (2), then we modify this vector in the following way

$$x_j' = \frac{\max\{0, x_j\}}{\sum_{i=0}^{k} \max\{0, x_i\}}, (j=0, 1, \ldots, k) \tag{13}$$

which means we round the negative components X_i of $\hat{x}_{Q_{nr}}$ for zero and we divide the other components by the sum of positive components in order to fulfill the material balance equation. It is clear that

Table 2. Results of Interpretations under Different Restriction Conditions at a Massive Granite Zone (* denotes that the given value is a boundary value)

9381.	ϕt	Qz	Fp	M&Hm	Pr	INC
Qnr	.0380	.4947	.4359	.0437	-.0123	.309
Pℓr	.0376	.4887	.4306	.0432	.0000*	.458
Qℓr	.0408	.4741	.4577	.0274	.0000*	.399
Qgr	.0452	.4407	.4932	.0009	.0200*	.731

Table 3. Results of Interpretations under Different Restriction Conditions at a Fractured Granite Zone

9397.	ϕt	Qz	Fp	M&Hm	Pr	INC
Qnr	.1292	.7610	-.1480	.1883	.0695	1.55
Pℓr	.1125	.6629	.0000*	.1640	.0606	2.12
Qℓr	.1371	.6507	.0000*	.1223	.0898	1.75
Qgr	.1400	.6062	.0600*	.0959	.0978	1.92

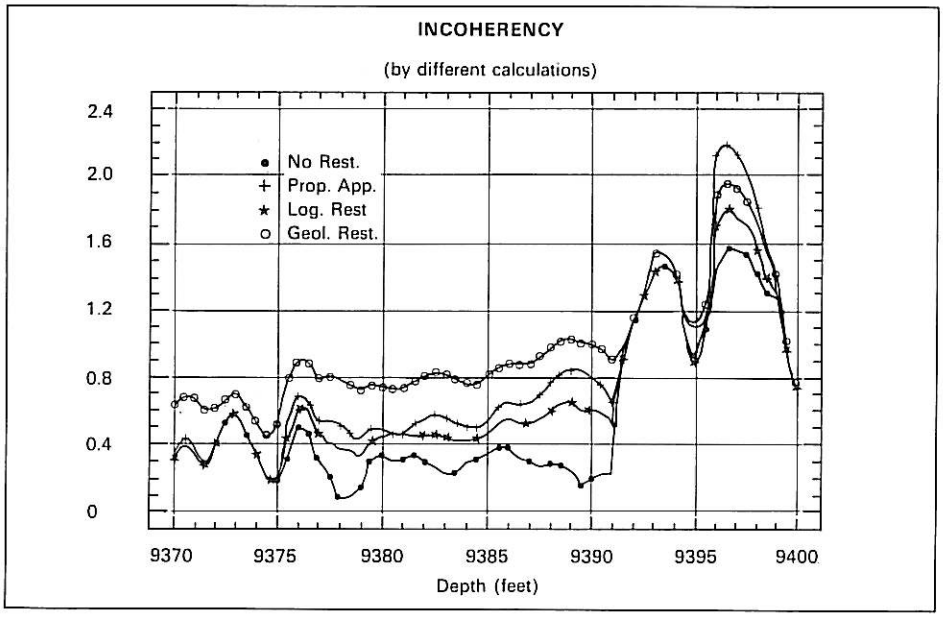


FIG. 4. Incoherency as a function of depth between 9370 and 9400 feet.

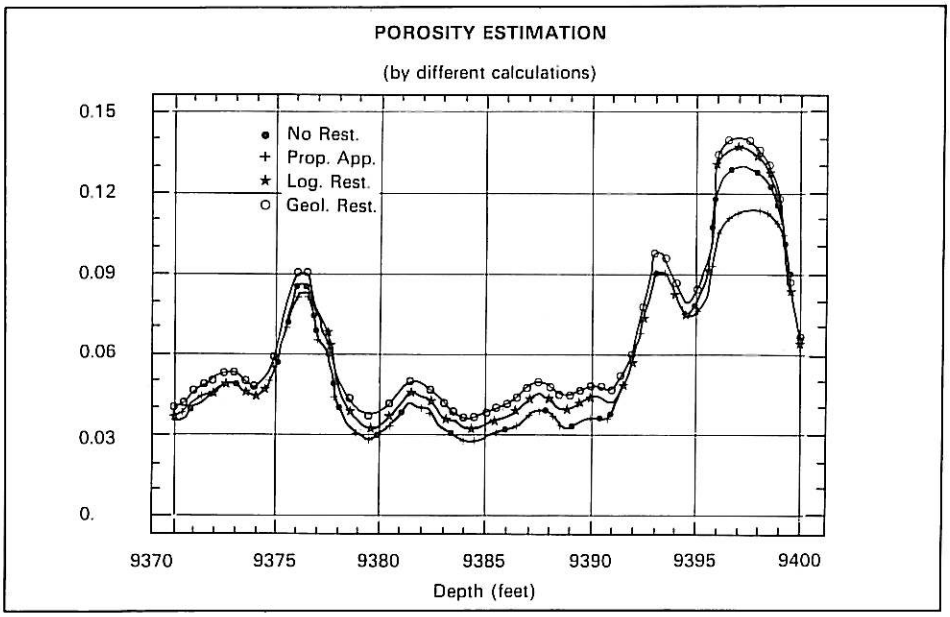


FIG. 5. Porosity estimations on the log section of Fig. 4.

$(x'_0, x'_1, \ldots, x'_k) \in Q_{lr}$, so we denote the modified vector by $x_{P_{lr}}$ and we call it as proportional approximation of problem (1) and (3).

Let us study the result of different interpretations in the granite rock, first at the depth 9381 feet (Table 2). Evidently the no restriction case gives the smallest incoherency $\| b - Ax \|$, but because of the negative pyrite content, $\hat{x}_{Q_{nr}}$ could not be accepted at all, in other words the probability of occurrence of the rock components $\hat{x}_{Q_{nr}}$ is zero. According to formula (13) the modification of $\hat{x}_{Q_{nr}}$ which is the proportional approximation $\hat{x}_{P_{lr}}$ eliminates the negative pyrite content, but necessarily gives a higher incoherency than the exact solution $\hat{x}_{Q_{lr}}$.

The change in the main porosity component is not significant and the interpretation based on any of the four curves in Fig. 5 indicate that we are in the massive granite zone.

Table 3 shows the results at the depth 9397 feet. Here we have a higher negative feldspar component. Because the sum of the positive components is more than one, and because practically we shall not find negative porosity estimation in the solution of the Q_{nr} task, thus the porosity of the proportional approximation is less than the original one. On the other hand the exact porosity estimation offered by $\hat{x}_{Q_{lr}}$ is found to be higher in the present example than that of $\hat{x}_{Q_{nr}}$. This means that

the proportional approximation results could not be considered as a good approximation of the Q_{lr} task (1) and (3). This statement becomes especially clear having in mind that the modifying step is not a function of the matrix A of (1).

Figure 4 shows the incoherency of different calculations on the depth interval 9370–9400 feet. We can see that, with the exception of those intervals where the Q_{lr} restrictions fulfill automatically (e.g. 9370–9375 feet) and consequently $\hat{x}_{Q_{mr}}=x_{P_{lr}}=\hat{x}_{Q_{lr}}$, the decrease in incoherency of $\hat{x}_{Q_{lr}}$ related to $x_{P_{lr}}$ is considerable. In Fig. 5 we can follow the porosity estimations obtained by different calculations. Despite of the considerable changes in incoherency, the porosity shows a relatively stable character, especially in the massive granite intervals. This emphasises again that the porosity is not only the target parameter of the complex well log interpretation but the most robust one. However difference between the porosity estimations of Q_{lr} and P_{lr} is not negligible in the fractured zones and this fact tells about the usefulness of the exact problem solution.

In the case when we have additional information about mineral contents, then we solve the geological restriction task (1) and (4). For example if we know that pyrite content is more than 2% and feldspar content is at least 6%, i.e. $a_5=0.02$ and $a_3=0.06$, while all other limits are zero and one, then we get the results shown in Tables 2 and 3 and the appropriate curves of Figs. 4 and 5. The incoherency belonging to the solution $\hat{x}_{Q_{gr}}$ is necessarily higher (or equal) than that of the $\hat{x}_{Q_{lr}}$. But if this increase is not so dramatic (this is the case at 9397 or 9393 feet), then we should accept this solution, which is in accordance with the geological knowledge of the given area.

CONCLUSION

- Restriction conditions of well log interpretation can be represented or approximated in the form of defining the domain of minimization as a convex solid of a higher dimensional space.
- Rather exact algorithm for the minimization of a quadratic function on a convex solid can be worked out on the basis of elementary projections of different dimensions.
- Application of the exact algorithm reduces the incoherence between measured and theoretical logs and in some fractured zones of granite rock effects for the porosity estimation are considerable.

ACKNOWLEDGEMENT

The author would like to thank Mr. Mustafa Idris, the General Manager of the Petroleum Research Centre for his continuous support.

The author highly acknowledges the rewarding experienced comments and stimulating consultations with Prof. Zoltan Barlai.

REFERENCES

[1] Mayer C., A. Sibit, 1980, Global, A New Approach to Computer Processed Log Interpretation, 55th Annual Conference of Society of Petroleum Engineers, Dallas.

[2] Kuros, A.G., 1959, Kurs Vhysej Algebra [Higher Algebra] (in Russian), Moscow.

[3] Szigeti G., 1993, Algorithm and Computer Program for the Minimization of a Quadratic Function on a Convex Body, Petroleum Research Centre Internal Report, Tripoli, G.S.P.L.A.J.

[4] Szigeti G., 1993, Improvement of the Accuracy of Statistical Well Log Interpretation Using the Material Balance Equation, Petroleum Research Journal, Vol 5, Tripoli. G.S.P.L.J.A.

PRJ, Vol. 6 (January 1994); P. 9–17, 13 FIGS, 7 TABLES.

THE EFFECTS OF WAG PROCESS ON THE AREAL SWEEP EFFICIENCY

A.Y. Zekri* and S.K. El Mabrouk*

تأثير تردد الماء والغاز (WAG) على مساحة الإزاحة الأفقية لطرق الحقن المتجانس

عبد الرزاق يوسف زكري و صابر خالد المبروك

تم استخدام طريقة الحقن المتجانس WAG لزيادة المردود النفطي في عدد من المكامن بالعالم وبنجاح. السبب الرئيسي لاستخدام هذه الطريقة هو زيادة المساحة الأفقية التي يمر من خلالها المزيج مما ينتج عن ذلك تحسين المردود النفطي.

في العادة تجرى التجارب المعملية لتحديد الحجم الأمثل للغاز والماء المراد حقنه حيث يتم المقارنة بين تردد الماء والغاز حسب النسب 1:1 1:2 2:1 لتحديد النسب المثلى.

الهدف الأساسي لهذا العمل هو بحث تأثير تردد الماء والغاز على مساحة الإزاحة الأفقية التي يمر من خلالها الغاز المزيح المستخدم في طرق الحقن المتجانس حيث تم إجراء تجارب معملية باستخدام مجسم يمثل مربع نموذج خماسي.

لقد تم تغيير حجم الماء والغاز بنسب 2:1, 1:2, 1:1 وتم أستنباط ثلاثة معادلات لتقدير مساحة الإزاحة الأفقية التي يغطيها السائل المزيح حسب الحركية للنظام (Mobility).

إن نتائج هذا العمل يمكن استخدامها في برامج طرق التحليل العددي والحسابي لتقدير كفاءة الحقن المتجانس.

ABSTRACT

Miscible flooding using an alternate solvent/water injection process (WAG) is currently being applied for enhanced oil recovery. The main reason of alternating solvent/water is to improve the mobility of the system which will yield better areal sweep efficiency and more reservoir oil contacted by the solvent.

Normally laboratory work is performed to assess or select the optimum WAG process of the miscible flooding system being investigated. The main objective of the laboratory work is to select the process (WAG 1:1, 1:2, or 2:1) which will result in an optimum displacement efficiency.

The purpose of this study is to investigate the effect of various WAG ratios on the areal sweep efficiency. An experimental work was conducted using one-quarter five spot model.

The WAG ratio was varied for specified ratios of 1:1, 1:2, and 2:1. Three equations were obtained to predict the areal sweep as function of mobility ratio for various WAGs. The results of this work could be utilized in performing numerical and analytical miscible models for candidate EOR reservoirs.

*Petroleum Engineering Department, Al Fateh University, Tripoli, G.S.P.L.A.J.

INTRODUCTION

The search for future oil reserves has shifted the efforts of the oil industry to a new and more difficult areas for exploration, in addition to investigate the possibility of new technical means to produce the remaining oil after primary and secondary recovery. Currently various enhanced oil recovery methods are being investigated as possible new techniques for the enhancement of the world oil reserves.

Miscible solvent flooding is the selected EOR process by a number of Libyan oil companies. Volumetric sweep efficiency is the critical parameter effecting the performance of miscible process. Water-alternating solvent process has been proposed to improve the mobility of the miscible flooding system. This results in better sweep efficiency and more oil contacted by the solvent.

Many Authors have studied the five spot pattern because of its wide spread use in secondary and tertiary recovery operations. The effects of fluid mobility ratio on an areal sweep efficiency at breakthrough for an enclosed five-spot pattern has been studied by Ramey [1]. The system was also studied with an electrolytic tank by Check and Menzie [2] using fluid mapper models. Fay and Prats [3], Sheldon and Dougherty [4] employed analytical method, and Bredley, Heller and Odeh [5] using potentiometric models, sweep efficiency results is shown in Table 1. Habermann [6] studied the effects of miscible slug size, 10 to 25 percent hydrocarbon pore volume on oil recovery, keeping the mobility ratio constant. Habermann concluded that at high mobility ratios, a miscible slug of 10 percent hydrocarbon pore volume deteriorates after only a small fraction of the reservoir has been swept. Consequently the rich gas drive process approaches an ordinary gas drive. Mahaffey *et al.* [7] studied the effect of a slug on sweep efficiency utilizing a five spot pattern of a parallel-plate glass model. Mahaffey indicated that the presence of a slug, whose viscosity is intermediate between oil and solvent, increases the sweep efficiency of the oil-solvent system.

Lacy *et al.* [8] published areal sweep out results for a high pressure five-spot model where propane slugs were utilized to displace a methane saturated refined crude oil at 1550 psig. The propane slugs were driven by methane. He concluded that by using LPG slug process, a slug size of 5 percent or less is not effective in increasing oil recovery in horizontal reservoirs. Zekri and Natuh [9] have studied the effects of miscible WAG process on tertiary oil recovery. They concluded that WAG process had no significant effect on total oil recovery in water flooded sandstone-oil wet system. In their work the effect of areal sweep efficiency is not considered since composite model was employed in this study.

The size of the miscible slug could be determined experimentally or theoretically. Mahaffey calculated the optimum slug by setting the length of the mixing zone proportional to the square root of the distance traveled.

The purpose of this investigation is to provide some additional laboratory data that could help in determining the areal sweep efficiency of WAG process. The WAG ratios (1:1, 1:2, and 2:1) were tested in this work. The mobility of the system studied were: 0.456, 2.189, 20.65 and 45.206.

EXPERIMENTAL PROCEDURE

To achieve reproducibility of the results, it is essential that the basic properties of the model do not change from one experiment to the other. This objective was accomplished by using glass beads model. A model representing one-quarter of a five-spot was used in this investigation. A homogenous system was utilized in all runs. This was accomplished by fixing the mesh number of the glass beads (mesh no. 10). In this model of miscible displacement, molecular diffusion predominates is controlled by using the parallel plate spacing. The space between the plates was kept constant at 1.2 cm, which results in reducing convective mixing to arbitrary small levels.

The model total area was 412 square centimeters. The distance between injection point and producing point was 28 centimeters. Two types of mineral oil were utilized in this work, with viscosity 52.2 cp for oil A and 25.3 cp for oil B. The specifications of oil A and B is shown in Tables 2 and 3.

Table 1. Effect of Mobility Ratio on Areal Sweep Efficiency at Breakthrough Enclosed Five-Spot Well Pattern (Taken from Reference 5)

	Areal Sweep Efficiency—Per cent				
Mobility Ratio M	Potentiometric Analyzer		Fluid Mapper[9]	X-Ray Shadowgraph[10,11]	Analytical Calculation
	Conductive Cloth-Uskon	Electrolytic Tank[6]			
infinite	62.6[14]	62.5			
10		64.5	52.7	51.0	
4	66.4	65.8	62.0	54.0	45.0[3]
2	68.8	68.0	68.0	60.4	
1	71.6	70.0	71.7	69.8	71.5
0.25	82.2	88.5	78.0	87.0	
0.1		94.5	82.0	100.0	

Table 2. The Specifications of Oil (A)

Specific GRAVITY @ 60°F	0.885
API	28.3
Saybolt Viscosity @ 100 °F	350
Viscosity, cp @ 20°C	52.2
Pour Point, °F	−10
Flash Point, °F	430
Fire Point, °F	490
Distillation End Point, °F	952

Table 3. The Specifications of Oil (B)

Specific GRAVITY @ 60°F	0.840
API	36.95
Saybolt Viscosity @ 100 °F	70
Viscosity, cp @ 20°C	25.3
Pour Point, °F	+15
Flash Point, °F	345
Fire Point, °F	420
Distillation End Point, °F	844

In this work, displacement with colored fluids were carried out as function of viscosity ratio. Production history was obtained by tracing the specified colored area. The experiment passed through a square cross section lucite tube placed at the production point of the system. Light source was placed under the model to assist in determining the percentage of displaced (clear) and displacing (colored) areas of the model. The data obtained with injection at one corner of the well and production at the other represents a symmetry element of one quarter of a completely developed five spot pattern (Fig. 1).

The laboratory work consisted of 12 flood experiments performed at constant temperature of 20°C. The flood procedures is discussed in the following:

- The model was cleaned and packed completely with glass beads.
- The model was saturated with the specific oil (displaced fluid) and total pore space was estimated, based on the mount of fluid injected in the model. Constant gravity force was applied in the fluid injection process.
- Total pore volume of fluid injection was kept constant for all runs at 20% of the pore volume.
- For WAG process of (1:1), 5% pore volume of water was injected and the process was repeated for four cycles.

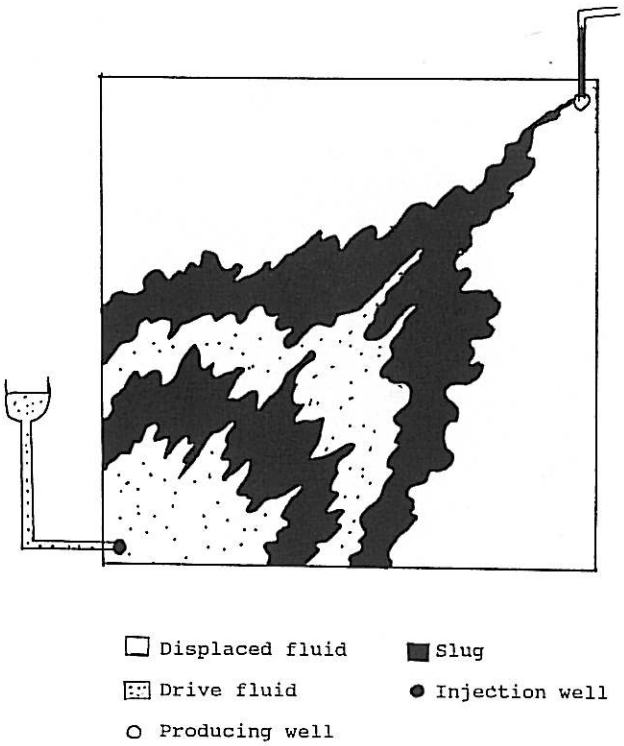


FIG. 1. Schematic diagram of the apparatus.

- WAG process of (1:2), 10% pore volume of solvent was injected and followed by 5% pore volume of water.
- WAG process of (2:1), 2.5% pore volume of solvent was injected followed by 2.5 pore volume of water.
- Upon completion of 20% pore volume of solvent injection, flow pattern of different stages were traced on transparency paper.

DISCUSSION

The results obtained in this study are, first, analyzed for the various WAG ratios at constant mobility ratio of 2.189. The total pore volume of the model is 200 cc, for WAG ratio 1:1 the total invaded (contacted area) is found to be 300 cm^2. While the total area contacted for WAG ratio of 1:2 is 322 cm^2 and 156 cm^2 for WAG ratio 2:1. The areal sweep efficiencies obtained for mobility ratio of 2.189 were 0.75, 0.85 and 0.39 for WAG ratios 1:1, 1:2, 2:1 respectively. These results indicate that WAG ratio 1:2 is the optimal value. Figs. 2, 3, and 4 show that the contacted area by the solvent is 316 cm^2 for 1:1 WAG, 322 cm^2 for 1:2 WAG and 162 cm^2 for 2:1 WAG.

The areal sweep efficiency of the various mobilities for the different WAGs are shown in Figs. 5, 6 and 7. The results of the system having a mobility of 0.456 indicate that a WAG ratio of 1:2 produces favorable sweep efficiency. Analyzing the results of performing

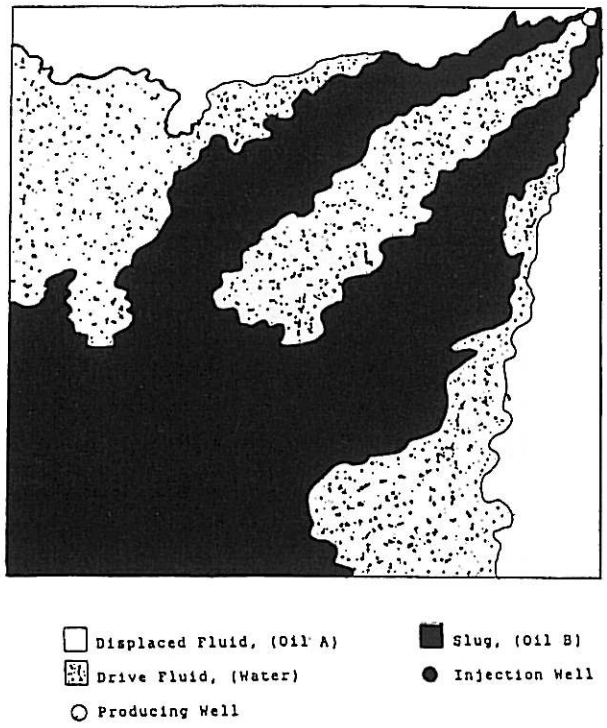


FIG. 2. Areal sweep of WAG 1:1 at mobility ratio 2.189.

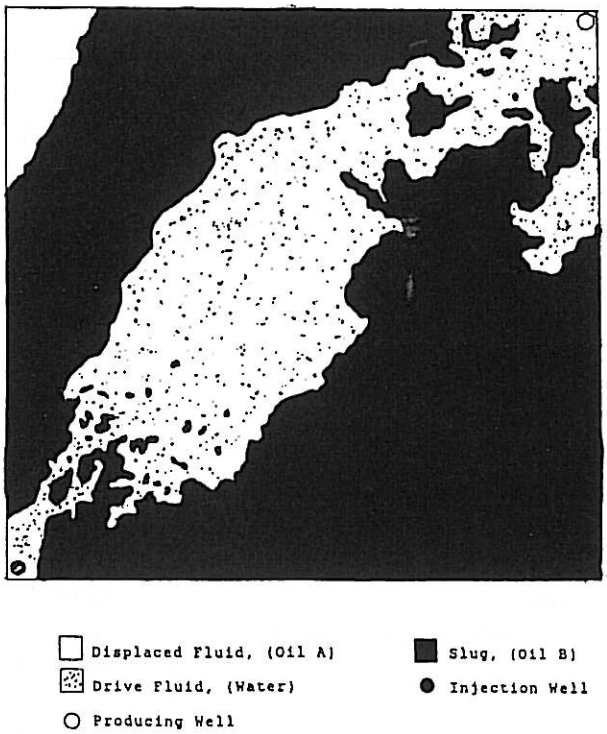


FIG. 3. Areal sweep of WAG 1:2 at mobility ratio 2.189.

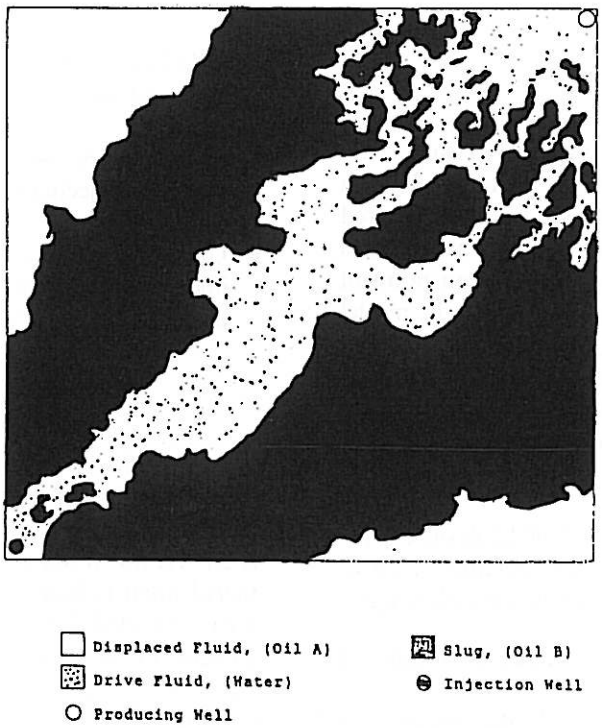


FIG. 4. Areal sweep of WAG 2:1 at mobility ratio 2.189.

the flood at a mobility of 45.206 for various WAGs 1:1, 1:2 and 2:1 yield an areal sweep of 0.5, 0.62 and 0.25 which indicate that the optimum system is WAG ratio 1:2.

Figures 8, 9 and 10 show the areal sweep of 1:1, 1:2 and 2:1. Changing the flood mobility to 20.65 and conducting the work at various WAGs 1:1, 1:2 and 2:1, yield area invaded of 248, 280 and 120 cm^2 respectively. The resulting areal sweep were 0.62, 0.70 and 0.3 for WAGs 1:1, 1:2 and 2:1 respectively. Again the optimum system is a WAG ratio of 1:2 which gives two fold increase of sweep over 2:1.

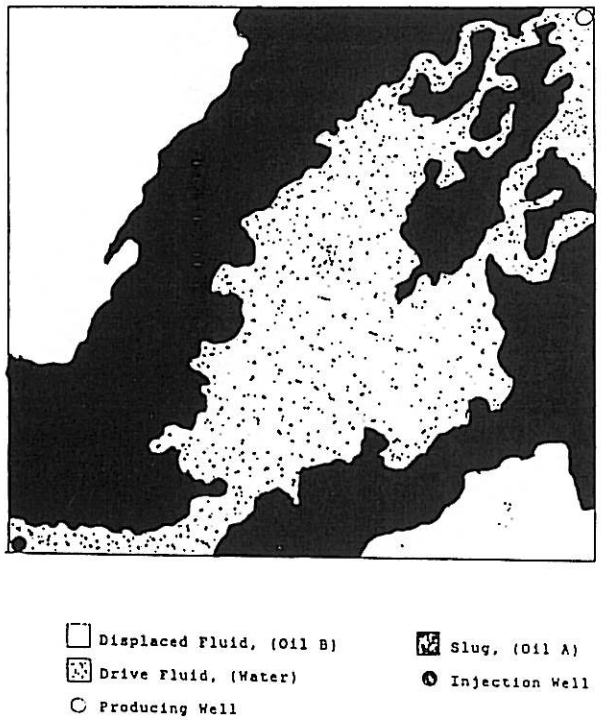


FIG. 5. Areal sweep of WAG 1:1 at mobility ratio 0.456.

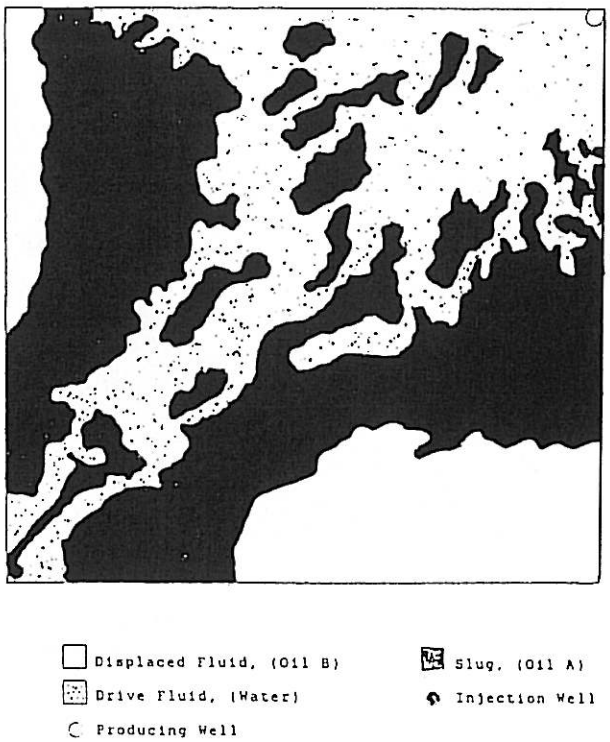


FIG. 6. Areal sweep of WAG 1:2 at mobility ratio 0.456.

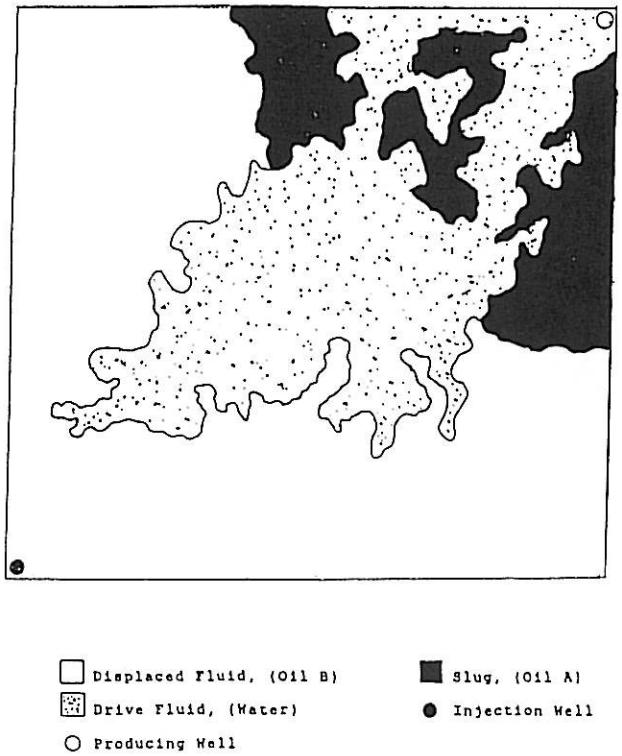


FIG. 7. Areal sweep of WAG 2:1 at mobility ratio 0.456.

Figures 11, 12 and 13 show the areal sweep of WAGs 1:1, 1:2 and 2:1. A WAG ratio of 1:1 yield areal sweep of 0.79 at mobility 0.456 and 0.5 sweep efficiency at mobility 45.206 which is around 58% increase, as presented in Tables 4, 5, 6 and 7.

Based on the results achieved in this study, the following equations are obtained:

WAG ratio of 1:1

$$\text{Areal sweep} = 0.825703 - 0.03538\log MR - 0.07765\log(MR)^2$$

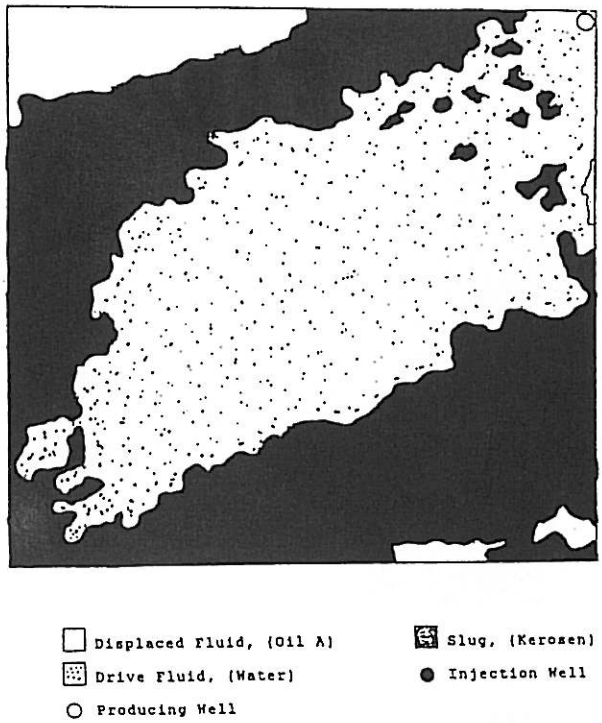


FIG. 8. Areal sweep of WAG 1:1 at mobility ratio 45.206.

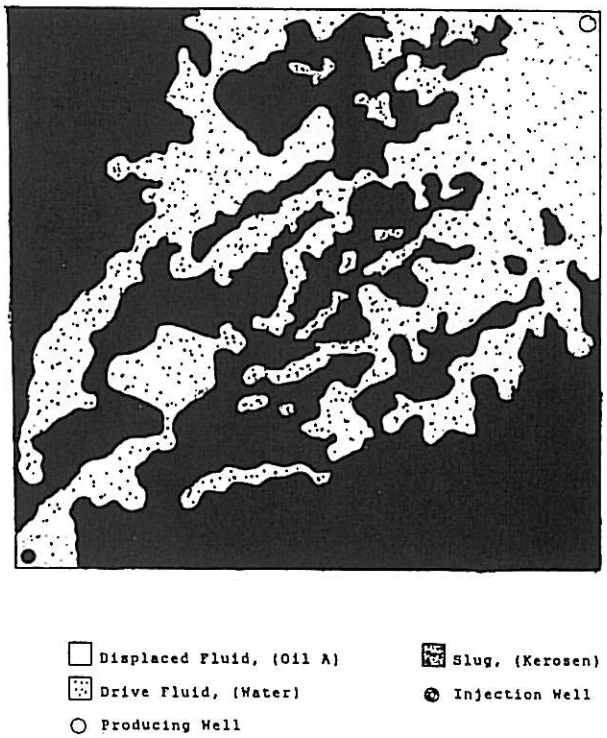


FIG. 9. Areal sweep of WAG 1:2 at mobility ratio 45.206.

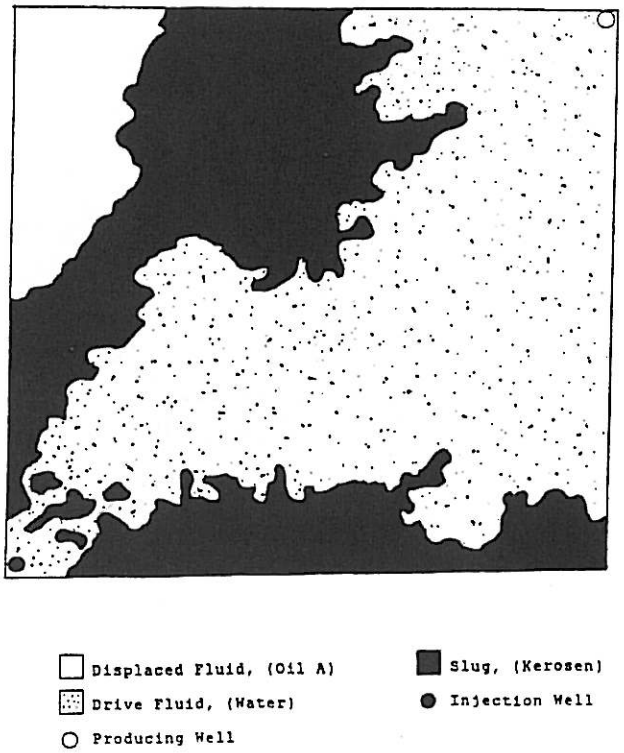


FIG. 10. Areal sweep of WAG 2:1 at mobility ratio 45.206.

WAG ratio of 1:2

$$\text{Areal sweep} = 0.825703 - 0.02636\log MR - 0.05734\log(MR)^2$$

WAG ratio of 2:1

$$\text{Areal sweep} = 0.402362 - 0.02223\log MR - 0.0422\log(MR)^2$$

The above equations could be utilized in reservoir simulation to estimate the areal sweep of the studied system.

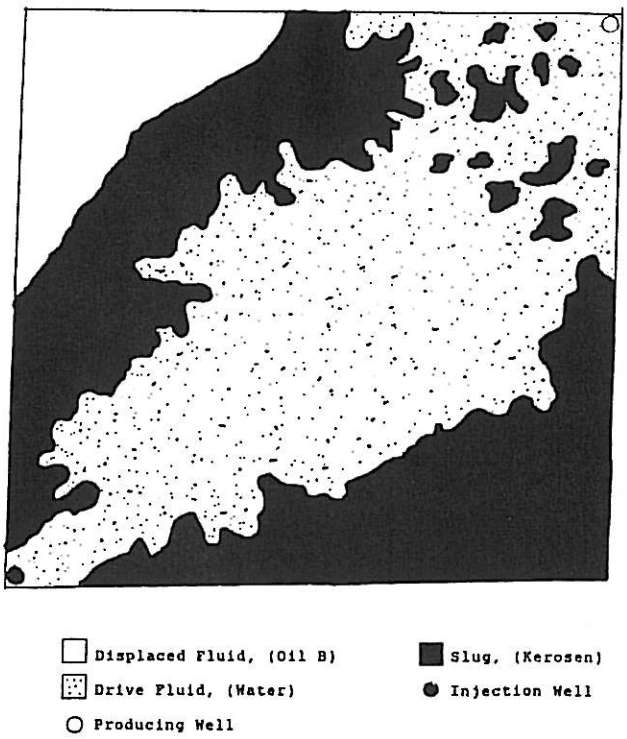


FIG. 11. Areal sweep of WAG 1:1 at mobility ratio 20.65.

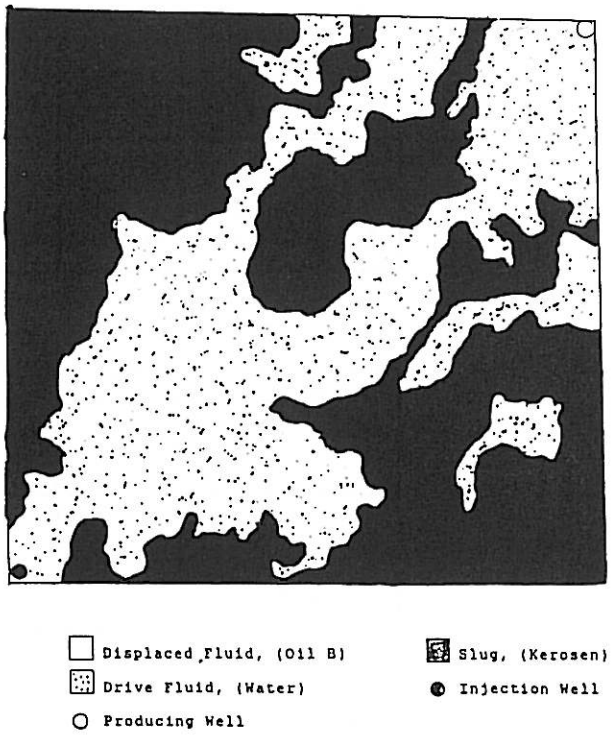


FIG. 12. Areal sweep of WAG 1:2 at mobility ratio 20.65.

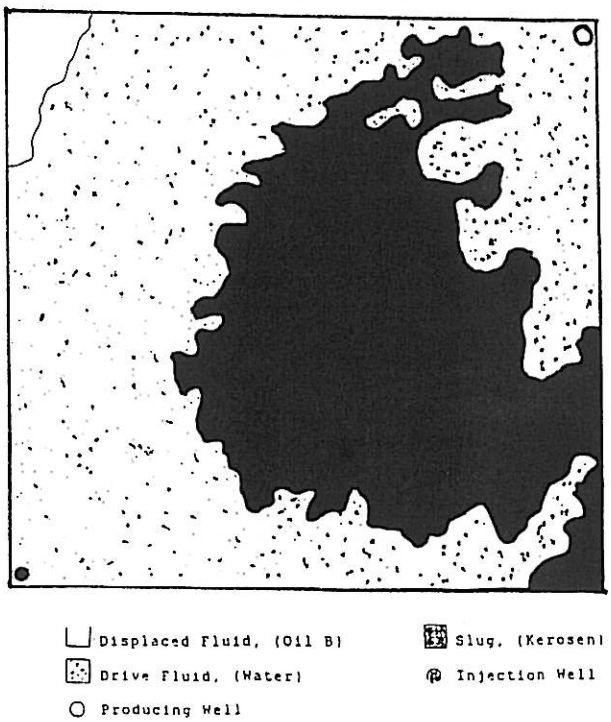


FIG. 13. Areal sweep of WAG 2:1 at mobility ratio 20.65.

Table 4. Areal Sweep of Different WAGs at Mobility Ratio 2.189

WAG	Displaced Fluid	Sulg	Drive Fluid	Total P.V. cc	Invaded Area cm^2	Area Sweep Efficiency
1:1	Oil (A)	Oil (B)	Water	200	300	0.750
1:2	Oil (A)	Oil (B)	Water	205	322	0.805
2:1	Oil (A)	Oil (B)	Water	200	156	0.390

Table 5. Areal Sweep of Different WAGs at Mobility Ratio 0.456

WAG	Displaced Fluid	Sulg	Drive Fluid	Total P.V. cc	Invaded Area cm^2	Area Sweep Efficiency
1:1	Oil (B)	Oil (A)	Water	205	316	0.790
1:2	Oil (B)	Oil (A)	Water	210	322	0.830
2:1	Oil (B)	Oil (A)	Water	205	162	0.405

Table 6. Areal Sweep of Different WAGs at Mobility Ratio 20.65

WAG	Displaced Fluid	Sulg	Drive Fluid	Total P.V. cc	Invaded Area cm^2	Area Sweep Efficiency
1:1	Oil (B)	Kerosen	Water	210	248	0.65
1:2	Oil (B)	Kerosen	Water	220	280	0.70
2:1	Oil (B)	Kerosen	Water	220	120	0.30

Table 7. Areal Sweep of Different WAGs at Mobility Ratio 45.206

WAG	Displaced Fluid	Sulg	Drive Fluid	Total P.V. cc	Invaded Area cm^2	Area Sweep Efficiency
1:1	Oil (A)	Kerosen	Water	200	200	0.50
1:2	Oil (A)	Kerosen	Water	215	248	0.62
2:1	Oil (A)	Kerosen	Water	200	100	0.25

CONCLUSIONS

- The model studied gives an insight into the effects of WAG process on the areal sweep efficiency. The most efficient WAG ratio for the studied system is found to be WAG of 1:2.
- Equations were developed to predict the areal sweep as function of mobility for WAGs of 1:1, 1:2 and 2:1. The results of this work could be utilized in analytical and numerical models to estimate the areal sweep efficiency of WAG process of 1:1, 1:2 and 2:1.

ACKNOWLEDGEMENTS

The authors gratefully acknowledge the efforts of Mohamed EL-Mmajdob, Nasser Alteer and Emad Abshina in conducting the laboratory experiments.

REFERENCES

[1] Armofsky D.W., and Ramey, H.J., 1956, Trans. AIME 207, 205.
[2] Cheak, R.E., and Menzie, D.E., 1951, Tran. AIME 204, p205 (1955).
[3] Fay, C.H., and Parts, M., proc. Word Pctr. Congress, Sec II.
[4] Sheldon, J.W., and Doughherty, E.L., Oct. 8–11, 1961., Paper no. SPE 183, AIME Dallas mtg.
[5] Bradley, H.B., Heller, J.P., and Odeh, A.S., Oct. 2–5, 1960, paper no. 1585-G, AIME Denever mtg.
[6] Hebermann, B., 1960, 'Efficiency of miscible displacement as a function of mobility ratio', Trans., AIME 219, p. 264.
[7] Mahaffey, A.L., and Rulherford, W.M., and Matthews, C.W., March 1966, 'Sweep efficiency by miscible displacement in five-spot' Soc. Pet. Eng. J. 73–80, Trans., AIME 237.
[8] Lacy, J.W., Faris, J.E., and Brinkmann, F.H., Aug. 1961, 'Effect of bank six on oil recovery of the high pressure gas drive LPG-Bank process' JPT 806–12.
[9] Zekri, A.Y., Nnatuh, A., May 18–20, 1992, 'Laboratory study of the affects of miscible WAG process on tertiary oil recovery', (ADSPE 201) presented at 1992 Abu Dhabi 5th Petroleum Conference and Exhibition.
[10] Blackwell, R.J., Rayne, J.R., and Terry, W.M., 1959, 'Factors Influencing the efficiency of miscible displacement' Trans. AIME, 216.

PRJ, Vol. 6 (January 1994); P. 18–31, 29 FIGS, 3 TABLES.

FAILURE INVESTIGATION OF WELD JOINT BETWEEN MANURITE 36X AND INCOLOY 800H TUBES IN ETHYLENE PLANT CRACKING FURNACE

M.L. Mahta* and A.T. Hassan**

دراسة حالة الإخفاق بماسورة الوصل الملحومة بين أنابيب المارونايت 36X وأنكولوي 800H بفرن التكسير بمصنع الاثيلين

م. مهتا و عبد الفتاح حسن

تم القيام بأعمال الدراسة المجهرية وقياس التأثر بالمغناطيسية وتعيين كمية الكربون في مناطق مختلفة من منطقة اللحام، كما تم قياس الصلابة، وتعيين التركيب الكيميائي والتحليل بجهاز EDAX.

لقد تم تشقق اللحام في كامل سمك المادة مع وجود مواقع تكربن وتكون كربيدات في حدود الحبيبات وتولد طور رمادي. كما لوحظ وجود صلادة (عالية) بمواقع التكربن وتجاويف زحف/شقوق. التحليل بجهاز EDAX وضح أن الطور الرمادي المتكون عند حدود الحبيبات غنيا بمعدني المنجنيز والكروم.

بدا تشقق اللحام من الجذر نتيجة تكربن جذر اللحام وتولد الطور الرمادي سهل التقصف بحدود الحبيبات. وزاد تغلغل الشقوق بمساعدة الزحف المتزايد الناجم عن تركز الإجهادات بأطراف الشق والإجهاد العالي الذي تولد عن صغر مساحة اللحام التي تعرضت للضغط مع تطور الشق وتكون الطور الرمادي سهل التقصف بحدود الحبيبات.

ABSTRACT

Macroscopic study, magnetic susceptibility measurement, bulk carbon analysis of different regions of the weld, hardness masurement, chemical composition and Energy Dispersive of X-Ray Analysis (EDAX) were carried out. Localized carburization in the weld regions, formation of grain boundary carbides and grey phase, hardness at carburized locations and creep cavities/cracks were observed. EDAX revealed brittle grey phase formed at grain boundaries rich in Mn and Cr.

Initiation of weld cracking was from its root. This was caused by carburization of the root of the weld and the formation of brittle grey phase at grain boundaries through their embrittling effects. Propagation of cracks was assisted by enhanced creep due to stress concentration centration at crack tips and higher stresses caused by decreasing load bearing area of the weld with the progress of the fracture and formation of brittle grey phase at grain boundaries.

* Formerly with Petroleum Research Centre, Tripoli, Libya, G.S.P.L.A.J.

** Petroleum Research Centre, P.O. Box 6431, Tripoli, Libya, G.S.P.L.A.J.

INTRODUCTION

Ethylene is produced by cracking naphtha in the radiant coil tubes heated in the furnace. Cracking is accomplished at low pressures and elevated temperatures in the range 950–1100°C.

The environment within the radiant coil tubing is carburizing while that on the outside or fire box side is oxidizing.

The outlet of the tube is exposed to higher temperature coil tubes and decoked at regular intervals.

CASE HISTORY

Cracking occured in the outlet of the radiant tube of the coil and is marked in the Fig. 1. Crack was observed at weld joint between dissimilar tubes,

Manurite 36X and Incoloy 800H during operation of the furnace. The following is the pertinent data of the case:

Outlet pipe material: Manurite 36X-Incoloy 800H pipe.
Skin temperature during services: 1003–1035°C
Design temperature: 1080°C
Maximum operating pressure: 1.83 kg/cm^2
Design pressure: 5.4 kg/cm^2
Decoking carried out: 9 times during the furnace working time of 548 days.

higher susceptibility was observed from the root side.

Incoloy 800H was also found to be susceptible from the internal surface, while Manurite 36X was not susceptible in any region. Reason for localized development of magnetic susceptibility is localized carburization of the weld during service. Chromium is withdrawn from the matrix. This chromium depletion yields a matrix which becomes progressively more magnetic.

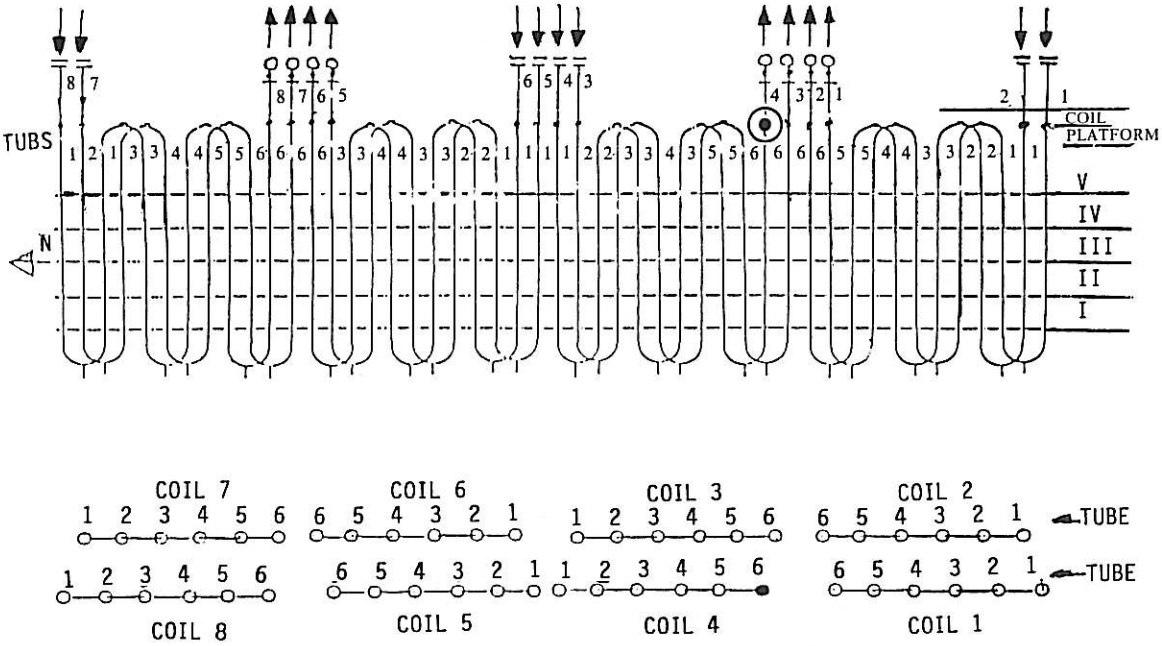


FIG. 1. Sketch of the radiant coil of cracking furnace 1-F-10-G with the location of crack (encircled).

INVESTIGATION

A. Magnetic Susceptibility

Metallographic observations revealed extensive formation of second phase precipitates in the area along the fracture surface of the weld. The magnetic susceptibility of the weld joint was to bring one of the poles close to the weld joint to detect susceptible and non-susceptible regions of the weld. For this measurement small samples containing the weld had to be cut for detecting magnetic susceptibility. Observations are marked in Fig. 2.

Regions of the weld cracked through thickness showed magnetic susceptibility while uncracked as well as partially crack regions were not found to be susceptible. For the susceptible region, weld away from the fracture was not susceptible indicating localized carburization. Further a

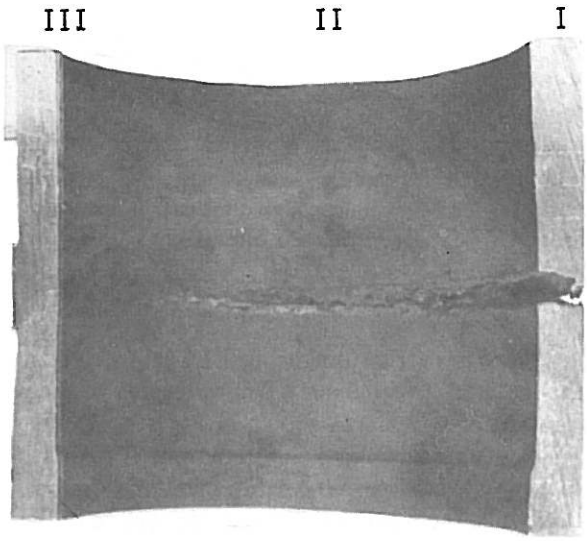


FIG. 2. Magnetically susceptible (MS) region of the weld (cracking through thickness) and nonsusceptible (NS) weld region marked on one of the equal halves of the tube.

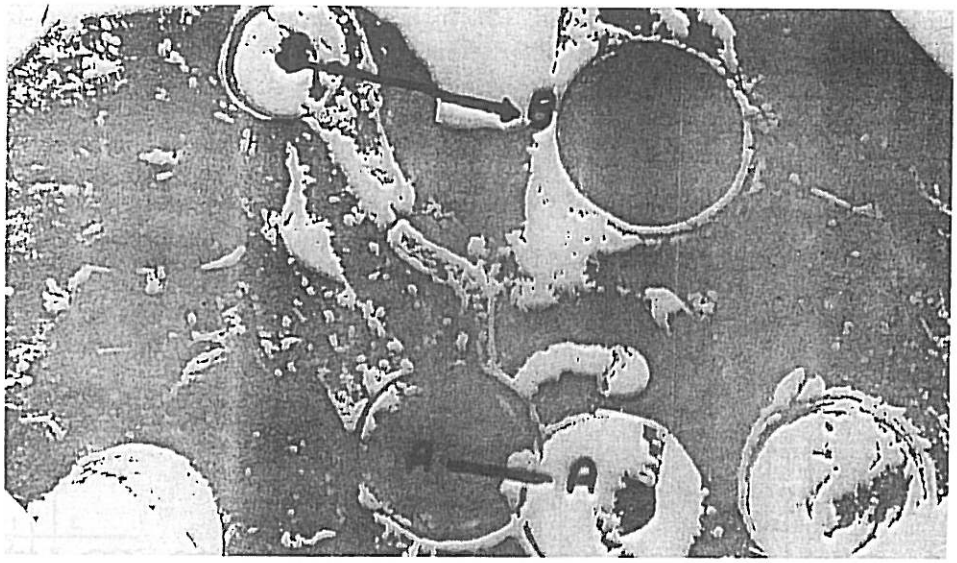


FIG. 3a. Three locations analysed for carbon analysis from the weld region partially cracked through thickness (i) A-A in the root region (ii) B-B around weld center line (WCL) near weld surface (OWS) (iii) C-C OWS but away from WCL.

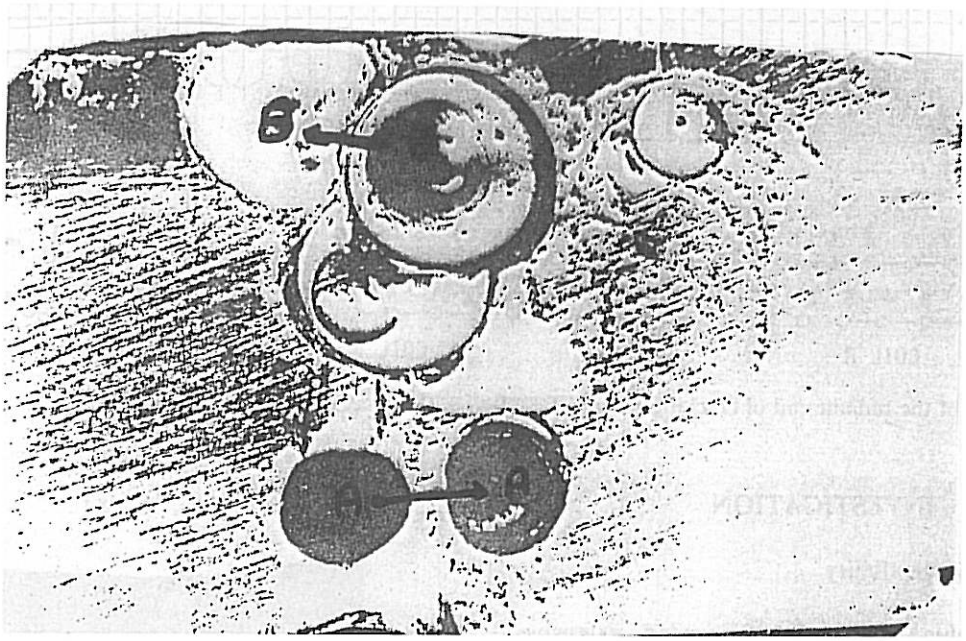


FIG. 3b. Two locations analysed for carbon analysis from the weld region free from cracks (i) A-A in the root region (ii) B-B around WCL near outer weld surface.

B. Carbon Analysis

This was carried out using LECO instrument on the material drilled from different regions of the weld (samples II and III) as shown in Figs. 3a, 3b.

Results are listed in Table 1. Sample II clearly indicates carburization in the root region and weld center line, while the weld near the outside surface but away from the center line, did not suffer from carburization.

Carbon contents in the carburized regions were 0.62 and 0.54 wt.% respectively, while it was 0.12 wt.% for the uncarburized regions. Sample II was magnetically susceptible from the fracture end as well as from the root side.

For sample III, free from cracking, carbon content in the outer weld region and that in the root region are different as seen in Table 1. However, the difference is not large enough to indicate carburization. This sample did not show magnetic susceptibility.

The inner surface Incoloy 800H tube suffered from carburization while the outer surface was not affected as evident from the results listed in Table 1.

Table 1. Bulk Carbon Analysis of Different Regions of the Weld

Location of samples	Weight of the sample (g)	Carbon content (wt.%)
1. As seen in Fig. 3a		
a. Root region of the weld designated as A-A	0.1957	0.620
b. Near outer weld surface in and around weld center line (WCL) region B-B	0.1454	0.540
c. Outer weld surface but away from the fracture surface region C-C	0.1612	0.120
2. As seen in Fig. 3b		
a. In the root pass region AA-	0.1636	0.155
b. Near outer weld surface region B-B	0.1559	0.102
3.		
a. Inner surface of Incoloy 800H tube	0.1426	0.441
b. Outer surface of Incoloy 800H tube	0.2839	0.129

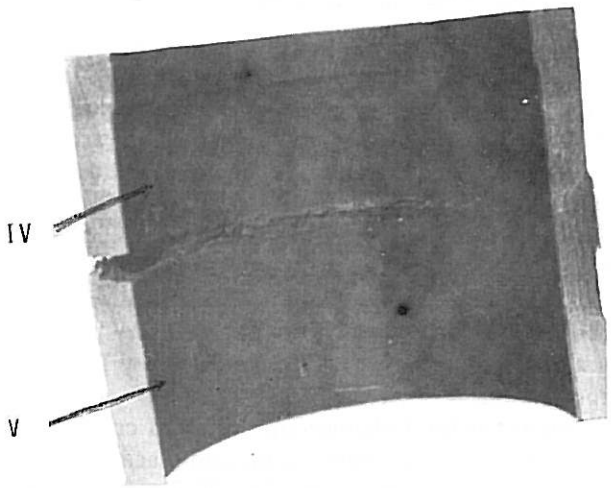


FIG. 4. Cross sections of the weld regions, from locations IV. V as indicated in the micrograph.

C. Hardness

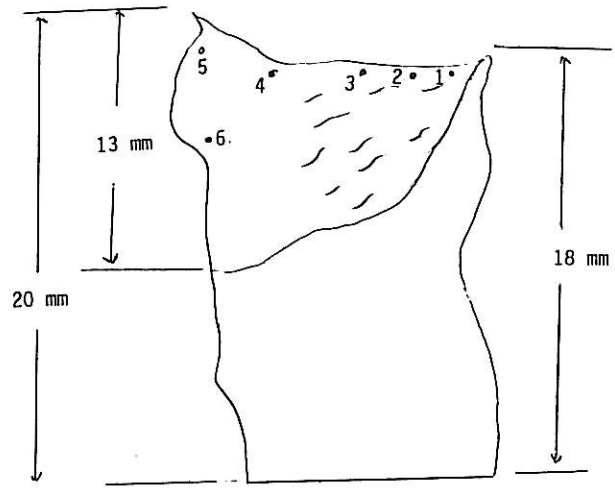
Hardness was measured in the cross-sections of the weld regions from locations IV, V indicated in Fig. 4 using Vickers Hardness Tester.

Locations, where hardness was measured, are shown schematically in Figs. 5a, 5b and 5c. Large hardness increase was detected along the fracture edge through the thickness of fracture region of the weld (Fig. 5a), near the outer weld surface. Away from the fracture edge the hardness was much lower, 158 HV5 as compared to 260 HV5 in the root, while in the region with multiple minute visible cracks in the root area (Fig. 5b) hardness recorded was higher than in the weld region free from cracks as evident from the results listed in Fig. 5b. In the weld region, which in the cross-section (Fig. 5c) showed a minute visible crack in the root region, hardness variation was not observed.

D. Metallographic Study

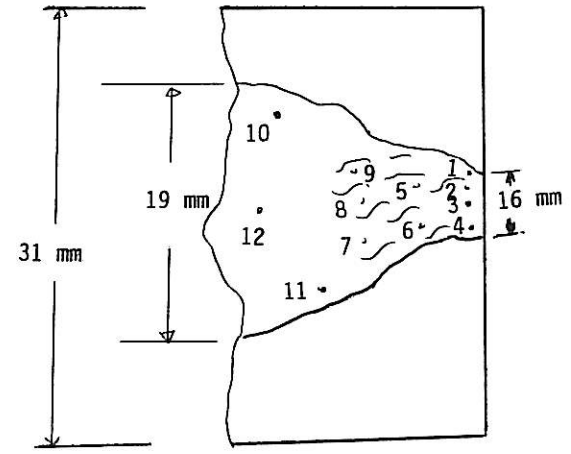
Samples I–III were taken from weld region and their location is depicted in Fig. 4. They were taken from weld region which had visible minute cracks/ crack in the root of the weld.

Sample I. Figure 6a is the microstructure of cross section fracture along the weld center line. Microstructures in the root region and those adjacent and away from the fracture in the weld are shown in Figs. 6b, 6c, 6d and 6e. Extensive precipitation in the root region and fracture region Fig. 6(b–d) were seen within grains. Precipitates, within the matrix, are attributed to the carbides resulting from carburization. Away from the fractured surface, precipitation is less extensive and is finer. Fig. 6e shows the formation of creep microcavities/voids along grain boundaries and the much finer precipitates. This region has not undergone carburization but suffered extensive creep damage. Grey phase at grain boundaries was detected in the root of the weld as well as in the filler passes as in Figs. 6b and 6f. This phase is porous and brittle.



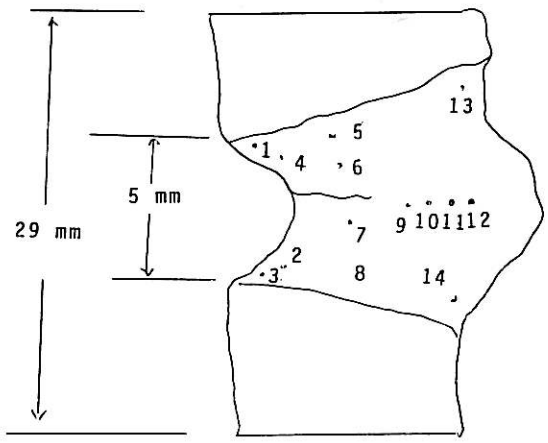
Location of hardness measurement	Hardness HV5
1	260
2	262
3	268
4	246
5	166
6	158

FIG. 5a. Schematic representation of locations of hardness measurements and hardness values in weld region shown in Fig. 6a revealing high hardness in the fracture end.



Location of hardness measurement	Hardness HV5
01	229
02	186
03	172
04	161
05	178
06	172
07	157
08	172
09	162
10	161
11	157
12	157

FIG. 5b. Schematic representation of locations of hardness measurement and hardness values in weld region shown in Fig. 8a revealing higher hardness in the root of the weld.



Location of hardness measurement	Hardness value HV5
01	153
02	158
03	157
04	153
05	153
06	152
07	156
08	157
09	160
10	156
11	156
12	162
13	153
14	157

FIG. 5c. Schematic representation of location of hardness and hardness values in weld region shown in Fig. 9a.

Sample II. Figure 7a give the macrostructure of section of the weld region showing cracking in the root region of the weld and cracks, away from the weld center line. Figures 7c and 7d show cracks in the root and extensive precipitates of different shapes.

Grain boundaries precipitates and some of precipitates in the matrix are attributed to carbides. These microstructural changes indicate carburization of the root region of the weld. Formation of grey phase at grain boundaries was also observed away from the root region.

Microstructural changes are less, and creep damage in the form of cavities/voids and cracks are seen as illustrated in Fig. 7e and Fig. 7f. Precipitates are much finer and such microstructural changes are observed in the later part of the third stage creep.

Sample III. Macrostructure of the cross-section in Fig. 8a shows only a small crack in the root region. The microstructure of this area (Fig. 8b and Fig. 8c) consists of fine precipitates and cracking along grain boundaries. Grains are twinned. Formation of grey phase at grain boundary is detected Fig. 8d. In addition, creep cavities/voids at grain boundaries have taken place Fig. 8b. No hardening was observed; hardness being the same for cracked and uncracked regions of the weld Fig. 5c. Neither bulk carbon analysis nor magnetic susceptibility measurement indicated carburization. Ahead of the root crack, formation

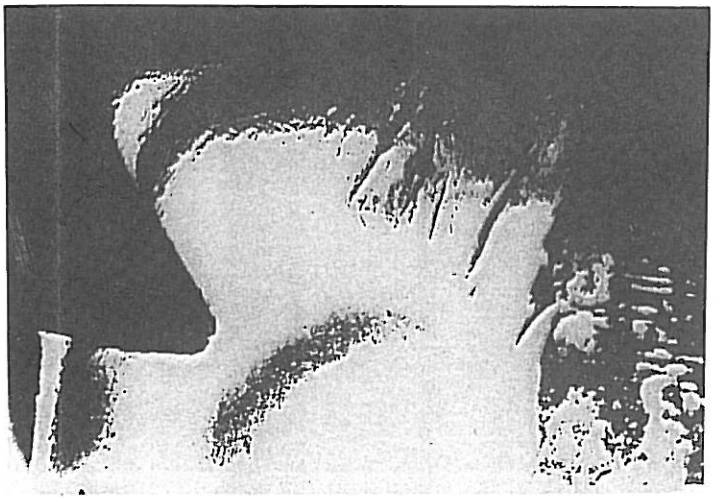


FIG. 6a. Sample I Microstructure of the cross section through thickness fracture region of the weld showing multiple internal cracks (etched).

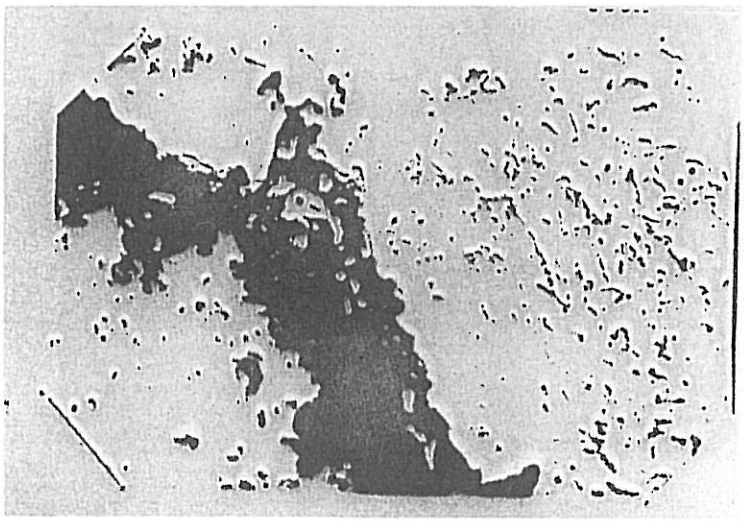


FIG. 6b. Root cracks associated with grey phase.

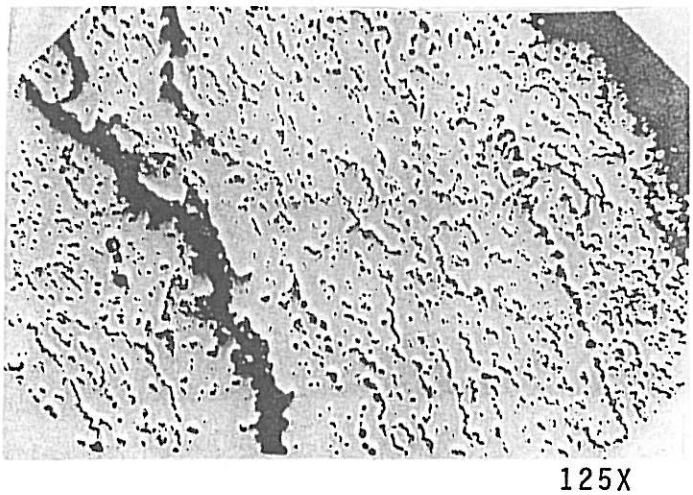
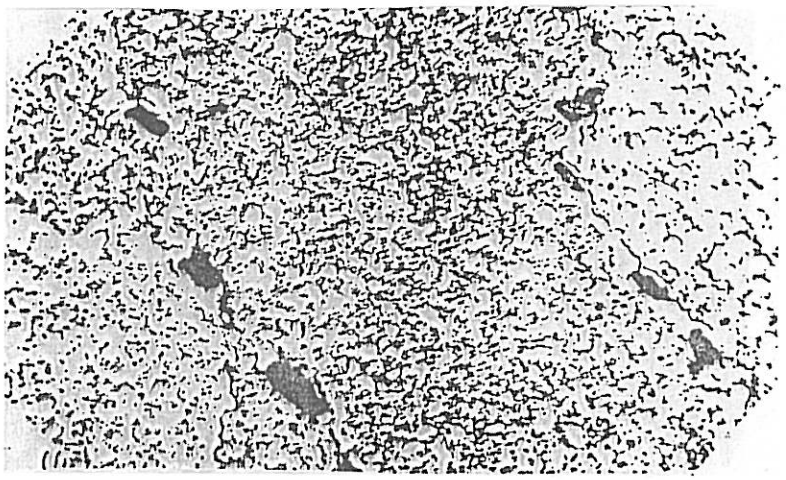
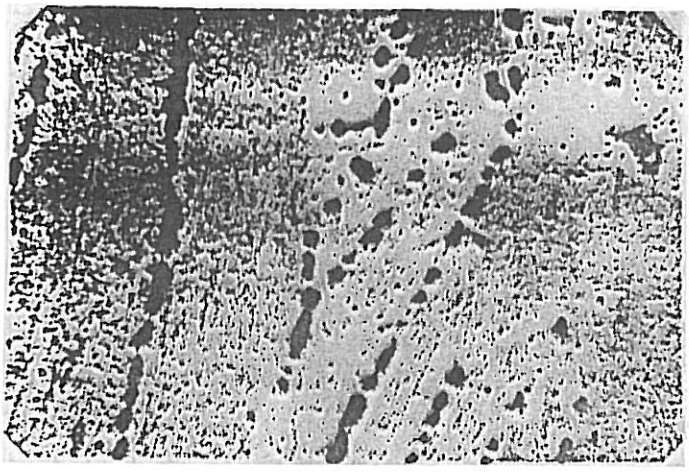


FIG. 6c. Root cracks and extensive precipitation along grain boundaries resulting from carburization of the root.



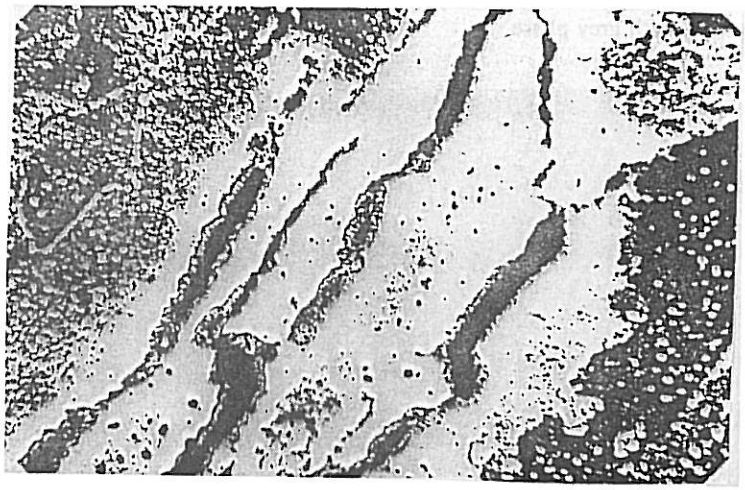
250 X

FIG. 6d. Continuous grain boundary precipitates (carbides) and different shaped precipitate, within grains.



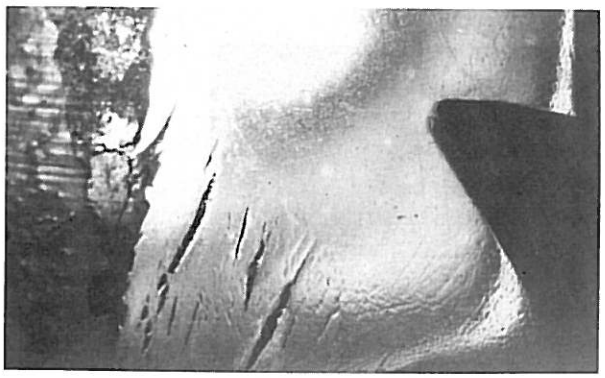
125 X

FIG. 6e. Away from fracture end, region showing fine precipitates and extensive, creep voids/cavities.



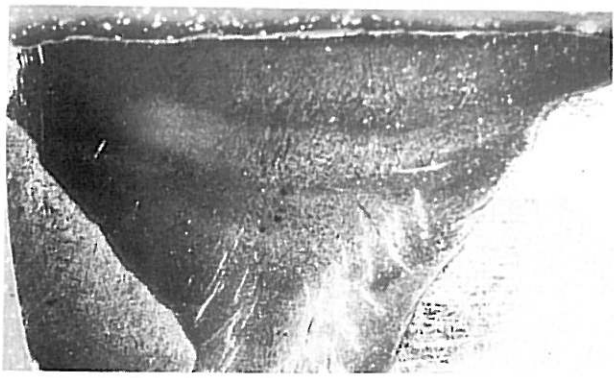
125 X

FIG. 6f. Grey phase fomation at grain boundaries and extraction through the grey phase.



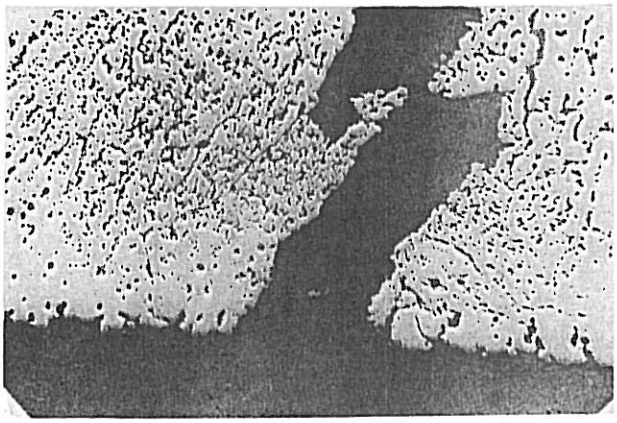
7 X

FIG. 7a. Sample V Macrostructure of the cross section showing multiple cracks in the root and away from WCL but no cracks formed in the outer weld surface (unetched).



7 X

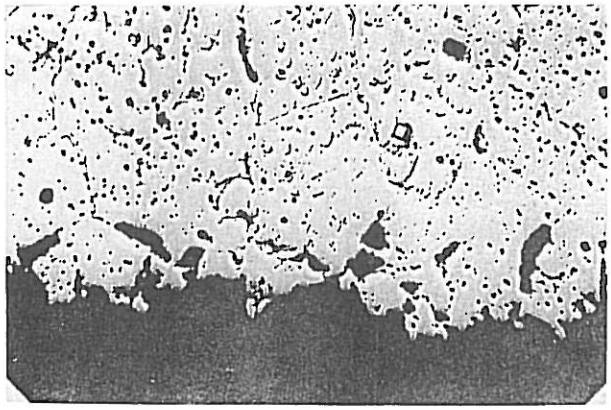
FIG. 7b. Same as Fig. 8(a) but after etching showing columnar grain structure of the weld metal.



125X

FIG. 7c. Cracking started from the root extensive precipitation within grains and at grain boundaries resulting from carburization (unetched).

of grey phase precipitates at grain boundaries was observed Fig. 8e. In the present case grey phase is essentially responsible for initiation of root crack and its partial propagation, Figs. 8d and Fig. 8e.



500X

FIG. 7d. Showing different shaped precipitates within grains and association of cavities with grain boundaries precipitates (unetched).

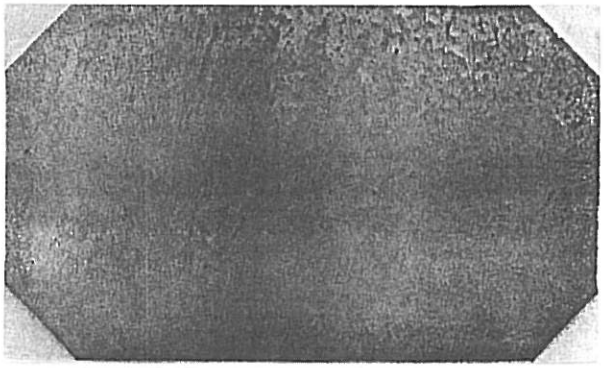
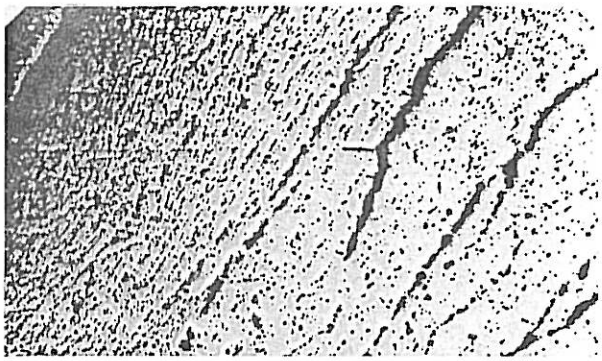


FIG. 7e. Middle of the weld showing finer precipitates and isolated creep cavities (unetched).



65X

FIG. 7f. Creep cracks and cavities adjacent to fusion line in the weld region away from the root region (etched).

E. EDAX

EDAX of grey phase at grain boundary (Fig. 9a) was observed to contain mainly Cr and Mn with some Ti as seen in Fig. 8b. EDAX shows absence of sulphur in the grey phase.

Figure 9c shows EDAX of grey phase at grain boundary revealing the grey phase to consist of only Mn and absence of Cr and Ti. Figure 9d shows

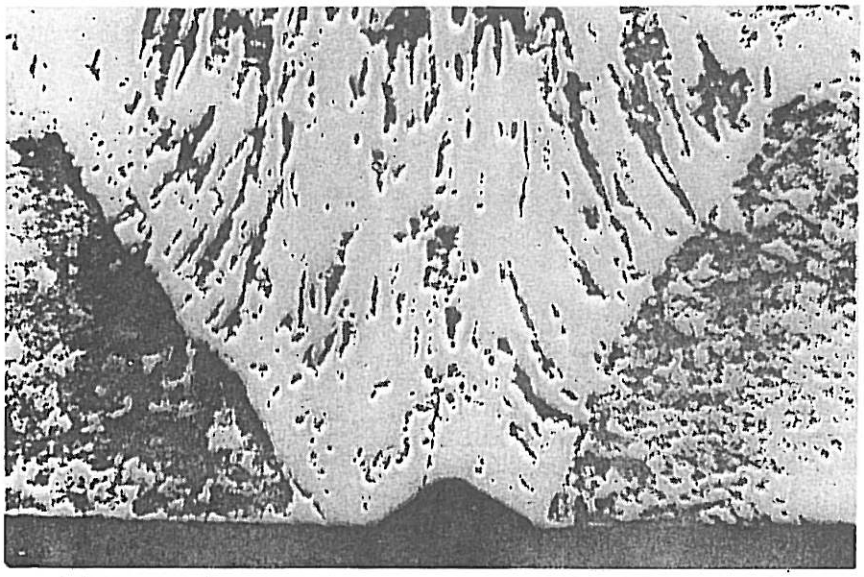


FIG. 8a. Macrostructure of the cross section of the weld region showing a root crack and columnar grain structure materials drilled from root bottom, (etched).

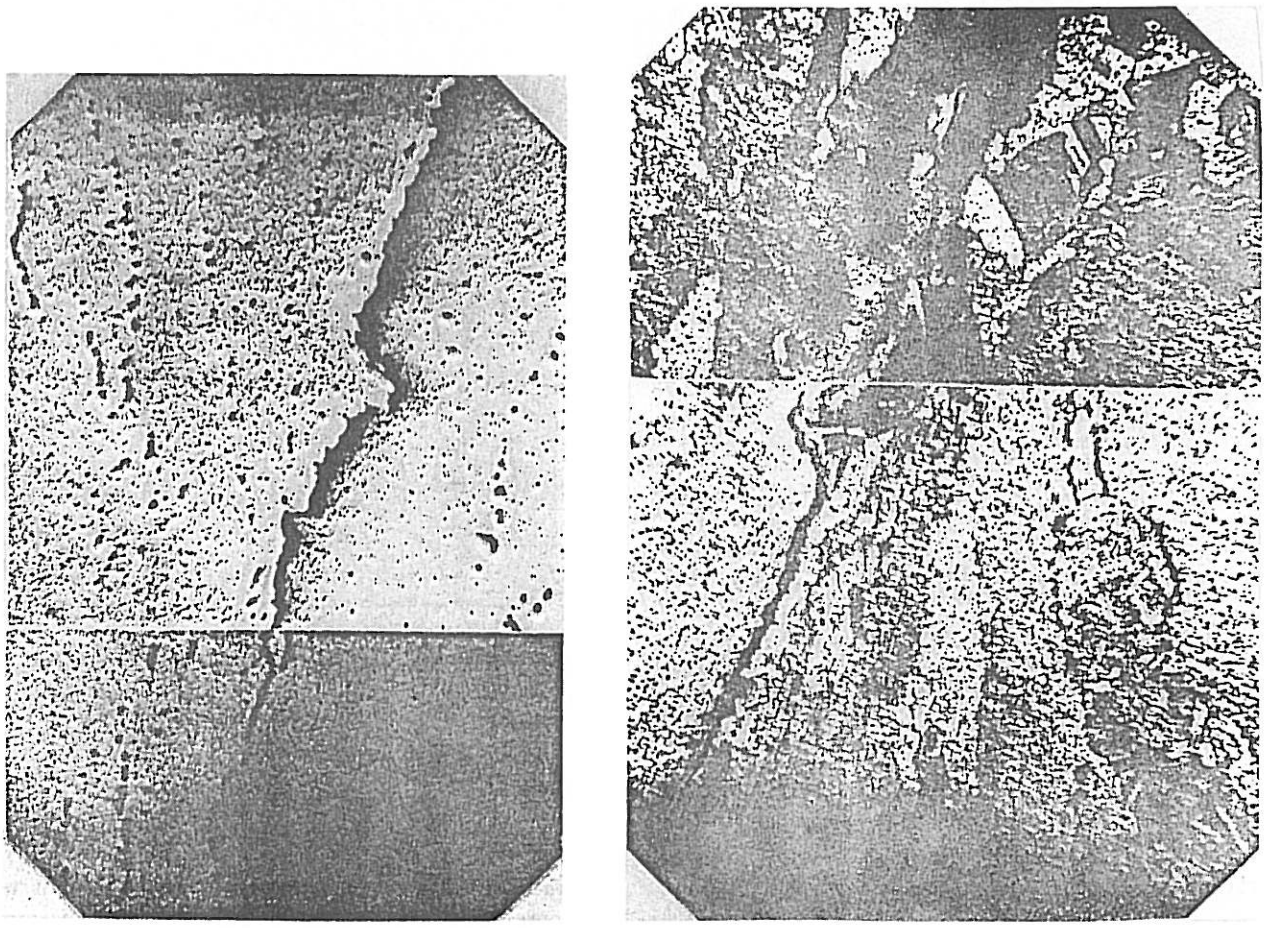


FIG. 8b,c. Root crack formation and its propagation in the root region not affected by carburization but affected by creep damage as seen around the crack and ahead of the crack.

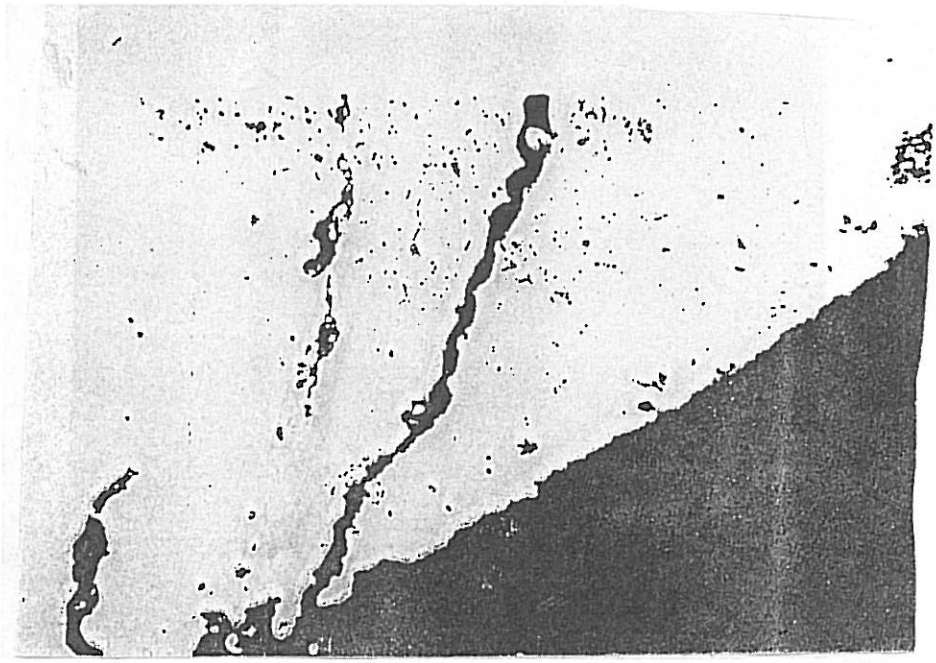


FIG. 8d. Grey phase formed at grain boundaries assisted nucleation of root crack.

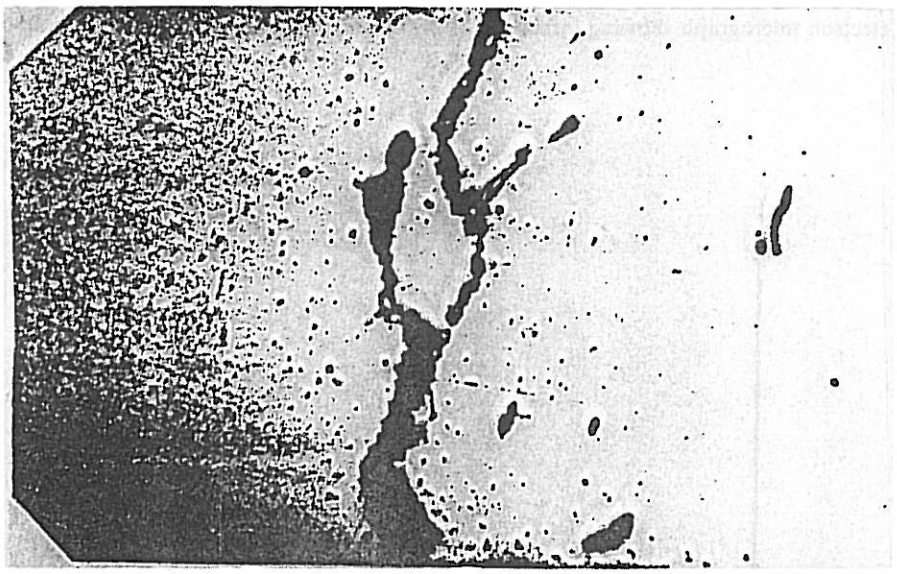


FIG. 8e. Grey phase facilitating crack propagation.

scanning electron micrograph, EDAX and quantitative chemical analysis of grey phase.

EDAX of rod shape precipitates in the matrix is shown in Fig. 9e, which reveals that this precipitates consist of Ni, Cr, Fe and Mn, major component being Ni and Cr.

CHEMICAL COMPOSITION

In view of the failure of the weld, chemical composition determined was only for the weld using atomic absorption spectrometer. Results are given in Table 2a. Composition for welding electrode used is listed in Table 2b. Analysis of Mo, Ti and Nb was not carried out for the weld.

Iron present in Weld Metal (WM) is higher while Ni is lower as compared with that in welding electrode. This difference results from dilution of welding driller metal caused by the admixture of the base metal. Base metals in the present case are dissimilar materials, Manurite 36X and Incoloy 800H being iron based alloys. Their composition are listed in Table 2b for reference.

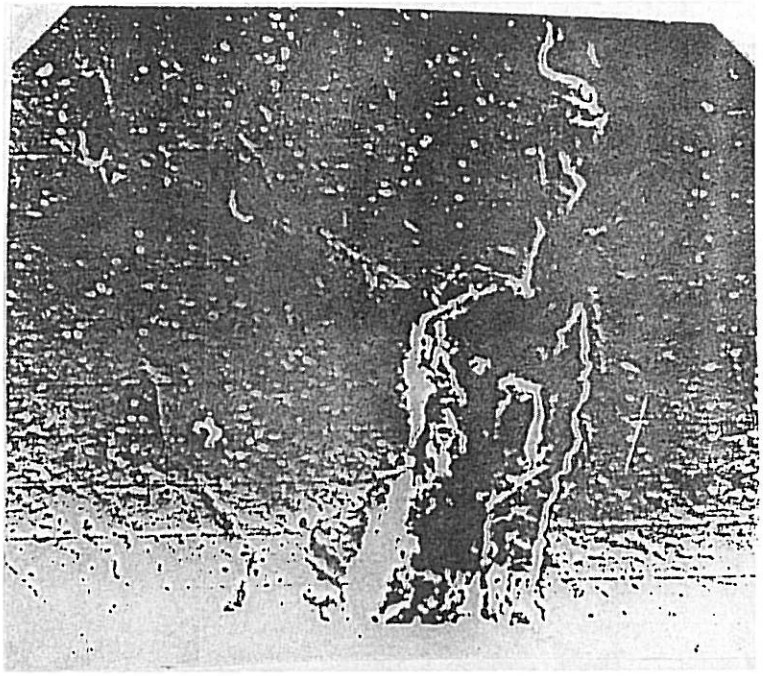


FIG. 9a. Scanning electron micrograph showing formation of brittle and porous grey phase at grain boundaries and matrix precipitates.

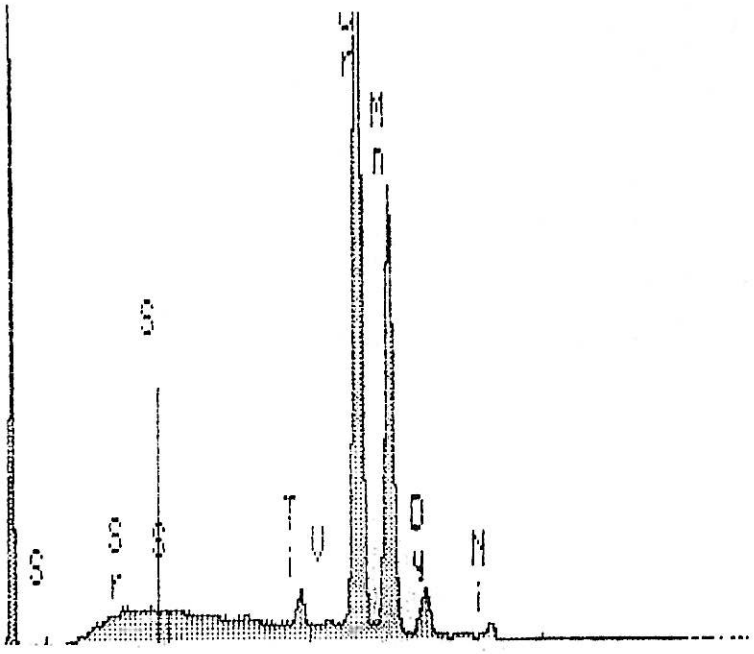


FIG. 9b. EDAX of grey phase precipitates showing presence of Cr, Mn and some Ti.

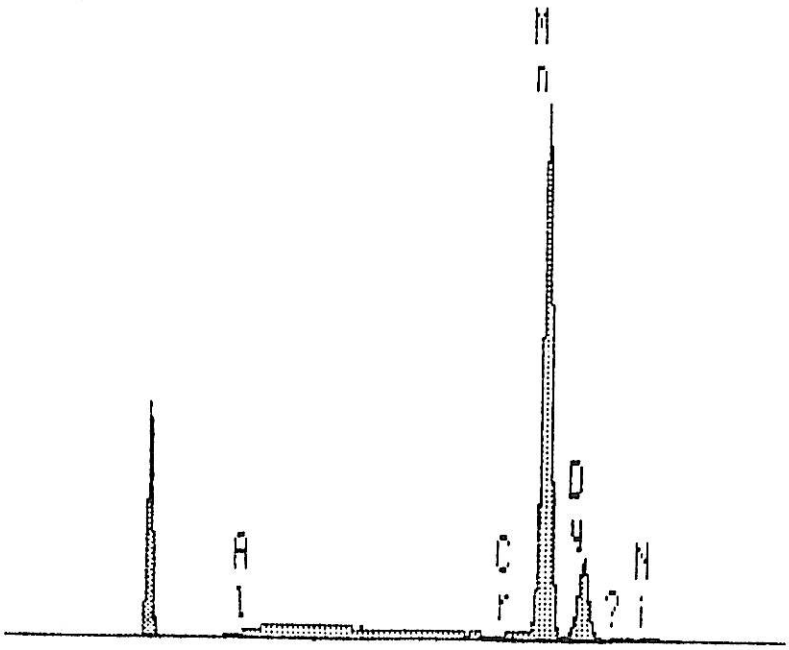
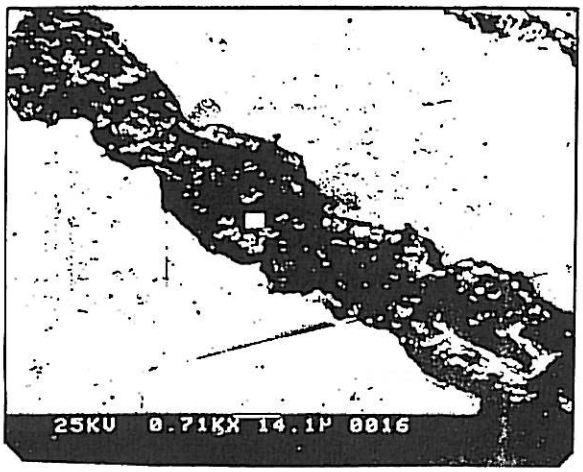


FIG. 9c. EDAX of grey phase facilitating crack propagation.



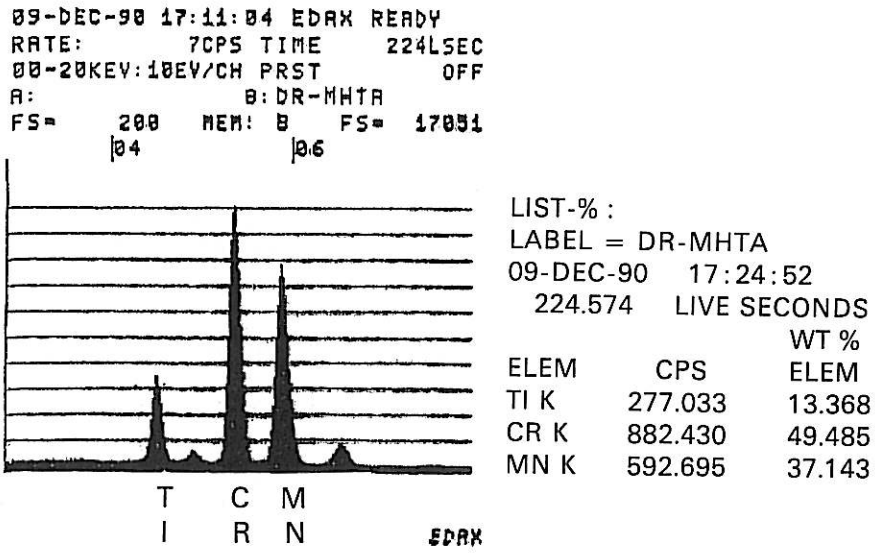


FIG. 9d. EDAX of the area marked in scanning electron micrograph and quantitative elemental composition of the grey phase.

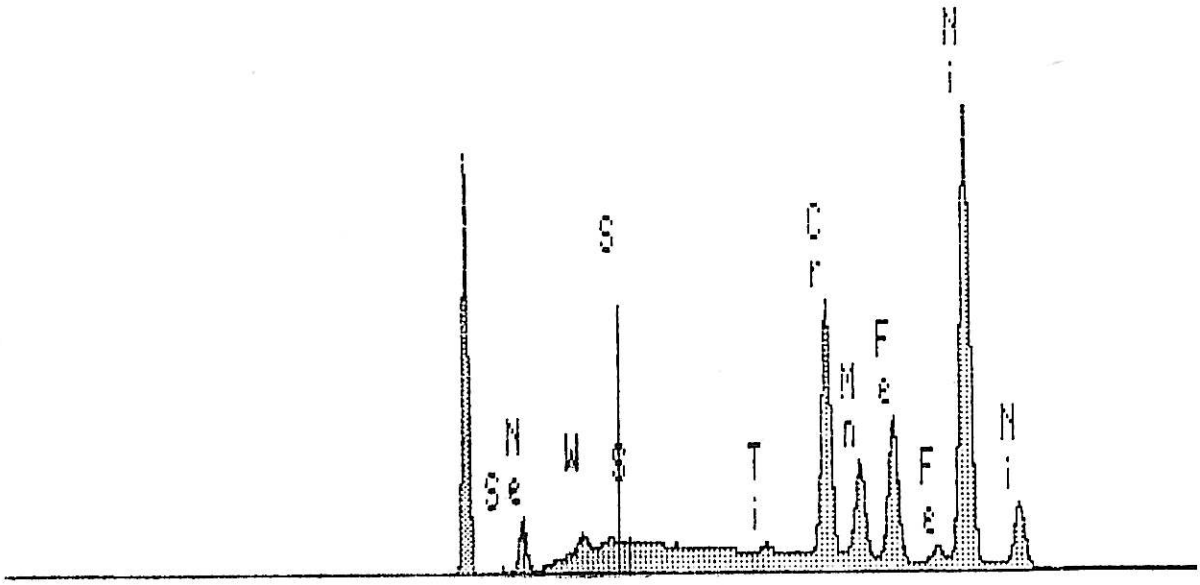


FIG. 9e. EDAX of the shape precipitates within the grain showing presence of Ni, Cr, Fe and Mn.

Table 2a. Chemical Composition of Welding Electrode ER. Ni-Cr-Fe_3

Element	C	Ni	Mn	Cr	Mo	Ti	Fe
%	0.05	67	5	19	1	2	3

Chemical Composition of Weld Metal

Element	Ni	Al	Cr	Fe	Mn
%	60	0.08	18.9	11.3	6.7

Table 2b. Manurite 36X

Element	C	Ni	Fe	Cr	Mn	Si	Nb	Ti
%	0.45	32–35	Balance	23–27	2	2	1	—

Incoloy 800H

Element	C	Ni	Fe	Cr	Mn	Si	Nb	Ti
%	0.08	32	45	21	—	—	—	0.04

DISCUSSION

Results of the present investigation establish that the weld suffered from localized carburization in some regions, creep voids/cracks and formation of brittle grey phase at grain boundaries. Evidence for localized carburization are magnetic susceptibility hardness and microstructural changes.

Formation of brittle grey phase at grain boundaries was detected in all the samples examined. However, it was detected in greater amount in weld regions cracked through thickness. This phase was brittle and provided sites for easy crack nucleation and propagation.

The weld metal is nickel base alloy and its chemical composition is given in Table 2a. Decker and Sims [1] have discussed metallurgy of nickle-base alloys. Its matrix structure is FCC austenite and the major second phases normally present are precipitates and carbides. FCC austenite, is a solid solution and among the alloying elements present Cr, Fe and Mo form solid solution, while Cr, Mo and Ti form carbides. The major precipitates phase is gamma prime (γ) in nickel alloys Ni, Al, Ti and Nb.

Microstructural changes observed such as carbides formation within grains and at grain boundaries, particularly in the cracked region of the weld, are due to localized carburization. Segregation of alloying elements at the grain boundaries led to the formation of brittle grey phase.

However, the types of carbides formed need to be identified. Not all the second phase precipitates are carbides. EDAX analysis of rod type precipitates seen in SEM was found to consist of Ni, Cr, Fe and the nature of this phase remains to be identified.

X-ray diffraction ad transmission electron microscopic studies are required to identify second phase precipitates formed.

Localized carburization, grey phase formation at grain boundaries and creep are the factors which emerge from the present study as the causes for the weld failure. Their role in the failure is considered. The partially cracked regions, as illustrated in Figs. 7a, 8a indicated that crack initiation started from the

root of the weld caused by localized carburization and formation of brittle grey phase at grain boundaries. However, crack propagation was caused by the accelerated creep due to increase stresses of the weld with the progress of fracture in the weld as in Fig. 4. The region of the weld where there had been hardly any carburization suffered from creep damage in the form of microcreep cracks/voids induced by higher stresses resulting from decreasing load bearing area. It may be stated that the extent of creep damage observed would have not taken place if stresses have not increased. In this region initiation of root crack and its partial propagation is attributed to the brittle grey phase at grain boundaries Fig. 4.

The region of the weld where there had been hardly any carburization suffered from creep damage in the form of microcreep cracks/voids induced by higher stresses resulting from decreasing load bearing area.

CONCLUSION

- Localized carburization, brittle grey phase formation at grain boundaries and creep are the factors responsible for the weld failure.
- The factors responsible for the fracture initiated from the root of the weld are the localized carburization of the root and formation of brittle grey phase at grain boundaries.
- Propagation of fracture, once initiated in the root of the weld, was assisted by creep and brittle grey phase formation at grain boundaries.

ACKNOWLEDGEMENT

The authors would like to thank the management of the Petroleum Research Centre for their encouragement to present this work and to Ras Lanuf Petrochemical Complex staff for their permission to carry out this work at the Petroleum Research Centre.

REFERENCES

[1] R.F. Decker and C.T. Sims, The Superalloys, (John Wiley and Sons, Inc., 1972), p. 33.
[2] M.W. Mucek, Materials Performance, 1983, vol. 23, No. 9, p. 25.

PRJ, Vol. 6 (January 1994); P. 32–43, 7 FIGS.

COMPARISON: SEMBLANCE SPECTRA AND VELOCITY FUNCTION TECHNIQUES OF VELOCITY ANALYSIS

M.M. Elazezi*

مقارنة طريقتي الأطياف والدوال لتحليل السرعة السيزمية

محمد مسعود العزيزي

أعطى تحليل السرعة السيزمية بإستخدام طريقة الأطياف (Semblance spectra) نتائج أفضل من التي تم الحصول عليها باستخدام دوال السرعة (Velocity functions) ولقد تميزت بالحصول على قيم أعلى لسرعات التكدس (Stacking velocities). تبين من خلال تقييم ومقارنة سرعات التكدس المتحصل عليها باستخدام دوال السرعة مع السرعات المتوسطة (Average velocities) المقاسة من سرود الآبار الواقعة على الخطوط السيزمية أن السرعات المتوسطة أعلى من جميع سرعات التكدس بينما تتباين نسبياً بمقارنتها مع السرعات المتحصل عليها بطريقة الأطياف.

لقد أدى إستخدام طريقة الأطياف إلى تحسن واضح في نوعية المقاطع السيزمية والذي مكن من التعرف بصورة أوضح على بعض الظواهر الجيولوجية مثل الصدوع.

ABSTRACT

The velocity analysis by using the spectra has shown better results than the velocity function technique, besides that the former is characterized by higher stacking velocity values. The stacking velocities obtained from the two techniques were evaluated in relation to the average velocities from wells located on the seismic lines. The comparison shows that all the velocity function values are much lower than the average velocities. The stacking velocities by using velocity spectra vary slightly between lower and higher values than the average velocities.

The raw final stack using velocity spectra show better improvement than the final stack using velocity functions; for example in the recognition of faults.

INTRODUCTION

The basic scheme in velocity analysis has been described by authors such as Taner and Koehler (1969), Neidell and Taner (1971), Al-Chalabi (1979), Robinson (1983), Robinson and Durrani (1986) and Mayne (1962). There are various velocity analysis techniques which are applied by the industry as source of stacking velocity required for dynamic correction, stacking and migration of the seismic traces. Velocity spectra and velocity functions are the most common of these techniques.

The seismic data used in this study were recorded for the Zuetina Oil Company during 1988 from Block 102, Sirt Basin, Libya (Fig. 1). The data were processed by Halliburton Geophysical Service (HGS) using the velocity function technique. The velocity spectra technique, and CMP stack were conducted on the same seismic data. The aim was to derive meaningful stacking and to investigate their accuracy for stacking of seismic sections in comparison with the stacking velocities already picked by HGS. This comparison is to bring out errors in stacking velocity obtained from the velocity function technique.

* Petroleum Research Centre, P.O. Box 6431, Tripoli, G.S.P.L.A.J.

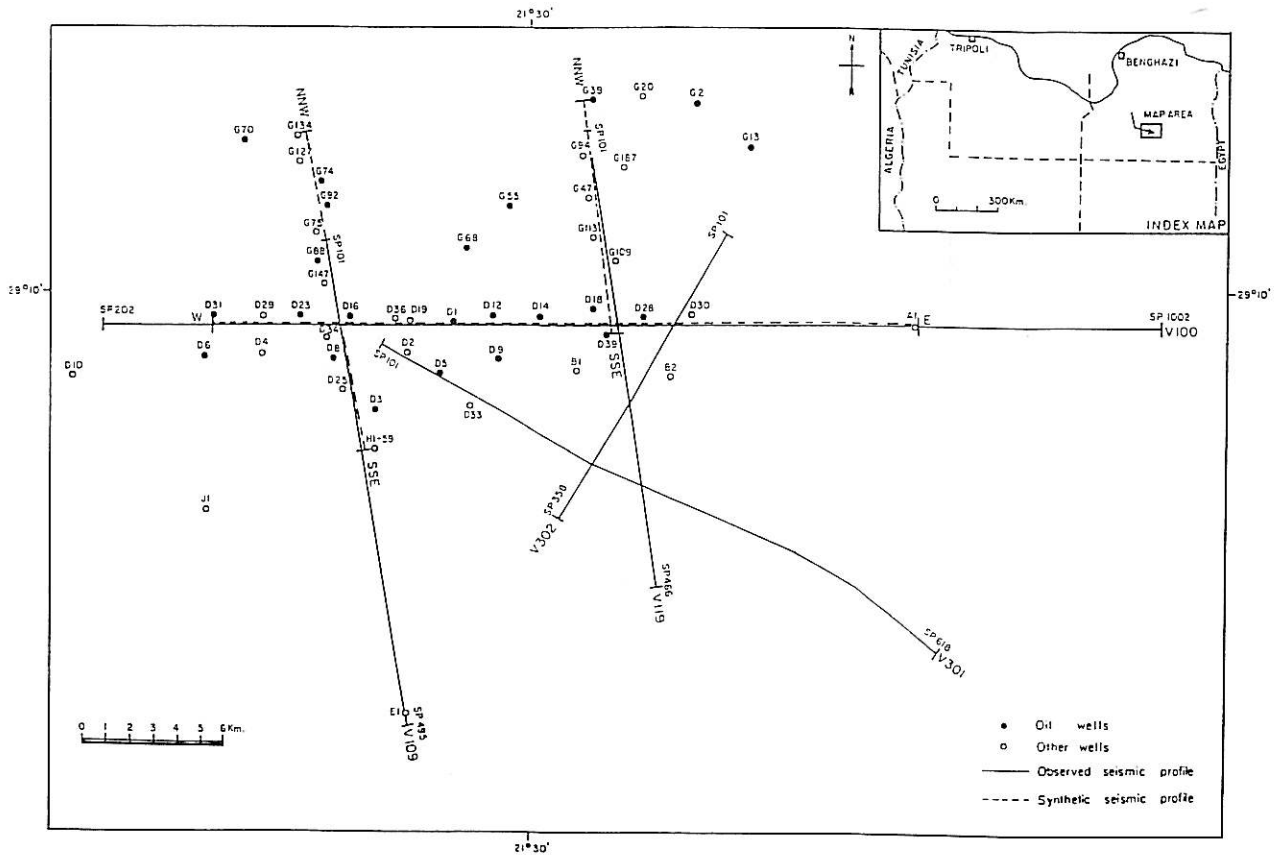


FIG. 1. Location map showing the seismic lines.

VELOCITY ANALYSIS METHODS

1. Velocity Functions and Trial Stacks Method

The Halliburton company's approach consists of selecting a portion of stacked data (23 stacked traces) which have been NMO corrected using 11 velocity values. These values range from the lowest to highest expected velocity (1.600–5.000 km/s). A single trial velocity is used for stacking all events from the beginning to the end of the record. Reflections had their highest amplitude on the stack panels when corrected with the optimum stacking velocity. The display of optimum velocities against the time where each optimum velocity results with highest amplitude, is known as velocity function. Hatton *et al.* (1986) have mentioned the weaknesses of the method which are mainly its lack of resolution in velocity due to the often coarse increment selected for reasons of economy and poor visual dynamic range. Besides, the velocity function technique is heavily dependent on the human's judgement of alignment of the seismic events. Therefore, different processors may not pick the same stacking velocities.

2. Velocity Spectrum Technique

Taner and Koehler (1969) have described a technique which was designed to permit interpretation of stacking velocity Vs as a function of the zero-offset travel time To. The technique involves plotting a measure of trace coherence computed along moveout curves which are defined by discretely sampled values of Vs and To. Their approach consists mainly on the trial of different values of stacking velocity at particular values of normal incidence time to calculate hyperbolic moveout within a short time gate. When the best value of Vs is found the data are corrected with time shifts based on this velocity and stacked together. The velocity spectra are plots of a coherence measure, called semblance, of reflections that exist at times To, having stacking velocities Vs.

a. Semblance

Semblance is a measure of the goodness of the stacked trace within a time gate. It is also defined by Sheriff (1978) as the ratio of energy resulting from a stacking velocity assumption compared to the amount of energy available to be stacked. Semblance

has been described by Al-Chalabi (1979), Robinson (1983), Said (1990) and Hatton *et al.* (1986). Neidell and Taner (1971) have defined it as follows;

$$S_t = \frac{\Sigma_i a_i^2}{\Sigma_i \Sigma_j b_{i,j}^2}$$

where a_i is the ith amplitude of the stacked trace and $b_{i,j}$ is the ith amplitude of the jth trace of the component CMP set. The semblance S_t has a possible range from 0 to 1 ($0 < St < 1$) with perfect comparison corresponding to 1, which depends on whether the traces contain only the signals or contain noise in addition to the signal. This affects the line-up of the reflection events which leads to a decrease in the amplitude of the correct Vs peak power (see Taner and Koehler, 1969; Neidell and Taner, 1971 for details). Different Vs values are calculated at the same To and a plot of semblance versus Vs will show a peak where the correct value of Vs has been used and all the traces have been brought into alignment.

This procedure is repeated for a collection of zero offset times, generally at equally spaced time increments all the way down the CMP gather. The result is called the velocity spectrum at the common midpoint. A curve or contour of power will develop showing the stacked semblance maxima wherever there is appreciable reflection energy and will give spot determinations of Vs and To between which linear interpolation may be made for intermediate travel time.

Not only does the semblance tend to be large when a coherent event is present but the magnitude of the semblance is also sensitive to the amplitude of the event. Strong events exhibit large semblances and weak events exhibit moderate values of semblance whereas incoherent data have very low semblances (Robinson, 1983). Semblance and other coherence measures are used to determine the value of parameters that will optimize a stack. The most important application of semblance is in the computation of a velocity spectrum from which stacking velocity is determined as a function of stacking time (Said, 1990). The velocity that produces the maximum semblance represents the best fitting hyperbola and thus produces the best stack at stacking time. As a result this optimum velocity is called the stacking velocity.

b. Velocity spectra display

Velocity spectra display is one of the most common forms of displaying the result of velocity analysis as described by Al-Chalabi (1979), and Taner and Koehler (1969). Figures 2 and 3 show examples of spectra displays with the coherency buildups. In these displays the coherency value as a function of time and velocity is represented in plots with time varying along the vertical axis and velocity varying along the horizontal axis. The velocity analysis is presented as contours of semblance. The contour in effect brings the values of stacking velocity as a function of arrival time which would result in bringing out events on a stacked section.

The displays are frequently accompanied by numerical tables of the measured coherency values for verifying root mean square velocity (Vrms) estimated from the display and curves for semblance and amplitude (Fig. 3). The velocity analysis program gives a listing of velocity as a function of time at the particular location where the analysis is made.

c. Interpretation of spectra displays

Velocity spectra are used to pick stacking velocities and are considered to be a very convenient method for good quality high volumes of data (Hatton *et al.*, 1986). The interpretation of velocity spectra plots basically involves the identification of coherency build-ups which are caused by primary reflections, and the isolation of those due to multiples and other spurious coherent events. The determination of the velocity function needed for optimum stacking, relies heavily on the build-ups of coherency at each point in the spectrum. Thus it requires high precision in selecting the best coherency which represents the primary reflection events especially in poor quality displays.

The observation of lateral variation in stacking velocities at any particular time interval is essential because a sudden change in velocity between the location of velocity analysis might lead to a change in reflector continuity or strength which could be interpreted as a geological change. Establishing close reference to the seismic section and the CMP record display, when available, is important in identifying the presence and strength of primary reflections at appropriate travel times, and also allows the presence of non-primary events to be checked (Al-Chalabi, 1979).

Well data at the same CMP locations could provide a valuable check for the spectra display through the identification of the main lithological interfaces which are expected to generate the primary reflections. Recognition of non-primary coherency build-ups on the velocity display can be a valuable guide for the processing and interpretation of the seismic section.

The interpretation, especially of good quality data, simply consists of connecting contoured highs that clearly indicate a realistic velocity-time function

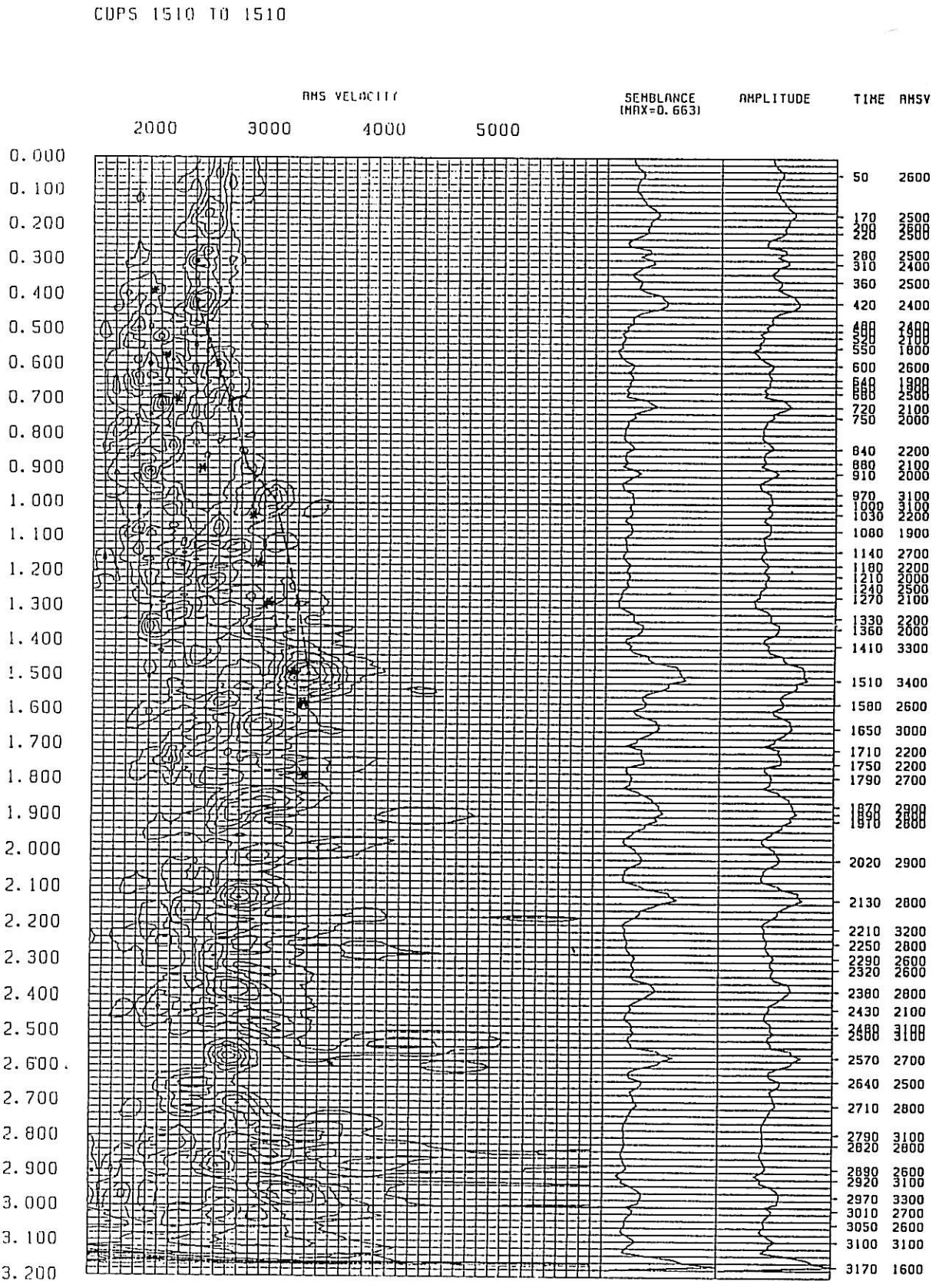


FIG. 2. Display of velocity spectra, CDP 1510, seismic line V100 showing the picking of stacking velocities.
----------= Picked velocity.
* * * * * = HGS picked velocity.

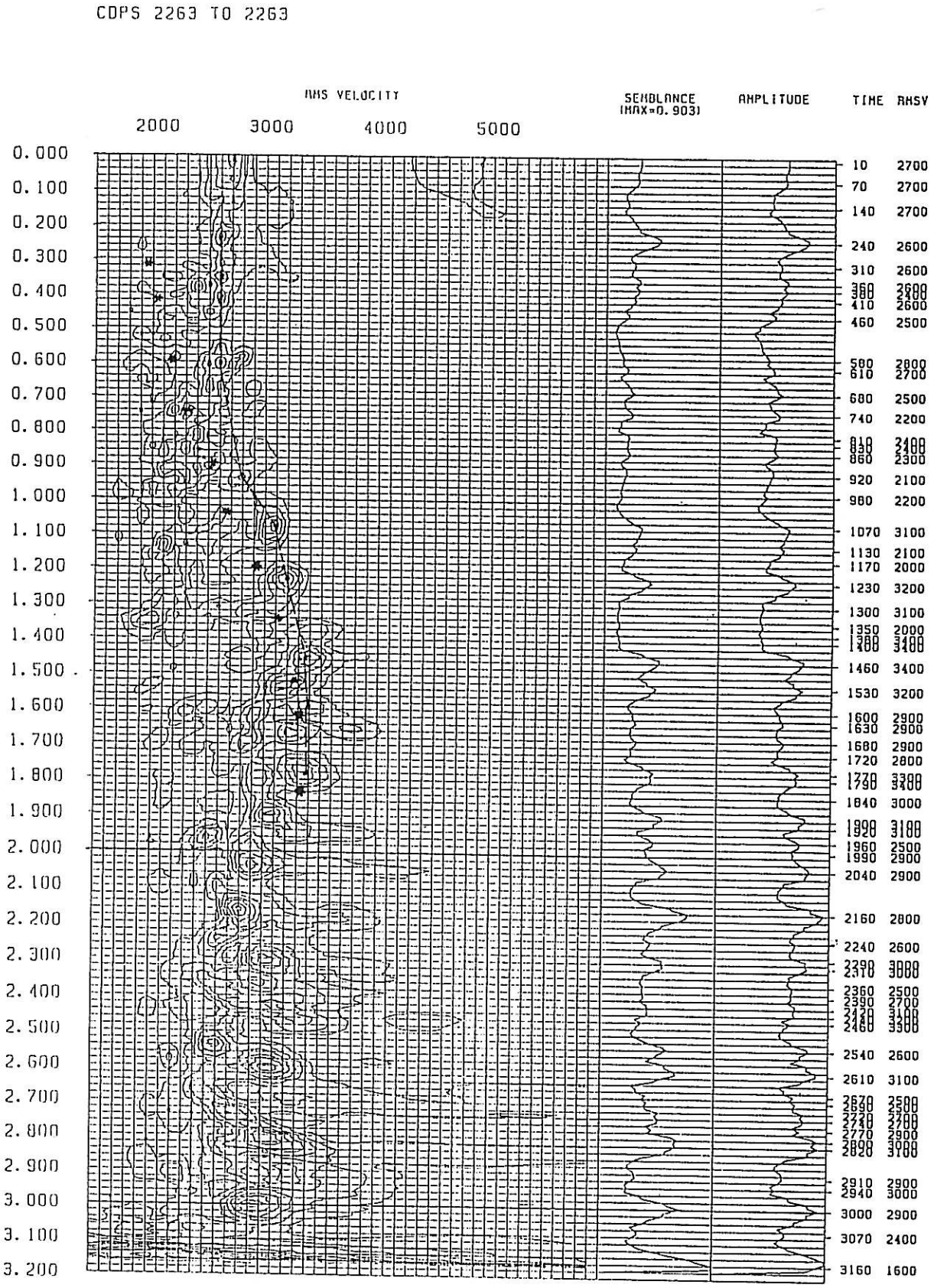


FIG. 3. Display of velocity spectra, CDP 2263, seismic line V100 showing the picking of stacking velocities.
---------- = Picked velocity.
* * * * * = HGS picked velocity.

(Fig. 3). Plots of semblance indicate the location in time of the most coherent events. In case of poor quality data reliable events should be picked first and the gaps should then be filled by comparison with adjacent analyses. Multiples are usually clearly identified in a velocity spectrum display, tending to align nearly vertically beneath the generating primary events.

VELOCITY ANALYSIS OF SEISMIC LINES V100 AND V109

The final display of the data showed that the primary reflection events are affected by the presence of multiples which obscure recognition of main reflectors such as the basement interface. Therefore, the main purpose of conducting velocity analysis was to improve the quality of the primary reflectors of the main reservoir rocks. This can be achieved by recognizing and subsequently attenuating the multiples and other effects. The step was decided after running post-stack deconvolution and the establishment of improved quality data such as the bringing out of a distinctive basement reflector and the reduction of the effect of multiples. The result indicated that the multiples could be partly the result of improperly picked stacking velocities used for the CMP stack.

1. Procedures

The velocity analyses were carried out as follows:

1. Seismic lines V100 and V109 (Fig. 1) were selected for carrying out the velocity analysis. The data were requested in the form of CMP gathers with static correction and pre-stack deconvolution applied. The V100 line consists of 1597 CMP gathers and the analyses were selected at every 50 CMP gathers. The V109 line consists of 768 CMP gathers and the analyses were selected at every 60 CMP gathers.

2. A number of CMP gathers were displayed at different parts of the seismic line in order to check their quality and arrangement. Figure 4 shows an example of such display.

3. The velocity spectrum at each velocity analysis location was derived from 10 CMPs, 5 at each side of the selected CMP in order to reduce the semblance peaks created by noise. Displays of velocity spectra were obtained at the selected CMP locations.

4. The velocity spectra displays were used for picking stacking velocities needed for stacking the seismic sections (Figs 2 and 3). Comparison between these displays was conducted to check the trend of coherency build-ups of the picked velocities.

5. The stacking velocities obtained were used for producing brute stack sections (Fig. 5). The velocities are applied to CMP stacks to check if any improvement could be achieved regarding the primary reflection events, and attenuation of multiples and any other events interfering with the primary reflectors.

6. Comparison is carried out between the new stacking velocities and those picked by the company (Figs 2 and 3) and also between the produced sections and the contractor's final sections (Fig. 5a–b) to check against any error resulting from procedure, interpretation, or computation of the stacking velocities which are suggested by the presence of multiples in the contractor's final sections.

7. Average velocities measured from well data of well A1 are used for evaluating both the new and the contractor's picked stacking velocities as shown in Fig. 6.

2. Data Interpretation

a. Velocity spectra

Velocity displays were interpreted by picking the readily recognizable primary coherency build-ups. The picking out was at the high velocity edge of data which represents mainly the primary reflections. The stacking velocity functions were obtained by connecting those build-ups. Figure 2 shows a typical velocity spectra display computed from 0.100 sec to 3.200 sec for velocities varying from 2.500 km/s to 3.500 km/s at 0.100 km/s intervals. Coherency representing the primary events are characterized by displacement in the direction of increasing time. It has a maximum time limit down to about 1.50 sec. Stacking velocities are obtained by connecting the interpreted primary energy arrivals. The spectra also show that multiple energy started around 0.400 sec to 3.200 sec. These multiples are of lower velocities than the primary events and align nearly vertically especially around 1.650 to 3.200 sec. The coherency buildup of the basement reflector was confirmed by comparison with the available well data of well D1–102 (754.5 ms OWT) which has defined the time limit of the primary events at around 1.500 sec. Figures 2 and 3 show that the contours become increasingly stretched along the velocity axis, with increasing travel time. This stretching represents a deterioration in the sensitivity of the coherency measure with increasing time and causes a loss in resolution. It results from the fact that with increasing time, large stacking velocity changes correspond to increasingly smaller NMO changes and low frequencies become increasingly predominant.

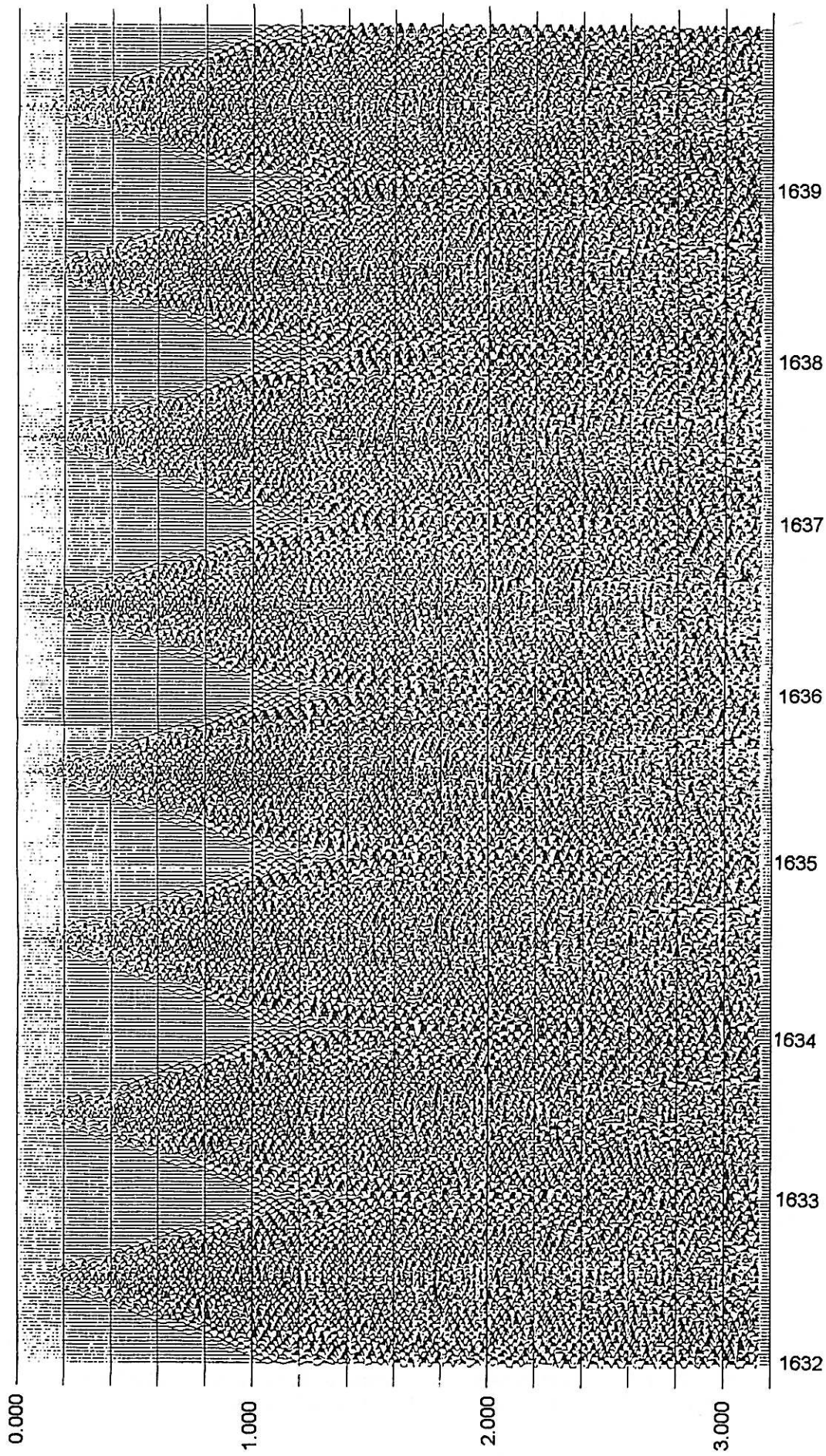


FIG. 4. Display of CDP gathers from seismic line V100, to check their quality and arrangements along the line. The display is showing good quality data.

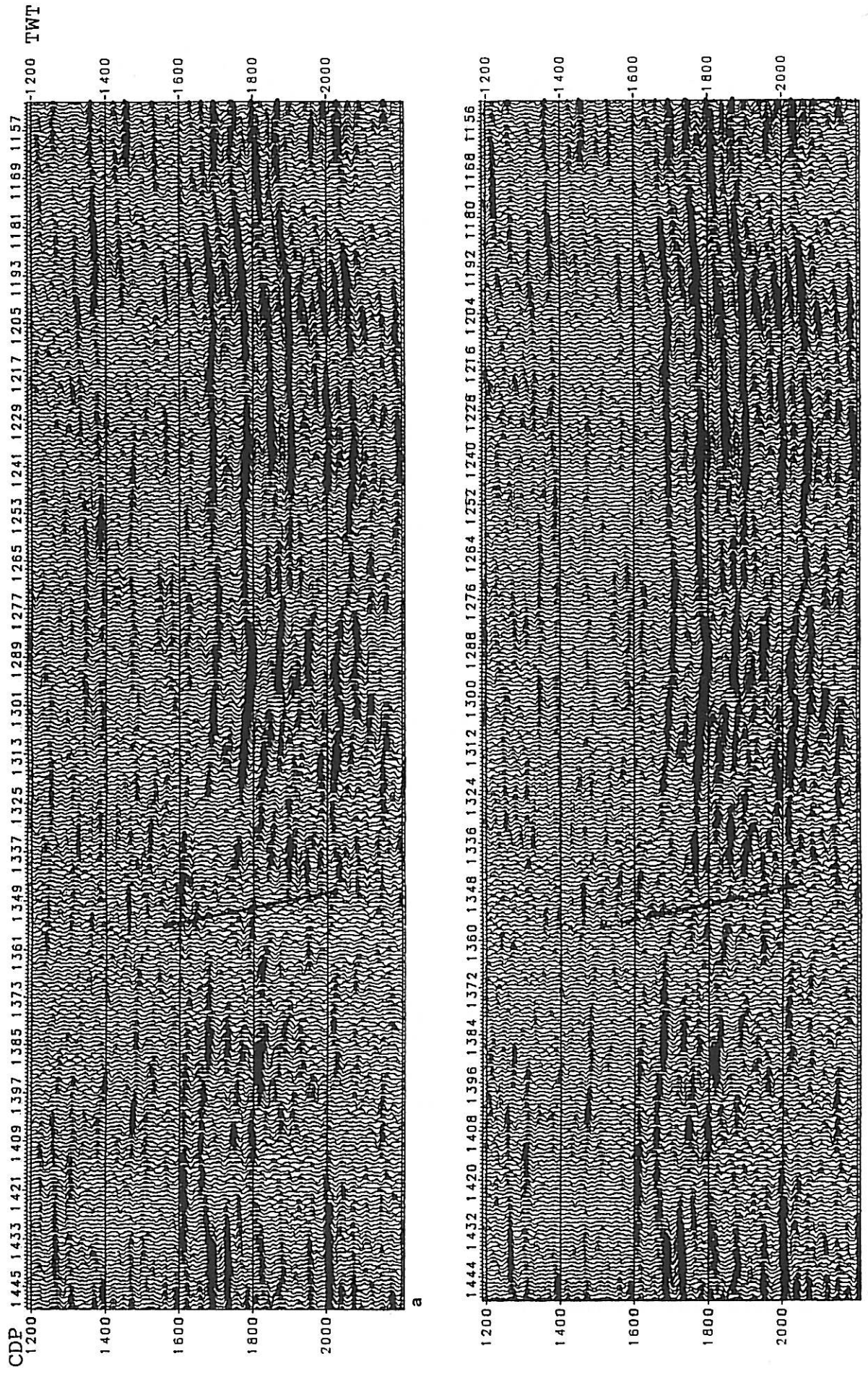


FIG. 5. Part of seismic section V109. (a) final section stacked by using the contractor's picked velocity. (b) Raw final section stacked by using newly picked stacking velocity.

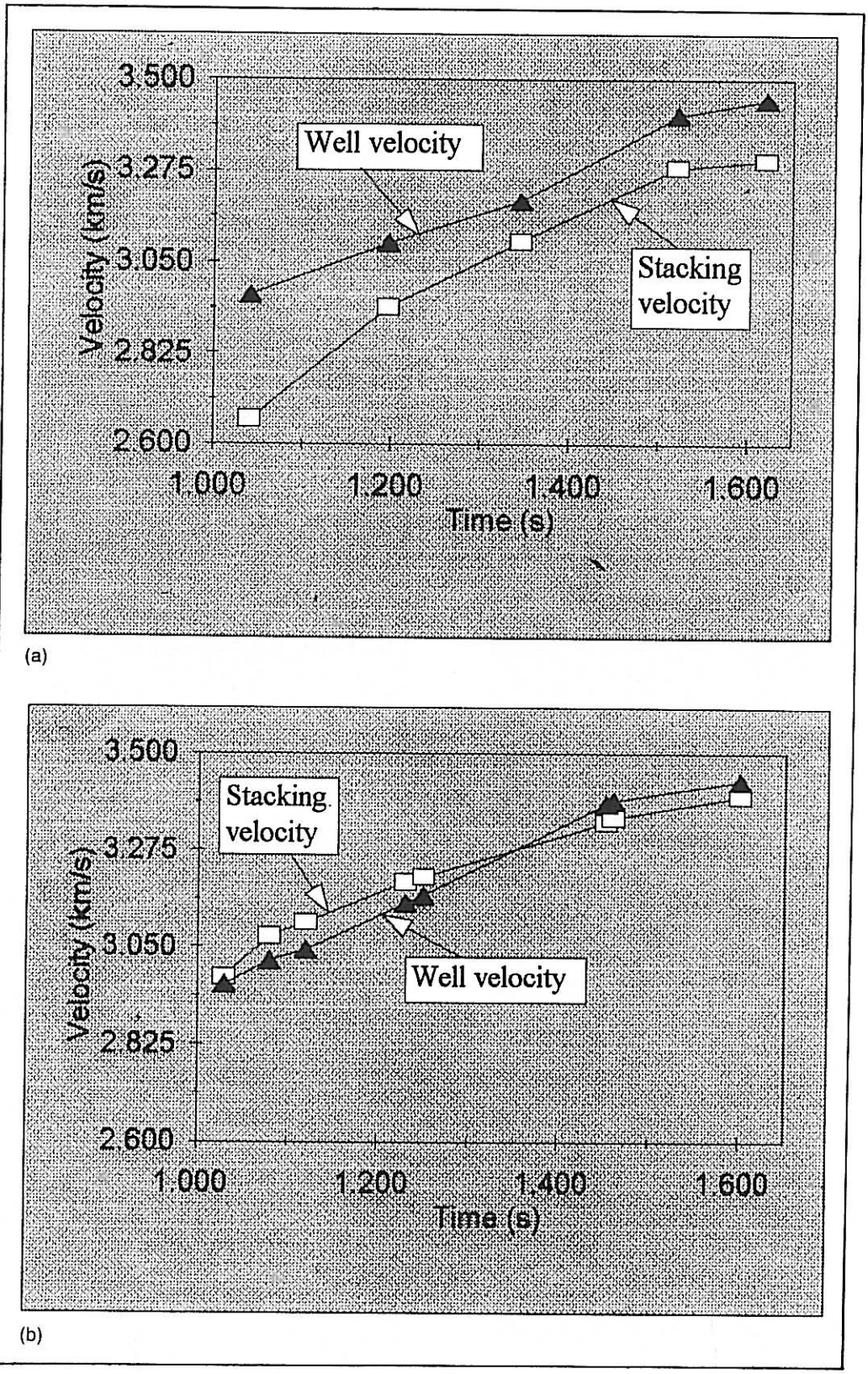


FIG. 6. Comparison between the average velocities measured from well A1 and stacking velocities. (a) Contractor's picked stacking velocity; (b) Repicked stacking velocities. □ = Stacking velocity, ▲ = Well velocity.

The contractor's picked stacking velocities are plotted on the velocity spectra (Figs. 2 and 3) to show the differences between the picked velocities which are expected to represent the primary reflection events.

b. Comparison with the contractor's final sections

An example of the noticeable improvement in the raw final stack section is shown in Fig. 5 which

represents a part (between CMPs 1151–1449) of seismic section V109. Fig. 5b shows that the multiples generally became weak or attenuated all over the section and in particular at the lower part between TWT 1800 and 2000 ms. There is also evidence of weakening of multiples at the interval between CMPs 1372 and 1410, and TWT 1600 and 1800 ms. This could be partly a result of improperly picked stacking velocities.

Another example of the improvement (Fig. 5b) is the sharpness and better continuation of the reflection event between CMPs 1358 and 1449 and TWT 1450 and 1480 ms, and also between CMPs 1180 and 1332, and TWT around 1470 ms. There is a clear fault in this part of the section between CMPs 1353 and 1347, and TWT 1400 and 1800 ms, which is much better defined in the raw final stack section.

c. Comparison with well data

It has been mentioned (Dix, 1955; Taner and Koehler, 1969) that the root mean square velocity (Vrms) is generally about 2% higher than the average velocity unless affected by other factors such as dipping and is generally 1% lower than stacking velocity.

The contractor's stacking velocities and the newly picked stacking velocities are compared with the average velocities computed from well data of well A1–102 as shown in Fig. 6. At A1 well location a plot of average and interval velocities against depth is used to measure the average velocities at the selected picked time positions. Comparison between stacking velocities and average velocities measured from velocity logs is carried out. As shown in Fig. 6a the contractor's picked Vrms are lower than the average velocities computed from data of well A1. The velocities are different by an average of 0.169 km/s. Figure 6b shows that the newly picked Vrms for the five TWT between 1030–1250 ms are higher than the average velocity from A1 well by 0.046 km/s. For the three TWT between 1452–1600 ms, the Vrms are lower by 0.040 km/s.

MUTING

The mute is generally considered to be a necessary part of the processing sequence, and it is usually applied before velocity analysis. It is carried out to cut off refraction and noise caused by geometric and other effects on the far traces. Muting has been described by Dobrin and Savit (1988) as eliminating or suppressing a portion of the recorded data, and can be divided into three main types: first break muting, NMO stretch muting, and inner trace muting.

Yilmaz (1987) has mentioned that as a result of NMO correction, traces are stretched in a time-varying manner causing their frequency contents to shift towards the low end of the spectrum. Frequency distortion increases at shallow times and large offsets. Therefore, muting before stacking is required to prevent degradation especially of the shallow events. Mute produces lower fold data near the surface part of the section and it can be a few hundred milliseconds before the data is full fold. Normally this would be critical in the interpretation of shallow reflections where the fold is low.

Mute was performed by picking one of the CMP gathers at the start of the seismic section as shown in Fig. 7. The available velocities (Vrms) at the CMP location were then used for NMO correction. Display of the CMP after the correction was applied, was then used to mark the part of the CMP to exclude the shallow reflections at large offsets at the upper part of the CMP until about 200 ms TWT. The plot was then used to obtain the offset and time according to the picked points along the line which defines the mute. The last point should be the maximum offset in order to obtain smooth mute.

STACKING

Stacking is one of the important applications of seismic data processing in improving data quality. The CMP stacking method is used because of the redundancy in the multiple coverage method applied in seismic prospecting (Mayne, 1962). Stacking relies heavily on the velocity derived from velocity analyses. The NMO correction puts all the corrected traces into alignment and produces one output trace for each CMP gather. This composite trace is called the stacked trace for that midpoint and collection of all the traces forms the stacked section. The primary reflections stack constructively while multiples tend to stack destructively because the reflection times of multiple reflections generally increase faster with increasing shot-receiver distance than do those of primary reflections with the same vertical time. The newly picked stacking velocities produced from the velocity analyses of the CMPs along the seismic lines were used for obtaining brute stack displays (Fig. 5b). The sections are used for comparison with the contractor's final seismic sections (Fig. 5a) in order to find out if the previous velocity analysis was unsatisfactory.

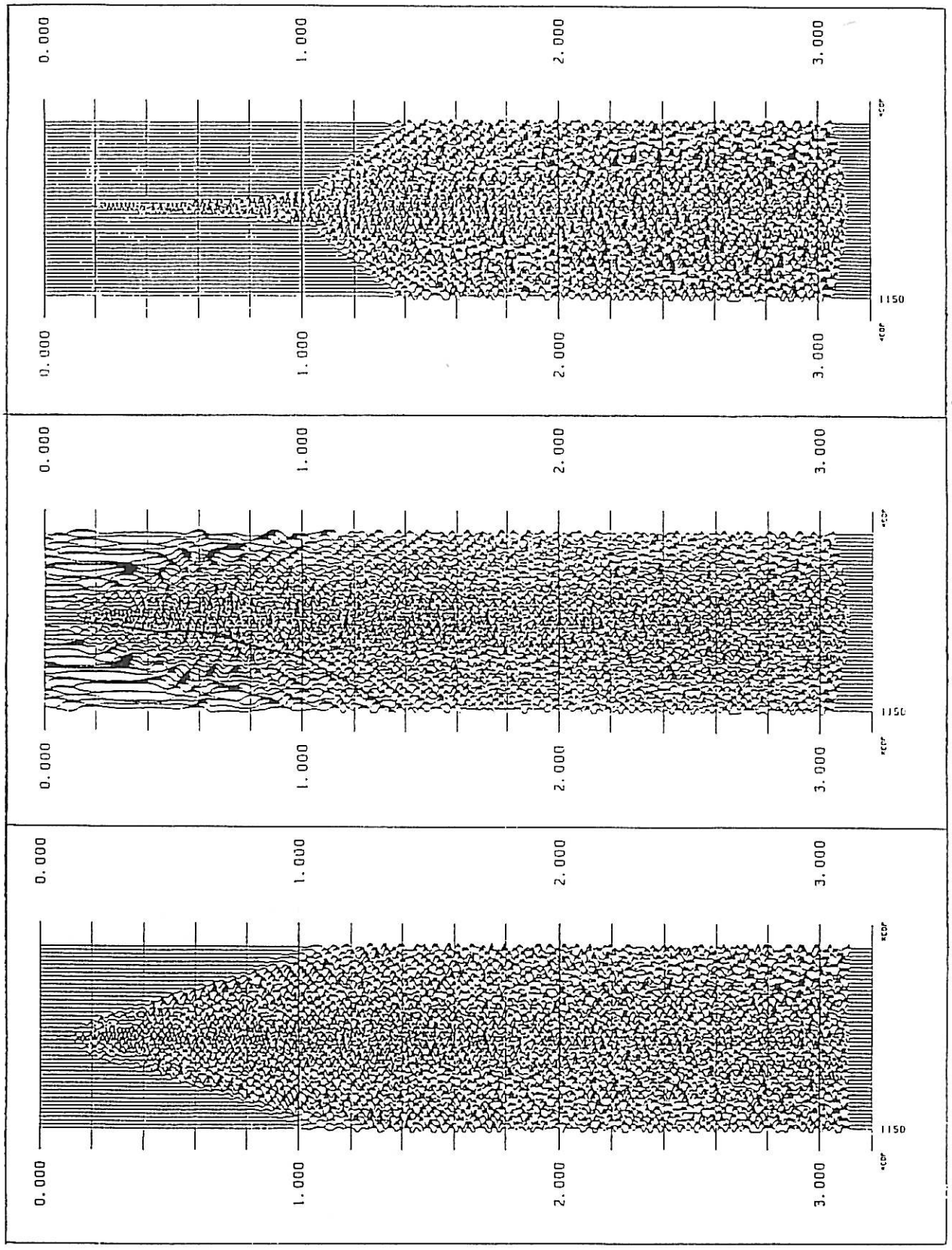


FIG. 7. CDP gather 1150, seismic line V100. (a) Before NMO; (b) NMO applied and the excluded part is marked; (c) After NMO and mute is applied.

DISCUSSION

The displays of velocity analysis of the selected CMPs show the picking of velocity when strong coherency build-ups exist. Such coherency, which represents the stacking velocities of the primary reflection events is more convincing than the velocity picked by using the velocity functions technique (Figs 2 and 3). Comparison of the velocity spectra have shown similarity in the trends of coherency build-ups at the selected locations along the seismic sections.

Comparison between the contractor's and the newly picked stacking velocity (Figs 2 and 3) shows that the newly picked coherency build-ups which represent the stacking velocities are characterized by higher values and are more convincing than the contractor's velocities.

The raw final stack sections were compared with the contractor's final sections (Fig. 5). They showed better improvement regarding the sharpness of the primary reflection events and the attenuation of the multiples which already existed in the final section. The variations between the raw stack and final sections could be taken as an indications of the effect of stacking velocity on reflection events. Indications for presence of a fault are shown in both sections. The fault in the raw final stack section can be recognized and sharply defined more easily than in the contractor's final section where scattered events obscure the main features of the fault.

Figure 6 indicate that the differences between the contractor's stacking velocities and the average velocities from well data are much greater than those between the newly picked velocity values and the same well data.

The attempted comparison suggests that the newly picked stacking velocities are much more representative than those picked by the contractor.

ACKNOWLEDGEMENTS

I would like to thank the management of the Petroleum Research Centre for permission to publish this paper. I am grateful to Dr W. Ashcroft for valuable suggestions during the preparation of this work.

REFERENCES

Al-Chalabi, M., 1979. Velocity determination from seismic reflection data. Fitch, A.A. (ed.) 1979. Developments in geophysical exploration methods – 1. Applied Science Publishers Ltd., London.

Dobrin, M.B. and Savit, C.H., 1988. Introduction to geophysical prospecting (4th ed.). McGraw-Hill Book Company, Singapore.

Hatton, L., Worthington, M.H. and Makin, J., 1986. Seismic data processing: Theory and practice, Blackwell, Scientific Publisher, London.

May, B.T. and Straley, D.K., 1979. Higher-order moveout spectra. Geophysics, 44,1193–1207.

Mayne, W.H., 1962. Common-reflection-point horizontal data stacking techniques. Geophysics, 27, 927–938.

Neidell, N.S. and Taner, M.T., 1971. Semblance and other coherency measures for multichannel data. Geophysics, 36, 482–497.

Robinson, A.E. and Durrani, T.S., 1986. Geophysical signal processing. PHI publisher, p. 481.

Robinson, A.E., 1983. Seismic velocity analysis and the convolutional model IHRDC publisher, p. 290.

Said, E.K., 1990. Development of seismic velocity analysis software. MSc. thesis (Unpubl), University of Glasgow.

Taner, M.T. and Koehler, F., 1969, Velocity spectra – digital computer derivation and applications of velocity functions. Geophysics, 34, 859–881.

Yilmaz, O., 1989. Velocity-stack processing. Geophysical Prospecting, 37, 357–382.

Yilmaz, O., 1987. Seismic data processing. Investigations in geophysics, Vol. 2, S.M. Dohety (Ed.). Society of Exploration Geophysicist.

PRJ, Vol. 6 (January 1994); P. 44–51, 9 FIGS.

HILBERT TRANSFORM AND IMAGE SHARPENING TECHNIQUES AS A TOOL OF INTERPRETING 3-D POTENTIAL FIELD (GRAVITY) DATA

A.M. Ushah*

استخدام محول هلبرت وتقنيات وضوح الصورة في تفسير معلومات الجاذبية

عبد الرزاق محمد أوشاح

تعرض هذه الورقة دراسة تحليلية وعددية بطريقة محول هلبرت ذي البعدين وتطبيقه على معلومات الجاذبية من مصادر (أجسام) ذات ثلاثة أبعاد.

هذا وقد تم التطرق إلى العلاقات الرياضية التي تمثل محول هلبرت كدالة في الزمن وكدالة في التردد، وكذلك العلاقات الرياضية التي تمثل شذوذ الجاذبية للمصادر تحت السطح، بالإضافة إلى بعض العلاقات الأخرى مثل مرشحات المرور العالية المثالية، المشتقة الأولى والثانية سواء كانت الرأسية أو الأفقيتين لشذوذ الجاذبية.

إن استخدم تقنيات وضوح الصورة (Image sharpening) للمشتقة الرأسية الثانية، لشذوذ الجاذبية، الناتجة عن مجموعة مصادر ذات أسطح مستطيلة متوازية، يعتبر مفيد جداً في تتبع ومعرفة حواف وحدود هذه المصادر.

ABSTRACT

The paper presents an analytical and numerical study of two-dimensional (2-D) Hilbert transform method as applied to the three-dimensional (3-D) potential field (gravity) data for interpretation and image sharpening. The relations of two-dimensional (2-D) Hilbert transform in time and frequency domains are presented and a numerical algorithm package has been developed.

Application of 2-D Hilbert transform in quantitative interpretation of gravity anomalies due to multiprismatic bodies as well as their derivatives are investigated and used to test the 2-D Hilbert transform technique. The results achieved by using this relatively new technique are excellent.

Image sharpening techniques of the second vertical derivative of gravity effect due to multiprismatic bodies are useful primarily as an enhancement tools for highlighting edges in an image. These techniques can be achieved either by differentiation or by highpass filtering.

* Petroleum Research Centre, P.O. Box 6431, Tripoli, G.S.P.L.A.J.

INTRODUCTION

This paper deals with the application of 2-D Hilbert transform, to problems associated with the interpretation of three dimensional potential field (gravity) data, and image sharpening (as enhancement tools).

The 2-D Hilbert transform expressions were derived by Bose and Prabhu (1974) in several forms such as cotangent, sine and matrix forms whereas Nabighian (1984) used 2-D signum function.

A closed expression developed for the gravitational attraction of a prism was derived by Nagy (1966) which is valid for any point outside of or on the boundary of the prism, and this was later modified by Goodacre (1973). This expression is extended to multiprismatic bodies and simplified by Ushah (1988).

The discussion is extended to image sharpening of the second vertical derivative in the spatial and frequency domains by differentiation and by highpass filtering respectively. In the spatial domain, the theory of the gradient approach is derived, which is most commonly used in image processing applications as

an enhancement tool for edge detection. In frequency domain, the ideal highpass filter, which attenuates the low-frequency components without disturbing high-frequency components in the Fourier, transform is discussed.

THEORY OF HORIZONTAL AND VERTICAL DERIVATIVES OF A 3-D POTENTIAL FUNCTION AND 2-D HILBERT TRANSFORM

The 2-D Hilbert transform can be expressed in several forms, such as cotangent, sine and matrix forms (Bose and Prabhu, 1979). The 2-D Hilbert transform operator in cotangent form (Fig. 1) is given below as:

$$ht(i,j)=\frac{2}{N_1N_2}\cot\frac{\pi}{N_1}i+\frac{2}{N_1N_2}\cot\frac{\pi}{N_2}j \qquad (1)$$
$$=ht_1+ht_2$$

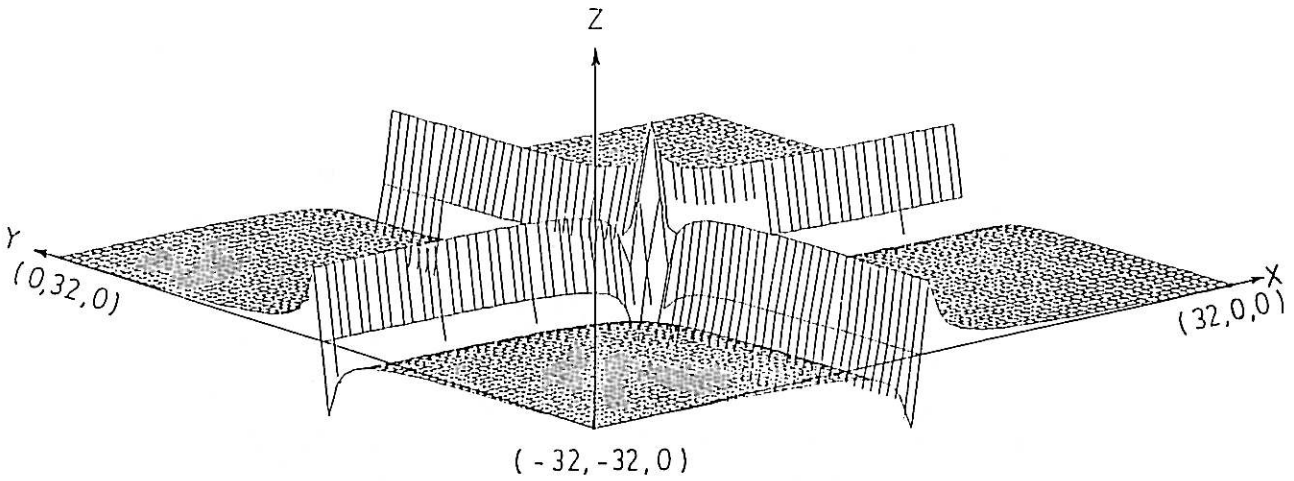


FIG. 1. Two dimensional Hilbert transform as obtained by using the cotangent form (equation 1).

where

$$ht_1=\frac{2}{N_1N_2}\cot\frac{\pi}{N_1}i, \quad ht_2=\frac{2}{N_1N_2}\cot\frac{\pi}{N_2}j$$

$(i=0,1,2,\ldots,N_1-1)$

$(j=0,1,2,\ldots,N_2-1)$

In frequency domain, the 2-D Hilbert transform can be expressed as (Nabighian, 1984):

$$H(p,q)=-j\,\mathrm{sgn}(p,q)=H_1\widehat{ex}+H_2\widehat{ey} \qquad (2)$$

where

$$\mathrm{sgn}(p,q)=[p/(p^2+q^2)^{1/2}]\widehat{ex}+[q/(p^2+q^2)^{1/2}]\widehat{ey}$$

$(j=(-1)^{1/2})$

$\widehat{ex}$ and $\widehat{ey}$ are the unit vectors in the x and y directions, and

$$H_1=-jp/(p^2+q^2)^{1/2} \quad \text{and} \quad H_2=-jq/(p^2+q^2)^{1/2}.$$

If M is a 3-D potential function, then, the relationship between the horizontal and vertical derivatives of M and the 2-D Hilbert transform may be written as:

$$F[\mathrm{d}M/\mathrm{d}z]=H_1F[\mathrm{d}M/\mathrm{d}x]+H_2F[\mathrm{d}M/\mathrm{d}y] \qquad (3)$$

$$F[\mathrm{d}^2M/\mathrm{d}z^2]=H_1F[\mathrm{d}^2M/\mathrm{d}z\mathrm{d}x]+$$
$$H_2F[\mathrm{d}^2M/\mathrm{d}z\,\mathrm{d}y] \qquad (4)$$

where F is the Fourier transform, $\mathrm{d}M/\mathrm{d}z$ is the vertical derivative of M, $\mathrm{d}M/\mathrm{d}x$ and $\mathrm{d}M/\mathrm{d}y$ are the horizontal derivatives of M, in x and y directions, respectively, and $\mathrm{d}^2M/\mathrm{d}z^2$ is the second vertical derivative of M.

It is worth mentioning at this point that the numerical computation of equations (3) and (4) are stable because both H_1 and H_2 are well behaving operators with values not exceeding ± 1.

GRAVITATIONAL ATTRACTION OF MULTIPRISMATIC BODIES

The expression for the gravitational attraction of multiprismatic bodies at a point of observation x, y and z can be written as:

$$Gt(x,y,z)=\gamma\sum_{t=1}^{N}\rho_t(br_{t_1}+br_{t_2}+br_{t_3}) \qquad (5)$$

where $Gt(x,y,z)$ is the vertical attraction of t prisms at a point (x,y,z), ρ is the density of the prism, N is

the number of the respective prism, and γ is the gravitational constant

$$br_{11} = \left|\left|\left| u \arcsin[v/u^2+w^2)^{1/2}] \right|_{x-u_1}^{x-u_2} \right|_{y-v_1}^{y-v_2} \right|_{z-w_1}^{z-w_2}$$

$$br_{12} = \left|\left|\left| v \arcsin[u/v^2+w^2)^{1/2}] \right|_{x-u_1}^{x-u_2} \right|_{y-v_1}^{y-v_2} \right|_{z-w_1}^{z-w_2}$$

$$br_{13} = \left|\left|\left| -w \arctan[v/w(u^2+v^2+w^2)^{1/2}] \right|_{x-u_1}^{x-u_2} \right|_{y-v_1}^{y-v_2} \right|_{z-w_1}^{z-w_2}$$

In equation (5), the terms in each bracket correspond to a particular prism (Ushah, 1988).

SOME EXAMPLES OF GRAVITATIONAL ATTRACTION OF MULTIPRISMATIC BODIES

The vertical component of the gravity field due to five prismatic bodies Fig. 2 is obtained by using equation 5. The horizontal sides of the Prism 1 extend 14 by 14 pixels and its center at (32, 32) pixel. Prism 2 has 12 pixels length in x and y directions and its center at (16, 48) pixels. Prism 3 has 2 units less than Prism 2 in each horizontal dimension and its center at (48, 16) pixel. Prism 4 and Prism 5 have horizontal dimensions 8 by 8 and 6 by 6 units and their centers at (16, 16) and (48, 48) pixels, respectively. The depths to the top of all the prisms in this model is equal 2 units below the surface of observation. Figures 3 and 4 represent the first and second vertical derivatives obtained by using equations 3 and 4 respectively. From these figures the boundaries of the prisms in the model are very clear and can be determined easily especially from the second vertical derivative (Fig. 4).

Figures 5 and 6 are other examples which are tested by increasing the depths of all the prisms to 5 units below the surface of observation.

IMAGE SHARPENING

In this section two methods of sharpening techniques (Gonzales and Wintz, 1977) are discussed, which can be considered as enhancement tools to outline the boundary for the subsurface bodies. They

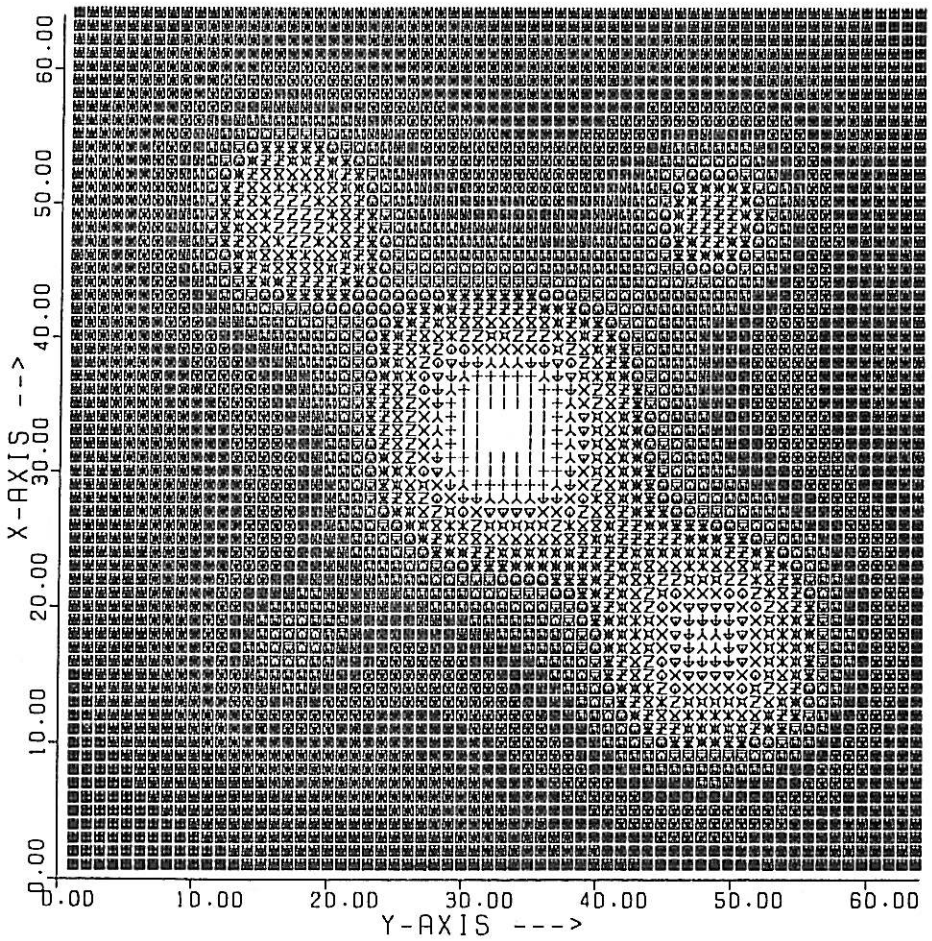


FIG. 2. Example of theoretical gravity effect due to five prismatic bodies; the image displayed with 64 by 64 pixels. $h_1 = 2.0$ for all prisms.

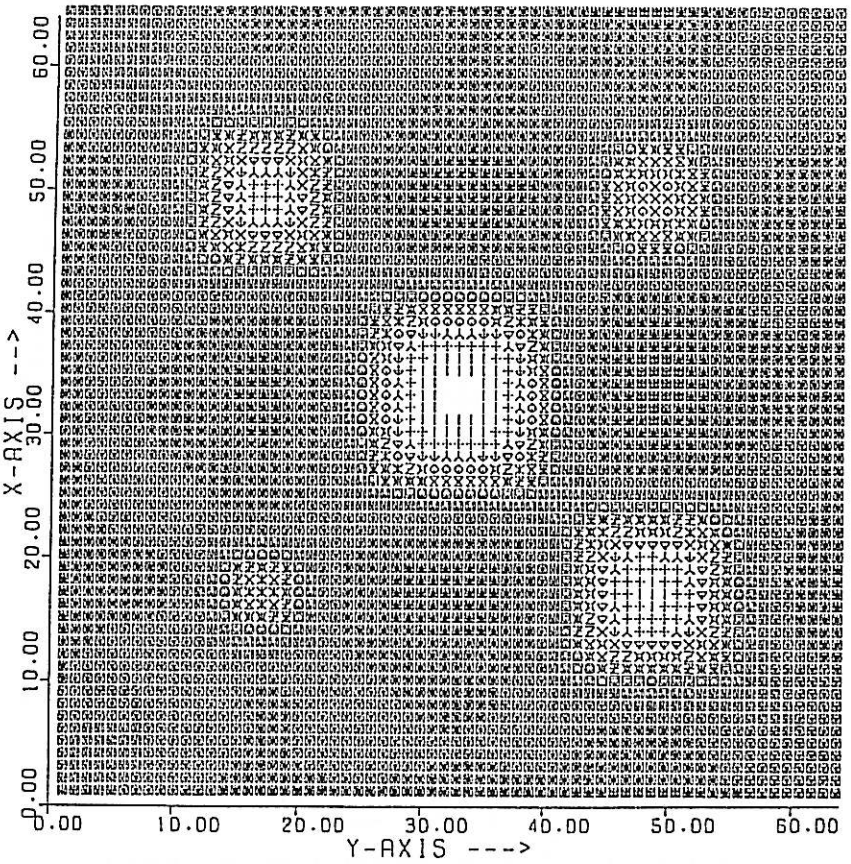


FIG. 3. First vertical derivative of the gravity effect obtained by using 2-D Hilbert transform.

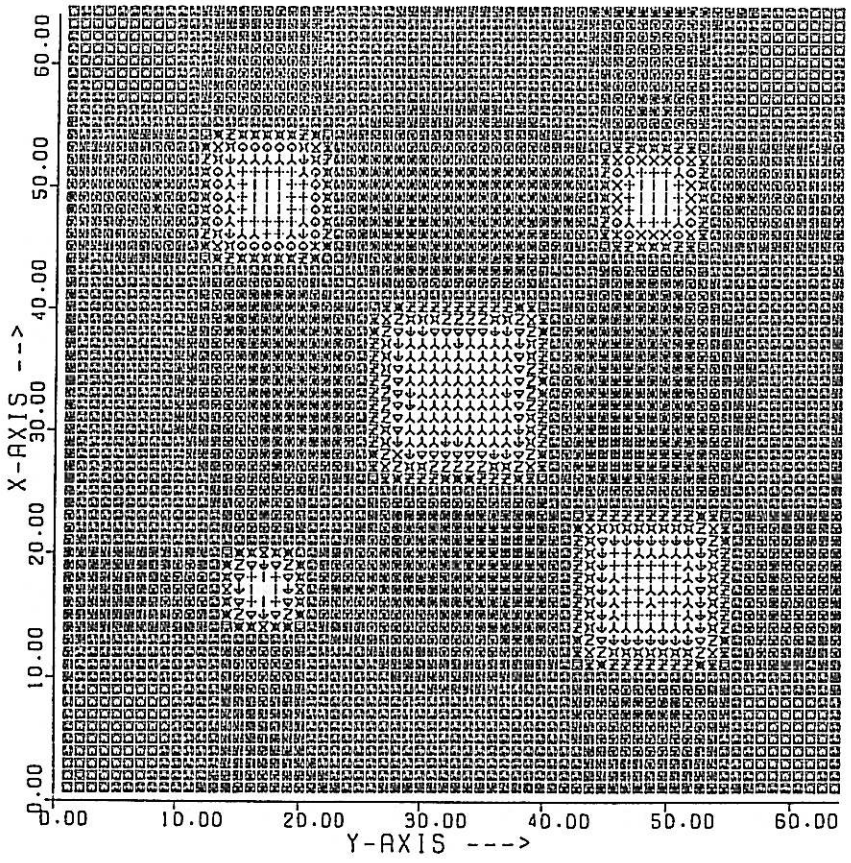


FIG. 4. Second vertical derivative of the gravity effect obtained by using 2-D Hilbert transform (equation 4).

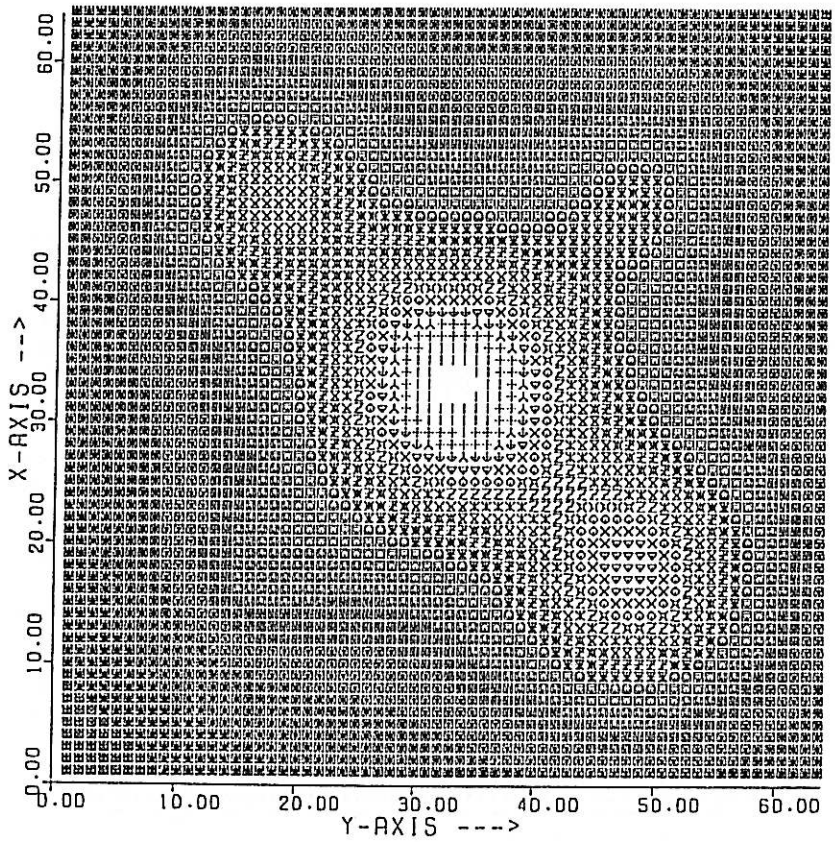


FIG. 5. Example of theoretical gravity effect due to five prismatic bodies; the image displayed with 64 by 64 pixels. h_1(depth) = 5.0 for all prisms.

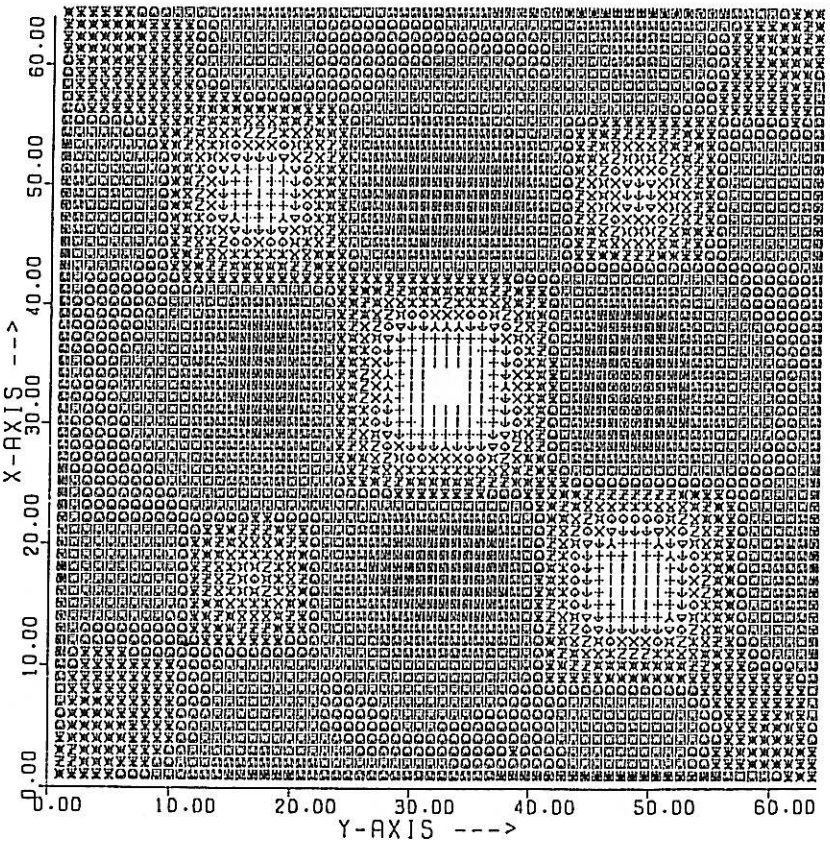


FIG. 6. Second vertical derivative of the gravity effect obtained by using 2-D Hilbert transform (equation 4).

are sharpening by differentiation and highpass filtering.

Sharpening by Differentiation

The most commonly used method of differentiation in image processing application is the gradient ($G[f(x, y)]$), which can be expressed as:

$$G[f(x, y)] = \text{mag}[G] = \left[\left(\frac{df^2}{dx} + \frac{df}{dy}\right)^2\right]^{1/2} \tag{6}$$

For a digital image, the derivatives in equation 6 are approximated by differences. One typical approximation is given by the relation

$$G[f(x, y)] = [[f(x, y) - f(x+1, y)]^2 + [f(x, y) - f(x, y+1)]^2]^{1/2} \tag{7a}$$

Similar results are obtained by using absolute values, as follows:

$$G[f(x, y)] = |f(x, y) - f(x+1, y)| + |f(x, y) - f(x, y+1)| \tag{7b}$$

This formulation is more desirable for a computer implementation of the gradient.

The disadvantage of equations 6 and 7 is that all smooth regions in $f(x, y)$ appear dark in $G[f(x, y)]$ because of the relatively small values of the gradient in these regions. One solution to this problem is to form a new function $g(x, y)$ as follows:

$$g(x, y) = \begin{cases} G[f(x, y)] & \text{if } G[f(x, y)] \geq T \\ f(x, y) & \text{otherwise} \end{cases} \tag{8}$$

where T is a nonnegative threshold. By selecting suitable value for T, it is possible to emphasize significant edges without obsecuring the characteristics of the smooth backgrounds.

Finally, if only the location of edges is of interest, the relation becomes

$$g(x, y) = \begin{cases} LG & \text{if } G[f(x, y)] \geq T \\ LB & \text{otherwise} \end{cases} \tag{9}$$

where LG and LB are specified gray levels for edges and the background.

The properties of the gradient are relatively large for the prominent edges in an image, and small values in regions that are fairly smooth, being zero only in

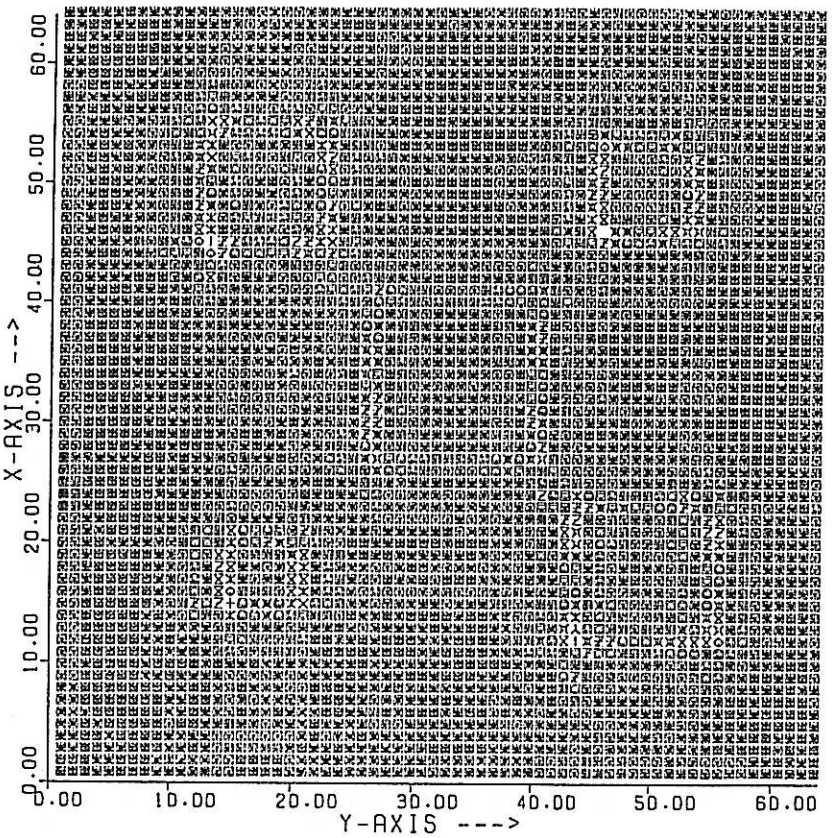


FIG. 7. Example of image sharpening by differentiation of Fig. 4. Illustration of edge enhancement by gradient techniques (equation 7b).

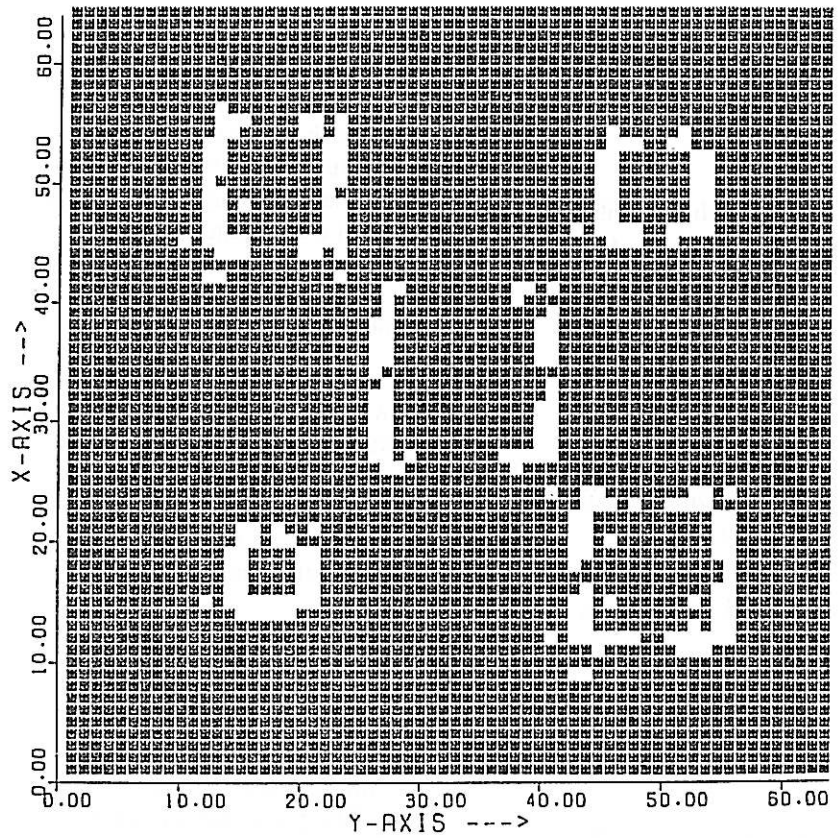


FIG. 8. Represents the edge effect detection (equation 9) with a nonnegative threshold (T)=10.

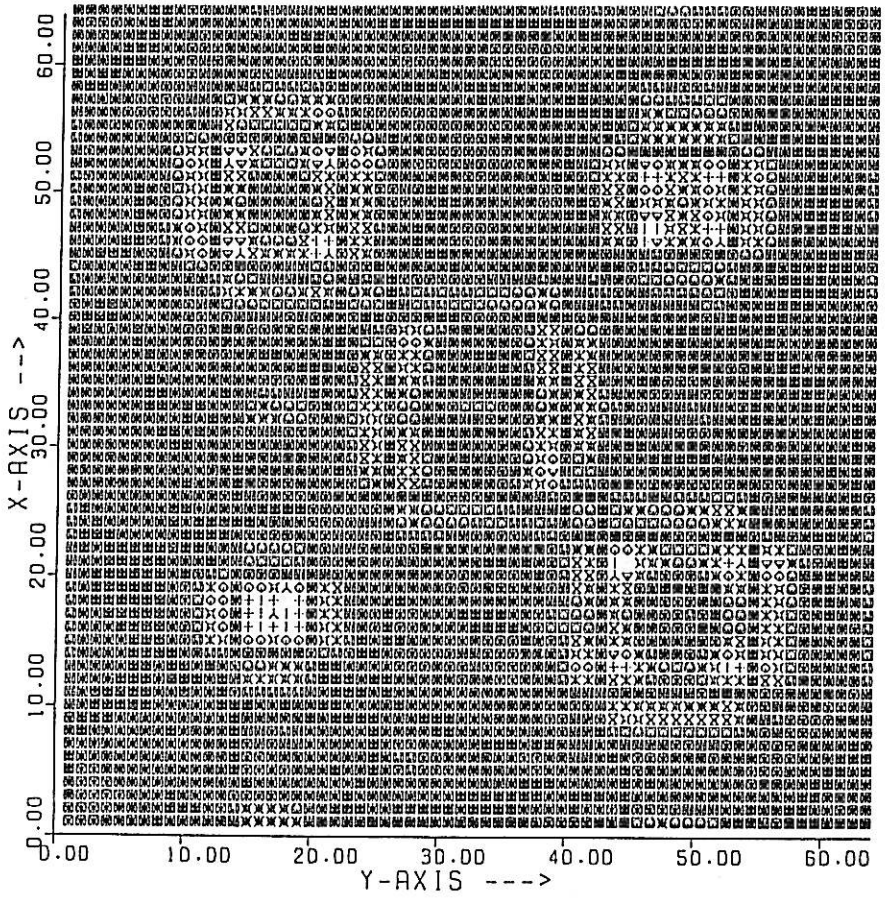


FIG. 9. Image sharpening achieved in the frequency domain by highpass filtering.

regions with constant gray level. These properties are illustrated in Figs. 7, 8 and 9. As shown in Fig. 7, the gradient operation (equation 7b was used) reduces all the constant white regions to zero (black), leaving only the points associated with abrupt changes in gray level (in this case the edge boundaries of the prisms).

Figure 8 is the result of using the gradient scheme given by equation 9 with $T=10$, $LG=32$ and $LB=1$. We notice that considerable amount of small segments appear in the resulting image, with the strongest intensities taking place around the border of the prisms. This is an expected result since the magnitude of the gradient is proportional to changes in gray levels and should be more prominent in regions of an image containing distinct edges.

Highpass Filtering

It is well known that an image can be blurred by attenuating the high-frequency components. Since the high-frequency components can be detected on the edges and other abrupt changes in gray levels, therefore, image sharpening can be achieved in frequency domain by a highpass filtering process which attenuates the low frequency components without disturbing high-frequency components.

Ideal Filter

The transfer function which satisfies the following relation is called a two-dimensional ideal highpass filter (IHPF);

$$H(u,v)=\begin{cases}0 & \text{if } D(u,v)\leqslant Do\\ 1 & \text{if } D(u,v)>Do\end{cases} \qquad (10)$$

where Do is the cut-off distance measured from the origin of the frequency plane, and $D(u,v)=(u^2+v^2)^{1/2}$.

Figure 9 shows the sharpening in the image achieved by applying IHPF with $Do=\sqrt{10}$. The edges of the prisms are predominant only in this image because the low frequency components were severely attenuated.

CONCLUSION

The 2-D Hilbert transform can be considered as one of the most important trasforms in image processing for image enhancement.

The first and second vertical derivatives of the gravity field caused by multiprismatic bodies can be obtained by 2-D Hilbert transform technique. Such techniques are used to locate the vertical projection of the subsurface bodies.

The image sharpening of the second vertical derivative obtained either by differentiation or highpass filtering, can be used as an additional tool to locate the boundary of the subsurface bodies.

The results indicate that the discussed techniques are quite useful in isolating the anomalies in 3-D potential field data.

ACKNOWLEDGEMENT

The author would like to acknowledge the support and encouragement of the Petroleum Research Centre received during the preparation of this work.

REFERENCES

Bose, N.K. and Prabhu, K.A., 1979, Two-Dimensional Discrete Hilbert Transform and Computational Complexity Aspects in its Implementation, IEEE Transactions on Acoustics, Speech and Signal processing, Vol. Assp-27, No. 4.

Curts, F.G., 1980, Applied Numerical Analysis, Addison-Wesley Publishing Co.

Gonzales, R.C. and Wintz, P., 1977, Digital Image Processing, p. 154–162, 183–211.

Goodacre, A.K., 1973, Some Comments on the Calculation of the Gravitational and Magnetic Attraction of a Homogenous Rectangular Prism, Geophysical Prospecting, Vol. 21, p. 66–68.

Hall, E.L., 1979, Computer Image Processing and Recognition, p. 239–242.

Nabighian, M.N., 1984, Toward a Three-Dimensional Automatic Interpretation of Potential Field Data Via Generalized Hilbert Transforms: Fundamental Relations, Geophysics, Vol. 49, No. 6, p. 780–786.

Nagy, D., 1966, The Gravitational Attraction of a Right Rectangular Prism, Geophysics, Vol. 21, p. 362–371.

Read, R.R. and Trietel, S., 1973, The Stabilization of Two-Dimensional Recursive Filters Via the Discrete Hilbert Transform, IEEE Transactions on Geoscience Electronics, GE-11, p. 153–160.

Wooil, M.M., Ushah, A., Singh, V., and Bruce, B., 1988, Application of 2-D Hilbert Transform in Geophysical Imaging with Potential Field Data. IEEE Transaction on Geoscience and Remote Sensing, Vol. 26, No. 5, p. 502–510.

PRJ, Vol. 6 (January 1994); P. 52–66, 13 FIGS.

SEISMIC CONFIRMATION OF A NEW TECTONIC ELEMENT SOUTH-CENTRAL SIRT BASIN, LIBYA

M.M. Elazezi* and R.N. Sinha*

دراسة سيزمية تؤكد وجودعنصر تركيبي (تكتوني) جديد بمنطقة جنوب – وسط حوض سرت

محمد مسعود العزيزي و ر. ن. سنها

بينت دراسات جيولوجية سابقة وجود مرتفع (نتق) ذو اتجاه شمال غرب – جنوب شرق، يربط الحد الجنوبي لحوض سرت مع مسطح البيضاء ويفصل منخفض الحقفة عن منخفض دور العبيد وأبوتميم.

إعتمدت النتائج الجيولوجية بصورة رئيسية على المعلومات المحتصل عليها من الآبار الموجودة بالمنطقة مما حتم ضرورة التحقق ودعم هذه النتائج بأدلة جيوفيزيائية لتأكيد وجود هذا المرتفع من عدمه.

لقد تم استخدام معلومات لعدد سبع خطوط سيزمية تغطي حوالي «200» كيلومتر بالإضافة إلى معلومات لآبار واقعة على امتداد هذه الخطوط.

نتائج الدراسة السيزمية أعطت أدلة واضحة عن وجود هذا المرتفع والمحاط بفوالق ذات إتجاه شمال غرب – جنوب شرق، ويمكن إعتبار هذا المرتفع منطقة استكشافية واعدة بتجمعات نفطية.

ABSTRACT

Subsurface geologic studies brought to light an unrecognised and unreported prominent horst which is herein named "Inferred Horst". This horst trends NW–SE, links the Southern shelf with the Beda Platform and separates the Hagfa Trough from the Dor Alabid and Bu Tumayam Trough. This geologic finding relys mainly on data available from wells drilled in the area. Therefore, it is very essential to be verified and supported by geophysical evidences to confirm the presence or otherwise of this horst.

Seismic data along seven selected profiles covering nearly 200 line kilometers, were studied alongwith the completion, sonic and gamma ray logs of few wells. The study gave clear indications of the presence of MW–SE striking inferred faults bordering the Inferred Horst. It appears to be a composite tectonic unit formed by minor positive and negative blocks. The Inferred Horst is concluded to be prospective and seems to offer good locales for large accumulations of hydrocarbons.

* Petroleum Research Centre, P.O. Box 6431, Tripoli, G.S.P.L.A.J.

INTRODUCTION

The tectonic elements in the south-central Sirt basin include the Beda Platform, Hagfa Trough, Zelten Platform, Dor Alabid Trough, Bu Tumayam Trough and the Southern Shelf (N.O.C., 1983; subsequently revised in 1989 and 1990). These tectonic elements are delimited by major normal faults. The Bu Tumayan Trough is shown to join the Hagfa Trough towards the north and thus separates the Beda Platform from the Southern Shelf.

On the basis of geologic analysis, Sinha (1990) inferred the presence of a new tectonic element (*Inferred horst*) located between the Beda Platform and the Southern Shelf. Subsequently, a detailed study of subsurface data available from nearly 150 wells was carried out and, with the aid of structural, isopach and lithofacies maps for various stratigraphic units and several cross-sections, the presence of this horst (Fig. 1) was established (Sinha, 1992). According to this study, the horst links the Beda Platform with the Southern Shelf, trends NW–SE and separates the Bu Tumayam Trough from the Hagfa

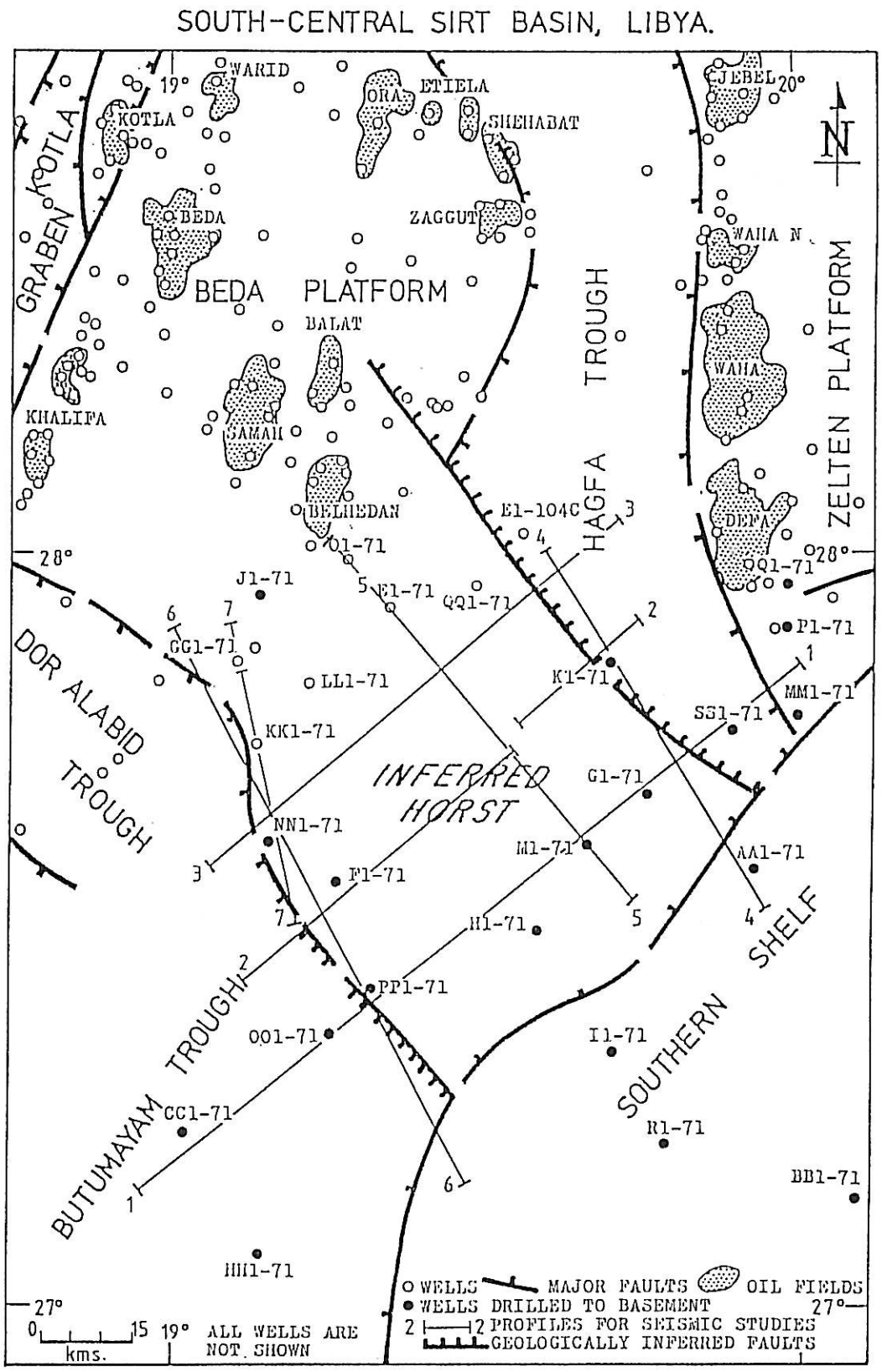


FIG. 1. Tectonic map (After Sinha, 1992).

Trough. It also was concluded that this horst has been intermittently active at least since the Campanian and hence is important from the view point of hydrocarbon prospects.

It was felt that the obtained geologic evidences regarding the newly discovered horst are not enough. These evidences require strong support by geophysical data. The use of seismic profiles across the study

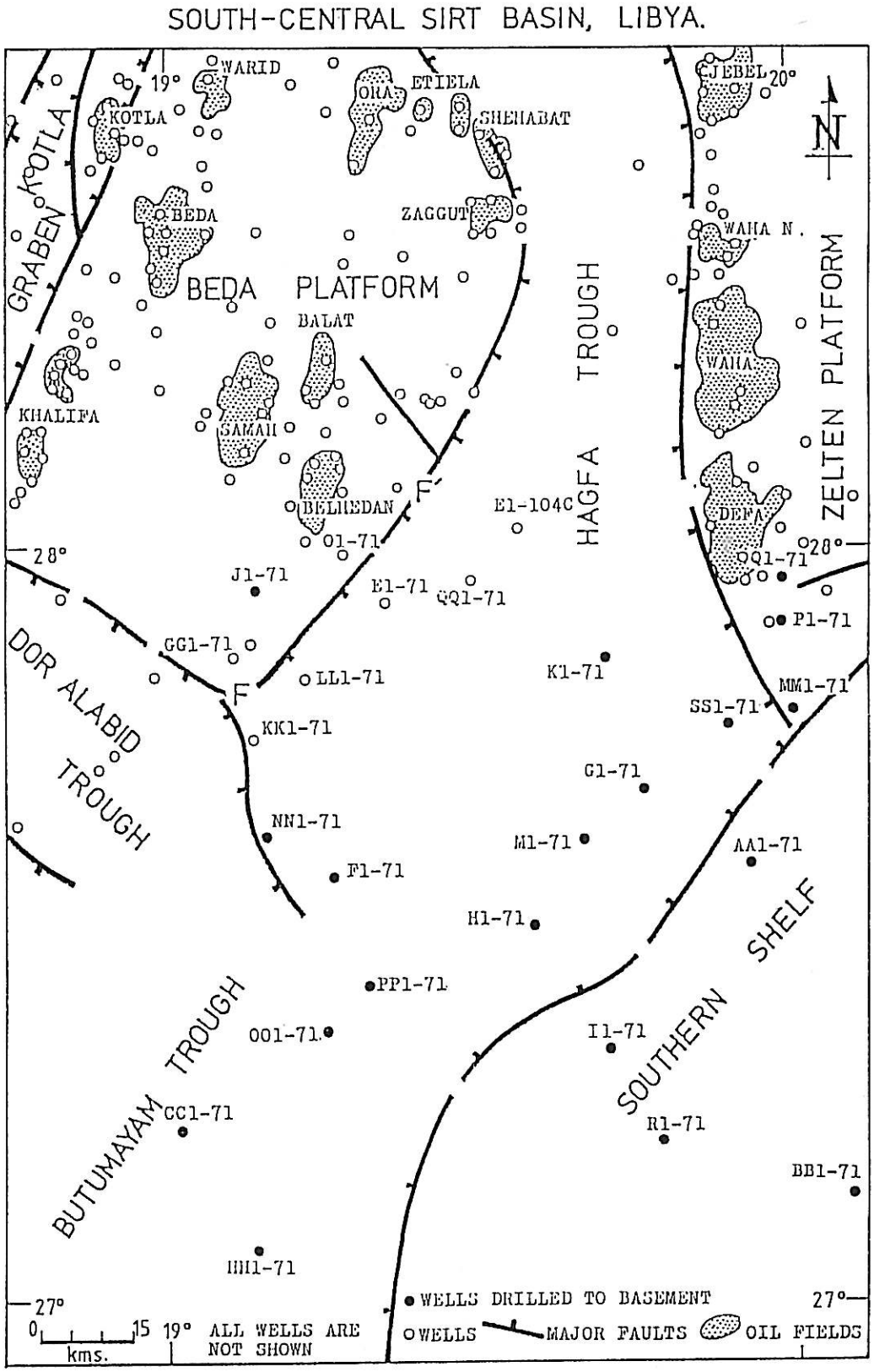


FIG. 2. Tectonic map (After National Oil Corporation, 1983).

area is very essential in order to resolve the arguments about the presence of the Inferred Horst.

A preliminary appraisal of seismic data along seven selected profiles (Fig. 1) across the *Inferred horst* was carried out mainly to confirm the presence or otherwise of this horst established by geologic studies. Profiles 1 to 3 are oriented almost NE–SW whereas, 4 to 6 are aligned approximately NW–SE. Profile 7

runs NNW–SSE. All these profiles cover the Inferred Horst and extend over parts of the adjoining tectonic elements.

WELL DATA

Completion logs of twenty five wells (AA1, BB1, CC1, E1, F1, G1, GG1, H1, HH1, I1, J1, K1, LL1, M1, MM1, NN1, O1, OO1, P1, PP1, Q1, QQ1, R1, SS1-71 and E1-104 C) were studied (Fig. 2). Nineteen of these are drilled through the entire sedimentary sequence and were bottomed in the igneous-metamorphic basement (Fig. 1). Gamma ray logs were available for only ten wells (AA1, F1, G1, GG1, H1, I1, J1, K1, OO1 and PP1-71) and these assisted in the delineation of various lithologic units. Only ten sonic logs (AA1, E1, F1, G1, GG1, I1, J1, K1, OO1, and PP1-71) could be procured and these were used for interval velocity assessments.

SEISMIC DATA

The seven profiles covering the *Inferred horst* comprise sixteen seismic lines (nos. 677, 713, 804, 805, 826, 842, 959, 970, 972, 1001, 1012, 1136, 1157, 1168, 1181 and 1189) shot by the Waha Oil Company, Libya, during 1971-1990. These, totalling approximately 200 line kms, were studied in detail. The data range from poor to good due to variations in fold coverage as well as recording and processing parameters. They however, adequately reflect the various tectonic elements of the study area. These elements are defined by normal faults. Some portions of few seismic lines need to be reprocessed for better resolution.

DESCRIPTION OF RESULTS

Profile 1

This profile is aligned NE–SW and covers the southern part of the area. It consists of 6 seismic lines 804, 842, 805, 972, 677, and 1181. Line 804 (SP's 1–240) is 24 fold stack, shot in 1975 and cover the Bu Tumayam Trough. The section shows gradual updip towards the NE. The dipping is around 100 ms in the upper part such as at 700 ms TWT and increases in the lower part of the section into around 300 ms (2000–1700 ms TWT) towards the NE.

Line 842 is an extension of line 804 shot in 1976. It consists of CMP 1–272 with wells OO1-71 and PP1-71 located along the line at CMP 66 and 152 respectively. The section shows main reflection interfaces which are characterized by their continuity and strength. These reflectors are mainly between 600 and 1700 ms TWT and could be divided into upper and lower part. The upper reflectors (600–1000 ms TWT) gradually dip towards the northeast. The lower part shows very important structural features consisting of normal faults. The reflection interfaces between CMP 1–54 and at 1700 ms TWT are nearly flat. These events are shifted upward around 75 ms TWT between CMP 54–77 and then shifted down again with slight dipping upward until CMP 126. The interval between CMP 126 and 142 shows scattered seismic energy and strong indication of the presence of a fault (Fig. 3) with a displacement of about 200 ms TWT. This fault separates the *Inferred horst* from Bu Tumayam Trough.

Line 805 is a continuation of line 842 and consists of stations 1–316. Well M1-71 is located along the line at CMP 33. The reflectors between CMP 204 and 316 are characterized by gentle dipping of about 30 ms TWT in NE direction. The interfaces in the lower part of the section between 1200 and 1500 ms TWT and CMP 204 are shifted upward by about 100 ms TWT. This displacement is a clear indication of the presence of a normal fault. This fault is located well within the area covered by the *Inferred horst*. The reflectors between CMP 1 and 204 are nearly flat. The deeper events are characterized by strong amplitude and continuity, specially those between 1200 and 1300 ms TWT.

Line 972 shot in 1978, consists of CMP 1–196. Wells M1 and G1-71 are located at CMP 40 and 156 respectively. The reflection interfaces between 400 and 1300 ms TWT and CMP 1 and 162 are generally flat with high amplitude and continuity. They dip downwards due NE in the interval between CMP 156 and 196. The dipping is very evident in the lower part of the section between 1000 and 1700 ms TWT. It shows clear indications of the presence of several major faults (Fig. 4), especially through tracing of main reflectors in the interval between 1200 ms TWT along the section. These faults separate the *Inferred horst* from the Hagfa Trough.

The last part of profile 1 is covered by the seismic line 1181. It consists of CMP 1–615. It is shot in 1989 across the Hagfa Trough and wells G1 and SS1-71 are located at CMP 548 and 224 respectively. The section is characterized by scattering and burst of seismic energy at some interval especially in the lower part of the section such as at intervals between CMP 504–550, 450–464, 312–348 and 168–240. The reflective interfaces in the upper part of the section show strong amplitude and continuity, and a general dip due NE. The lower part shows indications of faults. These faults are evident between CMP 504–516 and 450–462 and display a throw of about 100 ms TWT. Also, there are two other faults between CMP 316–342 and 168–212 with updip shift of about 300 ms TWT and 100 ms TWT respectively. The large interval of disturbance could be a result of stacking velocity picking in faulted and fractured zone with

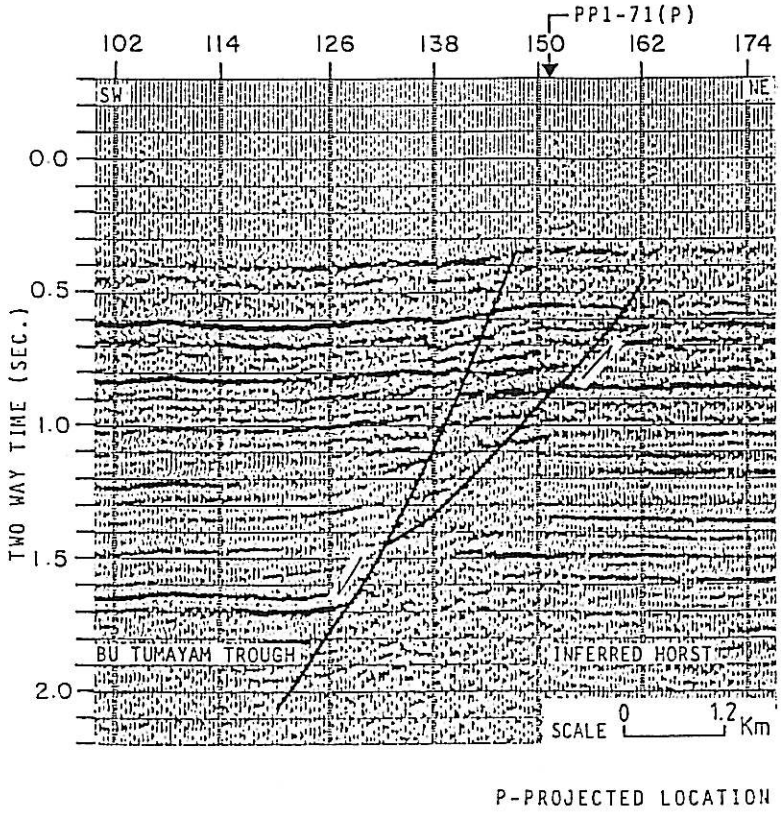


FIG. 3. Part of line 842; Profile 1-1.

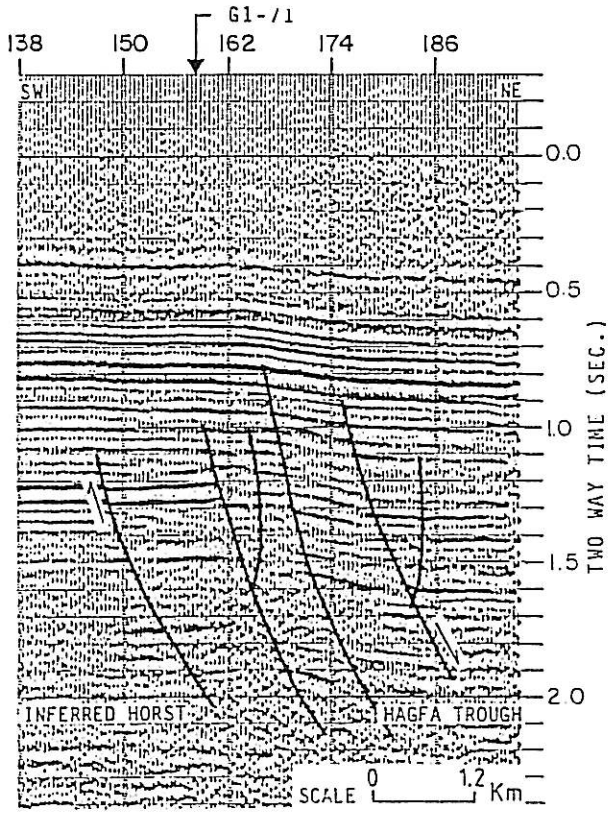


FIG. 4. Part of line 972; Profile 1-1.

low velocity which produce moving up of the reflection events that affected even the upper part of the reflection interfaces. The section shows presence of a fault dipping downward NE of well G1-71 and also another fault with an upthrown block NE of well SS1-71. These faults define the boundaries between *Inferred horst*, Hagfa Trough and Zelten Platform, (Fig. 1), respectively.

Profile 2

The profile 2, aligned NE–SW, crosses the middle part of the area and is represented by seismic lines 692 and 1001. It extends to the southern part of Hagfa and Bu Tumayam troughs. Seismic line 692 shot in 1972 represents the southwestern part of profile 2. The projected location of well F1-71 is close to CMP 176. The reflectors in the interval between CMP 1–102 show steep dips towards the SW and also indicate major step faults (Fig. 5) with a cummulative throw of about 200 ms TWT between CMP 66–102. These faults are discernible between 1500–2000 ms TWT and separate the *Inferred horst* from the Bu Tumayam Trough. The reflection interfaces in the interval between CMPs 102–238 are nearly flat with very gentle southwesterly dip. The reflectors from CMP 220 to the end of the section slightly dip towards the NE and also show evidences of step faulting (Fig. 6) in the interval between CMP 220–286 and with throw of around 100 ms TWT. The interfaces thereafter become nearly flat. These faults are located well within the area covered by the *Inferred horst*.

Seismic line 1001 was shot in 1979. It consists of 284 CMP and represents the northeastern part of profile 2. Well K1-71 is located very close to CMP 215. The reflection interfaces are characterized by strong amplitude and persistent continuity along the section with gentle dip towards the NE. The interval between CMPs 222–234 is denoted by presence of major faults (Fig. 7) with a throw of around 200 ms TWT towards the NE. These separate the *Inferred horst* from the Hagfa Trough. The two major faults in seismic sections 692 (Fig. 5) and 1001 (Fig. 7) clearly confirm presence of the *Inferred horst*.

Profile 3

Profile 3, represented by seismic lines 959 and 959 ext., is in the same direction as the profiles 1 and 2. Shot in 1977, it consists of CMP 1–704. It crosses the *Inferred horst* and extents into the Hagfa and Bu Tamayam troughs to the NE and SW respectively. Well NN1-71 is located at CMP 606. The main reflection interfaces in seismic section 959 cover interval between 300 and 1950 ms TWT. Most of the interfaces are characterized by high amplitude and continuity along the section. The interval between CMP 704 and 606 shows gradual updip of about 200 ms TWT toward the NE. There are indications of

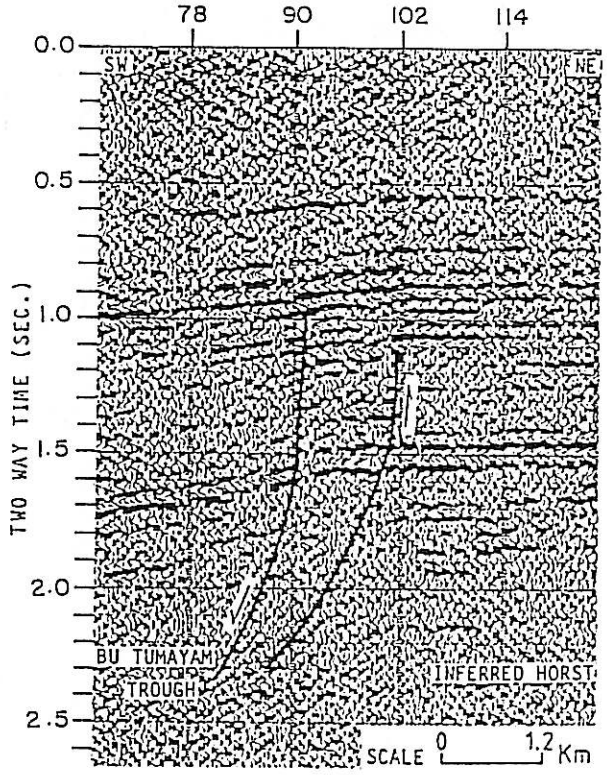


FIG. 5. Part of line 692; Profile 2-2.

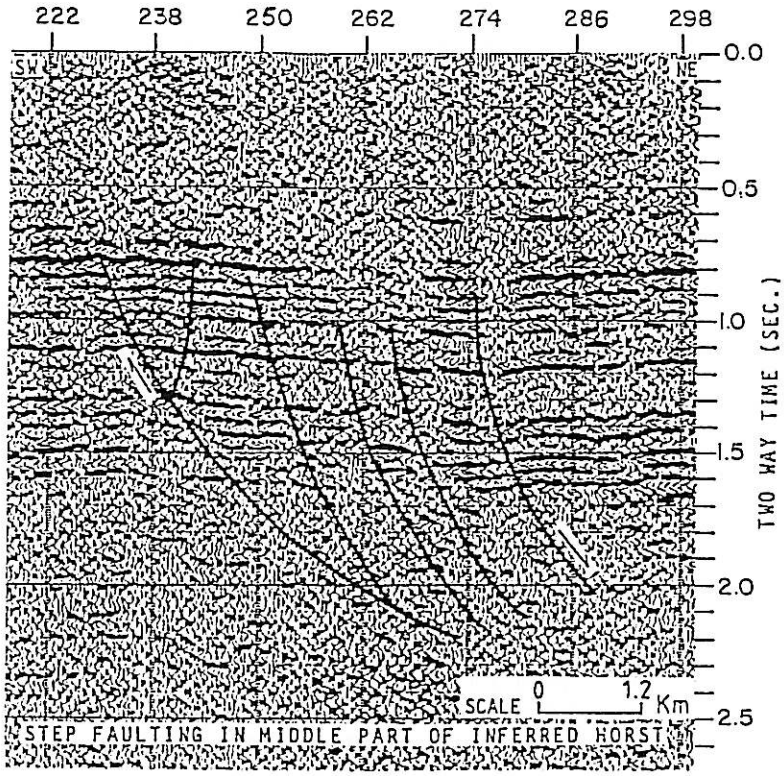


FIG. 6. Part of line 692; Profile 2-2.

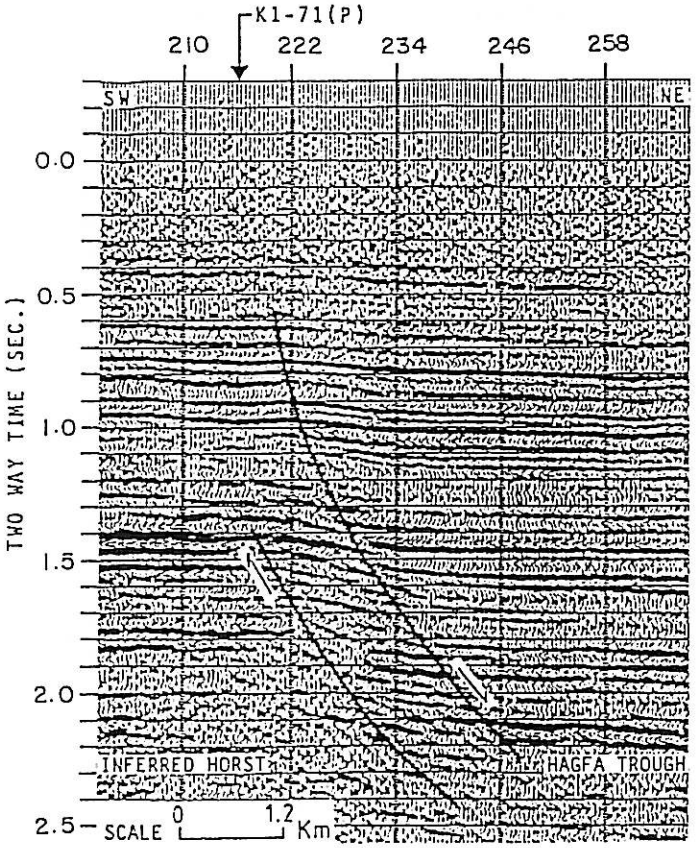


FIG. 7. Part of line 1001; Profile 2-2.

presence of normal fault (Fig. 8) around CMP 610 in the lower part of the section. The throw of the fault is not clear and the data might require reprocessing for better resolution. These faults separate the *Inferred horst* from Bu Tumayam Trough. The reflectors in the rest of the section are nearly flat.

The other part of profile 3 is covered by seismic line 959 ext. consisting of 113 CMPs (705–818). It is a continuation of line 959 with reflection interfaces dipping towards the NE. The main feature of the section is the presence of a major normal fault (Fig. 9) in the interval between CMP 756–780. The fault is clearly shown in the lower part of the section between 1500 and 2300 ms TWT with noticeable effect on the reflectors in the upper part of the section. This could be associated with a number of step faults with a cummulative throw of about 400 ms TWT. These faults separate the *Inferred horst* from the Hagfa Trough.

Profile 4

This profile, aligned NW–SE, extends from the Southern Shelf in the southeast to a part of the Hagfa Trough and thereafter covers a part of the *Inferred horst* as well as a smaller part of the Hagfa Trough further northwest (Fig. 1). It is represented by seismic lines 1189 and 1012. Seismic line 1189, shot in 1990, consists of CMP 1–455. The reflection interfaces show good continuity and high amplitude. These reflecting horizons dip gently due NW and indicate presence of a fault around CMP 60 that separates the Southern Shelf from the Hagfa Trough. The lower part of the section shows a sudden increase in dip between CMP 370–455.

Seismic line 1012, shot in 1979, consists of CMP 1–302. The reflectors in the upper part of the section (between 400 and 1300 ms TWT) are almost horizontal and exhibit high amplitude and continuity. The lower part is characterized by a northwesterly dip, high amplitude and reasonably good continuity. Multiples are present. The trace of the *Inferred horst* bounded by the normal faults can be deciphered between CMP 174 and 78.

Profile 5

This profile, aligned NW–SE, crosses nearly the middle part of the area. It comprises seismic lines 1136, 1168, and 970. The first part is represented by

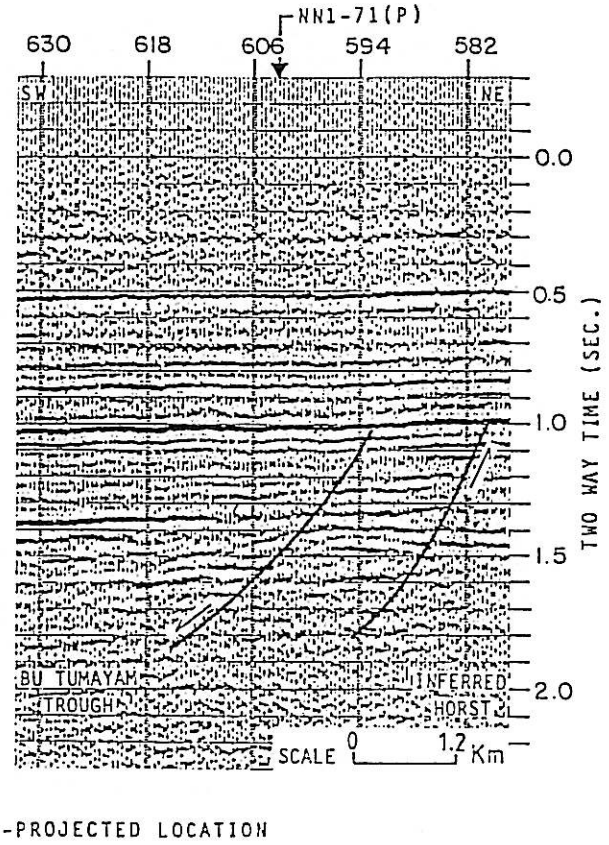


FIG. 8. Part of line 959; Profile 3-3.

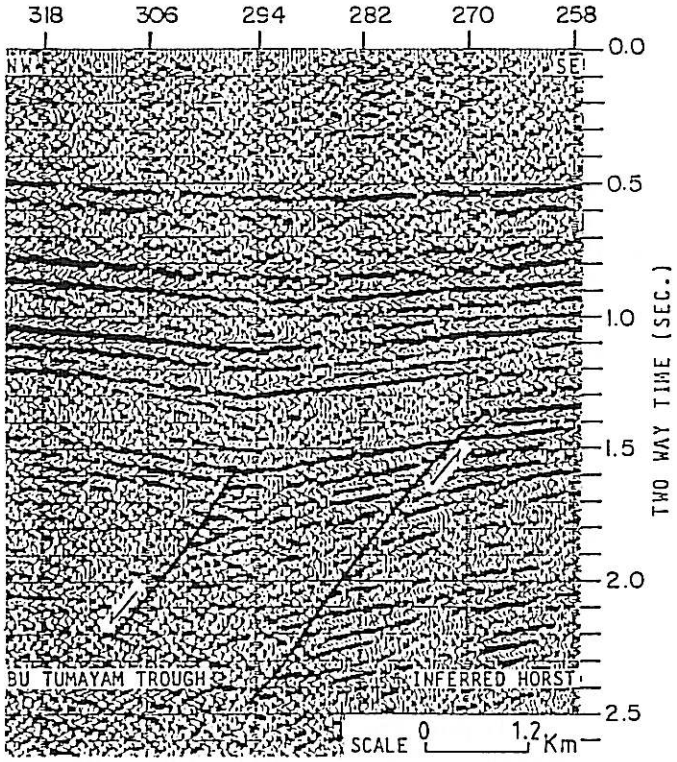


FIG. 9. Part of line 959 EXT; Profile 3-3.

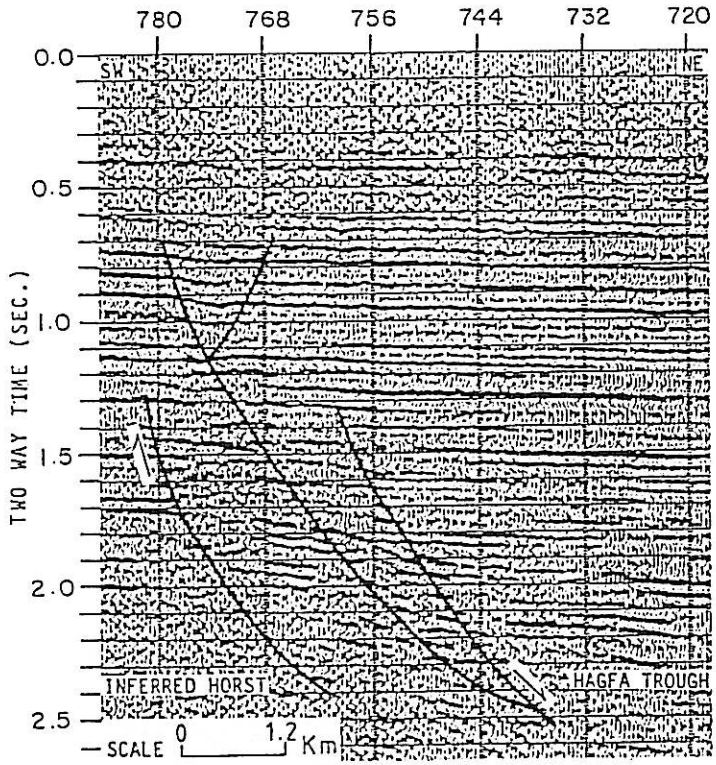


FIG. 10. Part of line 713; Profile 6-6.

seismic line 1136 shot in 1988 and consists of CMP 1–364. Wells O1 and E1-71 are located at CMP 312 and 122. The main reflection interfaces are characterized by high amplitude and continuity especially in the upper part of the section and are denoted by gentle dips towards the SE. There are no indications for the presence of any fault in the interval between CMP 120 and 360, that is between wells O1-71 and E1-71 (Fig. 11) although the tectonic maps of N.O.C. (1983; revised in 1989 and 1990) show its presence (F–F'; Fig. 2).

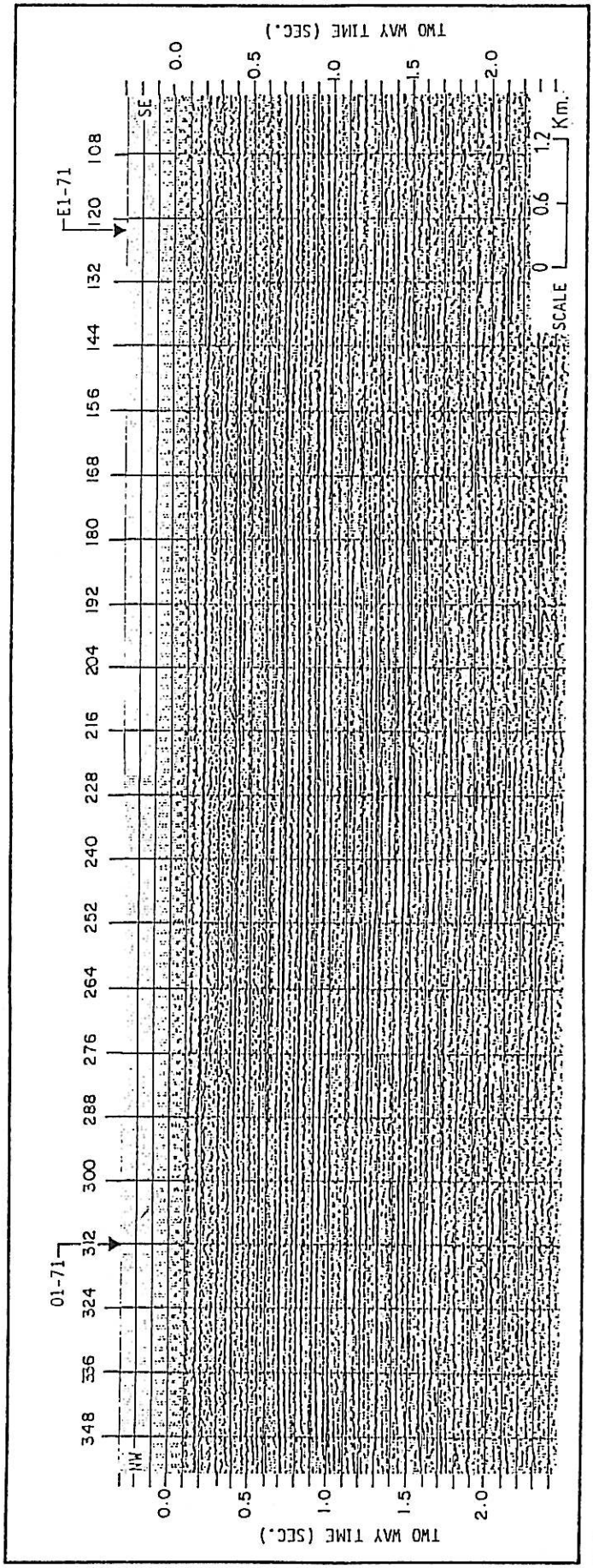


FIG. 11. Part of line 1136; Profile 5-5.

Seismic line 1168 represents the middle part of profile 5. It was shot in 1989 and consists of CMP 1–415. The reflection horizons are characterized by gentle dips towards the NW, high amplitude and continuity.

Seismic line 970, shot in 1978, consists of CMP 1–180. It is a continuation of line 1168 with well M1-71 located at CMP 103. The main reflectors, which very gently slope towards the NW in the lower part of the section, are, characterized by strong amplitude and continuity.

Profile 6

Profile 6 runs across the area in NW–SE direction and extends into the Southern Shelf and Beda Platform, (Fig. 1). It consists of seismic lines 713 and 826. These two lines are nearly in the same direction as that of the fault except in the NW part where they cross the fault. As shown in seismic section 713, the section between CMP 186 and 318 is characterized by reflectors with high amplitude and continuity especially in the upper part of the section. The lower part (between 1000–1800 ms) of this section is marked by faults (Fig. 10) as is brought out by the displacement of various reflectors. These faults seem to separate the *Inferred horst* from the Bu Tumayam Trough.

Line 826 consists of 420 CMPs 1–420 with well PP1-71 located at CMP 73. It is a continuation of seismic line 713. The reflection horizons show the same characters especially in the interval between CMPs 1–126. These reflectors then gradually dip towards the NE, between CMP 126–306. This interval represents the change from the *Inferred horst* to the Southern Shelf with possible presence of a fault at CMP 306. Another fault is indicated near CMP 246. The section between 126–234 CMP is very fuzzy and may need reprocessing. The rest of the section extends over the Southern Shelf.

Profile 7

Profile 7 consists of seismic lines 1157 (CMP 1–460) and 796 (CMP 1–400) shot in 1988 and 1974 respectively. Seismic line 1157 extends from the *Inferred horst* to Beda Platform. These lines were studied to ascertain if the southeastern part of Beda Platform is demarcated/delimited by any fault as is shown by the tectonic map of N.O.C., 1983; revised 1989 and 1990, FF'; Fig. 2. Wells GG1 and KK1-71 are located along the line at CMP 430 and 180 respectively. The main reflection interfaces are characterized by strong amplitude and continuity. The reflections between CMP 276–460 show gradual downdip towards the SSE especially in the lower part of the section. The interval between CMP 156–444 of line 1157 is characterized by nearly flat and undisturbed reflectors (Fig. 12). This seismic section does not confirm the presence of any fault which according to the tectonic maps of N.O.C. (1983; revised in 1989 and 1990) occurs between wells GG1 and KK1-71 and defines the southeastern margin of the Beda Platform (F–F'; Fig. 2).

Seismic line 796 covers the south-southeastern part of line 7 with wells KK1 and NN1-71 located at CMPs 32 and 344. The main reflection interfaces show high amplitude and continuity. These reflectors are almost flat along the entire seismic section.

DISCUSSION

The tectonic maps for the south-central part of the Sirt Basin (N.O.C., 1983; revised in 1989 and 1990) show that:

(a) the Bu Tumayam Trough continues to the north and joins the Hagfa Trough (Fig. 2),
(b) the Beda Platform is separated from the Southern Shelf by the northern parts of Bu Tumayam Trough and southern part of Hagfa Trough (Fig. 2) and,
(c) the southeastern margins of the Beda Platform is defined by a NE–SW trending normal fault (F–F'; Fig. 2).

Contrary to the above, Sinha (1990 and 1992) on the basis of geologic studies established that:

(a) the Bu Tumayam Trough is separated from the Hagfa Trough by a horst (*Inferred horst*; Fig. 1),
(b) the Beda Platform is tectonically linked to the Southern Shelf through the *Inferred horst* (Fig. 1) and,
(c) the southeastern margins of the Beda Platform are not defined by any fault (Fig. 1).

Seismic data along seven profiles across the *Inferred horst* and marginal parts of adjoining tectonic elements (Fig. 1) was critically studied to verify the foregoing conclusions of Sinha (1990 and 1992).

Study of data along the various seismic lines comprising each of the seven profiles, as already given in the foregoing establishes presence of major normal faults. These are located towards the southwestern part of profiles 1, 2 and 3 (Figs. 3, 5 and 8). Each of these faults is marked by a southwesterly down thrown block which seems to form the Bu Tumayam Trough. The traces of these faults on profiles 1, 2 and 3 when joined together seem to form a NW–SE trending system of regionally developed normal faults. These appear to extend further NNW and thereafter to NW to join the major fault (NW–SE) already mapped by N.O.C., 1983, and which defines the southwestern margins of Beda Platform. The northwestern blocks of

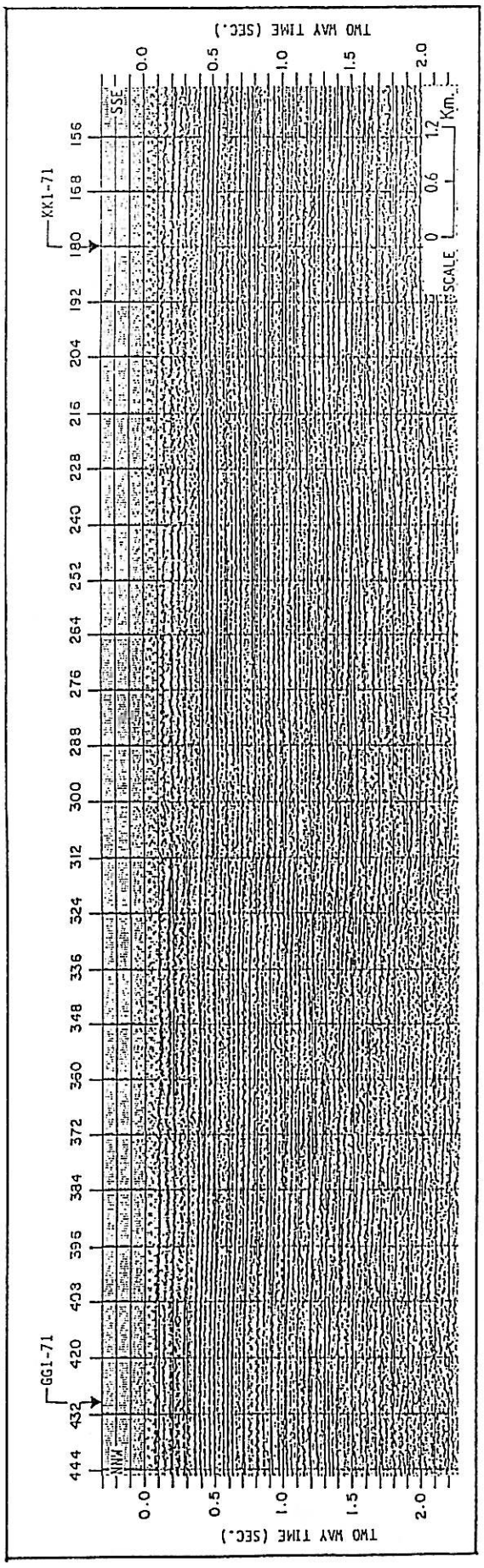


FIG. 12. Part of line 1157; Profile 7-7.

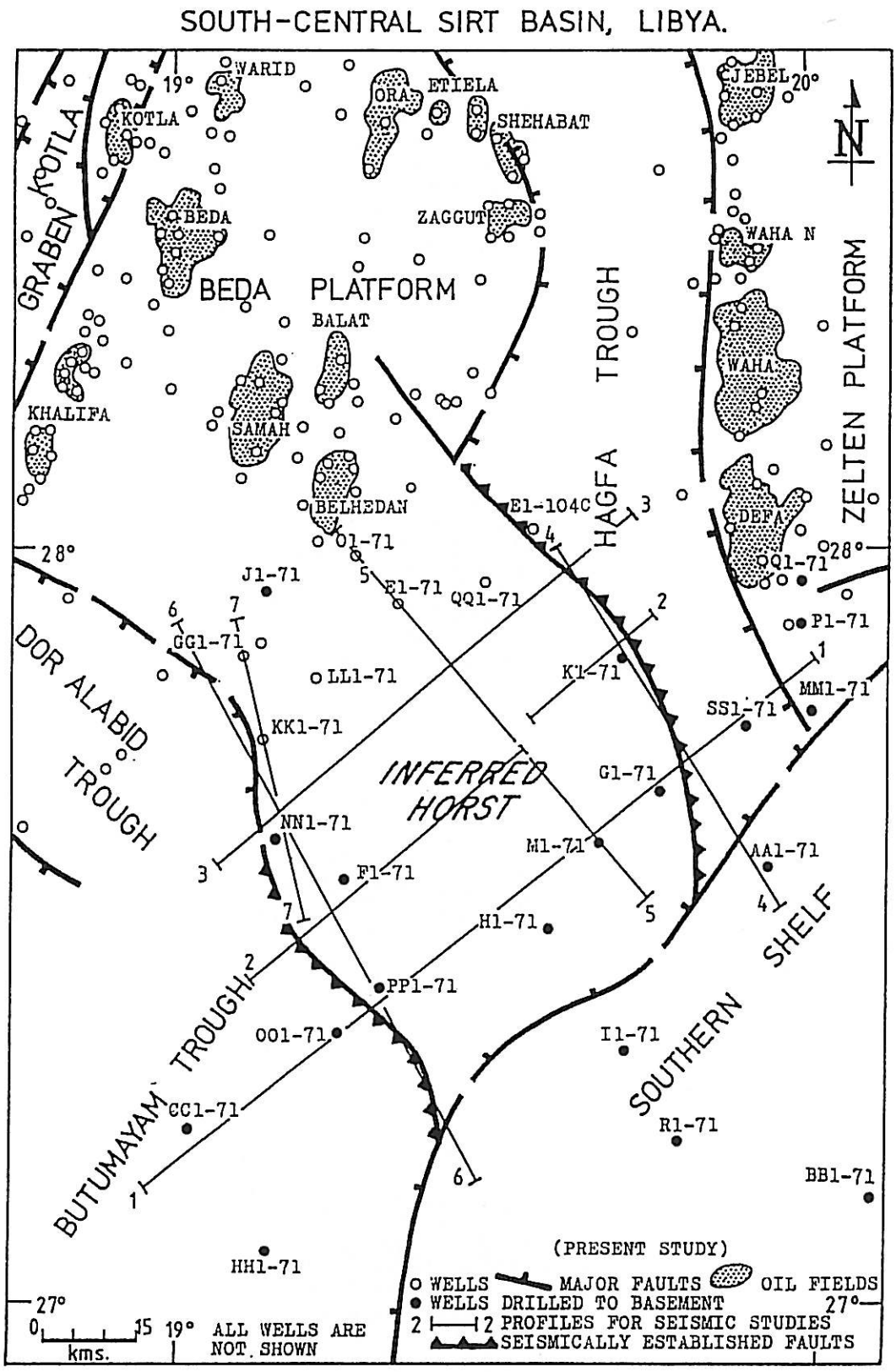


FIG. 13. Tectonic map on basis of the new seismic and geologic evidences (present study).

these faults are upthrown and together they form the *Inferred horst* (Fig. 13).

Seismic data from the northeastern parts of profiles 1, 2 and 3 display major normal faults (Figs. 4, 7 and 9). Each of these faults are marked by a northeasterly down thrown block and a southwesterly upthrown block. These faults when traced from profile 1 to 3, seem to form an almost NW–SE trending regional

fault system extending up to the Southern Shelf in the southeast and over the Beda Platform towards the northwest. The down thrown block corresponds to the Hagfa Trough while the upthrown block forms the *Inferred horst* (Fig. 13). Profile 4, aligned NW–SE is almost parallel to this fault. A normal fault with a northwesterly down thrown block is detected at CMP 60 of line 1189 which represents the southeastern part of profile 4. This fault seems to mark the margin of the Southern Shelf.

Seismic data from the northwestern parts of profiles 5 and 6 was studied in conjuction with data from KK1, NN1, O1 and El-71 wells (Fig. 1) with special attention to detect the presence or otherwise of the F–F′ part of the fault shown (N.O.C., 1983; revised in 1989 and 1990) to demarcate the southeastern margins of the Beda Platform (Fig. 2). The main reflectors along the seismic lines extending from wells 01 to El-71 (Fig. 11) and GG1 to KK1-71 (Fig. 12) are denoted by high amplitude and good continuity and marked by conspicuous absence of any signs of faulting. The presence of F-F′ part of the fault, hence, is not supported by seismic data even though it is shown by the tectonic maps of N.O.C. (1983; revised 1989 and 1990).

The forementioned study of seismic data appear to overwhelmingly confirm all the geologic conclusions of Sinha (1992). They confirm the presence of regionally developed *Inferred horst* in an area otherwise regarded to represent parts of two very major troughs (Bu Tamayam and Hagfa) of the Sirt Basin. The extension of Beda Platform due southeast and its linkage with the Southern Shelf through the *Inferred horst* does not seem questionable. The tectonic map prepared on the basis of seismic and geologic studies (Fig. 13), though very similar to that prepared earlier on basis of geologic evaluation (Fig. 1), brings out a better and more meaningful resolution of the faults and consequently, of the *Inferred horst*.

Normal faults with smaller throws (under 100 ms TWT) are present even within the area covered by the *Inferred horst*. These are detected on profile 1 at CMP 204 and on profile 2 between CMP 220–286 (Fig. 6). Those observed on profile 1 seem to hade due southwest while those traceable on profile 2 may hade towards the northeast. The *Inferred horst*, hence, seems to be a composite tectonic unit comprising several minor negative and positive blocks. At the present stage of study, it does not seem feasible to attempt the mapping of these faults. They, however seem to trend NW–SE. Seismic data from additional lines need to be evaluated for their precise delineation and detailing.

HYDROCARBON PROSPECTS

Oil fields are yet to be discovered in the area covered by the *Inferred horst*. Presence of oil is noted in sandstones (Late Cretaceous) met at G1-71 and in Lower Beda Formation (Palaeocene) met at NN1-71. Several giant oil accumulations are noted over the adjoining Beda Platform. Likewise, prolific oil fields are located over the nearby Zelten Platform (Fig. 13).

Sirt Shale of Campanian age is one of the principal source rocks of liquid hydrocarbons in the Sirt Basin (Hamayouni *et al.*, 1984). It is nearly 200 feet thick over the horst but it rapidly thickens to more than 1000 feet towards the northeast and southwest in the adjoining Hagfa and Bu Tumayam troughs respectively. It contains nearly 2.0 percent (average) of Type II and II–III Organic matter (Robertson International Corporation, 1979). Good clastic and carbonate reservoir rocks overlain by regionally developed shale cap rocks are present in the Early Cretaceous-Palaeocene sequence. The *Inferred horst* is concluded to have been intermittantly active since Campanian and was structurally positive during Oligocene-Miocene (Sinha, 1992) when the oil was generated, expelled and migrated from the Sirt Shale (Hamoyouni *et al.*, 1984 and El Alami *et al.*, 1989) to form giant accumulations over the adjoining Beda Platform and the nearby Zelten Platform. By the same analogy it must have also migrated over the *Inferred horst* in suitable entrapments. The hydrocarbon proclivity of the *Inferred horst*, thus, does not seem disputable. The *Inferred horst* appears to be a composite tectonic unit comprising minor positive and negative blocks. Their detailing is necessary for a more meaningful and objective evaluation of hydrocarbon prospects. Furthermore, presence of reefs especially within the Palaeocene carbonates enveloping the *Inferred horst* can not be ruled out (Sinha, 1992).

CONCLUSIONS

- The use of seismic data has contributed effectively in providing the approximity to investigate and resolve the arguments regarding the *Inferred horst*.
- Study of seismic sections covering about 200 line kms along seven selected profiles in the south-central Sirt Basin confirm the presence of the horst (*Inferred horst*) as already concluded by earlier subsurface geologic studies. This new tectonic element occupies the basinal part otherwise considered to represent major troughs.
- The *Inferred horst* links the Beda Platform with the Southern Shelf, strikes NW–SE and isolates the Bu Tumayam Trough from the Hagfa Trough. Seismic data suggest that this horst is a composite tectonic unit comprising minor positive and negative blocks delimited by normal faults of minor

throws. Alignment of the minor blocks could be NW–SE.

- The *Inferred horst* is concluded to be very prospective and seems to offer good locales for large accumulations of hydrocarbons.

ACKNOWLEDGEMENT

The authors are grateful to Mr. M. Idris, Secretary of People's Committee and Mr. Salem A. Sulaiman, Supervisor, Exploration Division, Petroleum Research Centre for help, encouragement and permission for publication and Mr. M. Aburawi, Manager, Exploration, Waha Oil Company, Libya, for releasing seismic sections as well as data and well logs necessary for the study.

REFERENCES

El Alami, M., Rahouma, S., and Butt, A.A., 1989, Hydrocarbon Habitat in the Sirte Basin, Northern Libya, Petrol. Res. Journal, Vol. 1, p. 19–30.

Hamayouni, E.A., Amr. I.A., Riani, A.B., El Ghull, A.B. and Rahouma S.A., 1984, Source and Habitat of Oil in Libyan Basins *in* Proc. Sem. Source. and Habitat of Petroleum in the Arab Countries, Kuwait, p. 127–180.

N.O.C., 1983, (revised 1989 and 1990), Tectonic Elements of Libya, 1:1,000,000, National Oil Corporation of Libya (unpublished).

Robertson Research International, 1979. The Petroleum geochemistry of Oils and Source Rocks in the Southeast Sirte Basin, Vol. I and II, Report to Arabian Gulf Oil Co., Libya (unpublished).

Sinha, R.N., 1990, Palaeocene Palaeogeography and Hydrocarbon Prospects, Sirte Basin, Libya. Rept. National Oil. Corporation, Libya, unpublished.

Sinha, R.N., 1992, The Subsurface Palaeocene Shoal Carbonates, South-central Sirte Basin, Libya, Rept. Petroleum research Centre (unpublished).

PRJ, Vol. 6 (January 1994); p. 67–74, 4 FIGS, 5 PLATES.

REMOTE SENSING AS A TOOL TO STUDY THE GEOLOGY OF THE NORTHEASTERN PART OF TIBESTI MOUNTAIN, LIBYA

K.M. Abdulnasser*

تقنية الإستشعار عن بعد كوسيلة لدراسة جيولوجية الجزء الشمال الشرقي لجبل تيبستي – ليبيا

خليفة عبد الناصر

تم إستخدام نوعان من تقنيات الإستشعار عن بعد في هذه الدراسة وهما الصور الفضائية للقمر الإصطناعي لاندسات تي إم والصور الجوية. الصور الجوية أثبتت أكثر فاعلية في التعرف وتحديد المعالم التركيبية الصغيرة الحجم بينما الصور الفضائية من خلال تطبيق المعالجة الرقمية أثبتت أكثر فاعلية في التميز الليثولوجي للوحدات الصخرية وكذلك لتحديد المعالم التركيبية ذات الأحجام الكبيرة.

الصور الفضائية المحسنة بواسطة الحواسيب الألكترونية أكدت جدواها في التغلب على الصعوبات في تخريط الصخور القليلة التكشف. الوصف البصري للصور الغير مدعوم بالعمل الحقلي تمخضت على إنتاج خريطة جيولوجية مبدئية وخريطة للمعالم الطولية لمنطقة الدراسة.

تم التعرف على ثماني وحدات صخرية والعديد من الظواهر الدائرية والتي تعتبر أماكن قيمة للإستكشاف المعدني.

من خلال هذه الدراسة إتضح أن إستخدام نوعين أو أكثر من تقنيات الإستشعار عن بعد في آن معاً تعتبر الطريقة المثلى في الدراسات الجيولوجية لأنه إلى حد كبير يعتبر كلاهما مكمل للآخر.

ABSTRACT

Two types of remote sensing data are used in this work. These include Landsat TM imagery and aerial photography. Aerial photographs proved to be more useful in locating and determining local structures. Landsat TM imagery, through the application of some image processing techniques, proved more effective for lithologic discrimination of rock units and regional structure of the study area. The computer enhanced images are used to overcome the difficulties of mapping small outcrops where most of the lithological rock units are identified. Interpretation of image processed products, not supported by field checking, are concluded by constructing a preliminary geologic map and lineaments map for Jabal Eghi area. Eight lithological rock units and many circular features are recognized. These circular features should serve as potential areas for mineral exploration. As a result of this study Landsat TM imagery has proved more important than aerial-photography. The use of more than one remote sensing data type such as is employed in this work is the ideal choice of proceeding with such studies because to some extent these two data complement each other.

INTRODUCTION

Geological application has become more interesting through the use of satellite imagery as Landsat MSS, TM and SPOT. Arid areas, devoid of vegetation, are suitable for study by remote sensing techniques. Various image processing techniques are applied to get high quality images suitable for photo-geological interpretation.

The study area is located in the Southern Central part of Libya (Fig. 1). It covers the Northeastern part of the Tibesti Massif and lies between lat. 22°30′ N to 23°00′ North and long. 19°30′ E to 20°00′ E. It is widely known as Jabal Eghi, located near and around Jabal Tushidi.

The aim of this work is to update the geological map of the area by using computer enhanced Landsat TM imagery and aerial photographs. The results are

* Petroleum Research Centre, P.O. Box 6431, Tripoli, G.S.P.L.A.J.

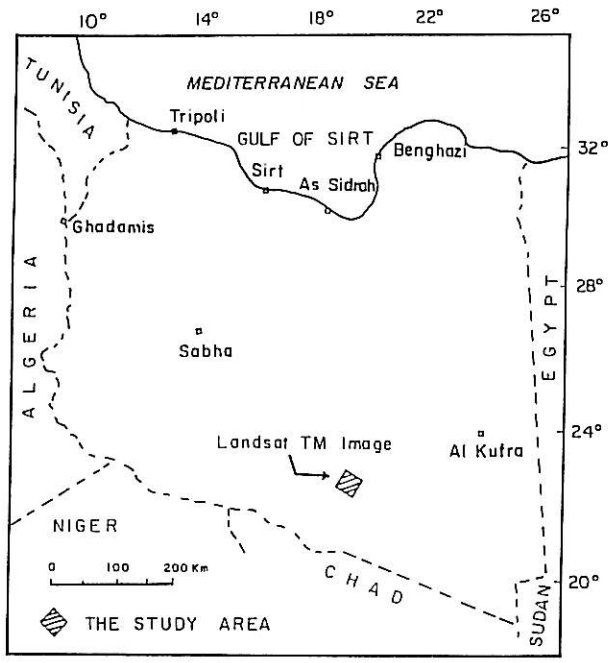


FIG. 1. Map of Libya showing location of the area.

compared with previous studies based, mainly, on aerial photographs.

Image Processing Techniques

Three infrared bands (4, 5 and 7) on CCT were used in this work. Some subscenes (512 × 512) covering the area were generated. By using the R-chips image processing system, different image processing techniques were applied to the images (colour combination, image ratios, principal component analysis and edge enhancement). The output of the subscenes were visually interpreted and incorporated into the final maps. This processing technique is performed simultaneously with the interpretation of aerial photographs of selected areas by using stereoscopic view. Finally the results of two data sets were compared and interpreted.

Aerial-Photographs Interpretation

This interpretation is based on the conventional visual interpretation of B and W aerial photographs by using stereoscopic method. The interpretation, which follows the classic interpretation of geological studies, is divided into two parts: lithological and structural interpretations. Lithologically the different rock units have been identified using standard aerial photographic interpretation techniques, i.e. analysis of textural, tonal, geomorphological and erosional characteristics. Due to the difficulty in determining the age of different rock units by using aerial photographs, the classification by age is mainly determined by correlating the rock units with those of known age in the area based on the geological map of Libya (Conant and Goudarzi 1977) and previous studies (Fig. 2).

Landsat TM Imagery Interpretation

Even though in this work Landsat imagery is divided into three subscenes (Plate 1), the work mainly focused on two subscenes. Area 1 shows all major structural elements and helps in selecting areas for detailed studies. Smaller area is selected by choosing the best region which contains the most geologic work units record according to age. It is labelled as area 2. The study area is visually interpreted and a

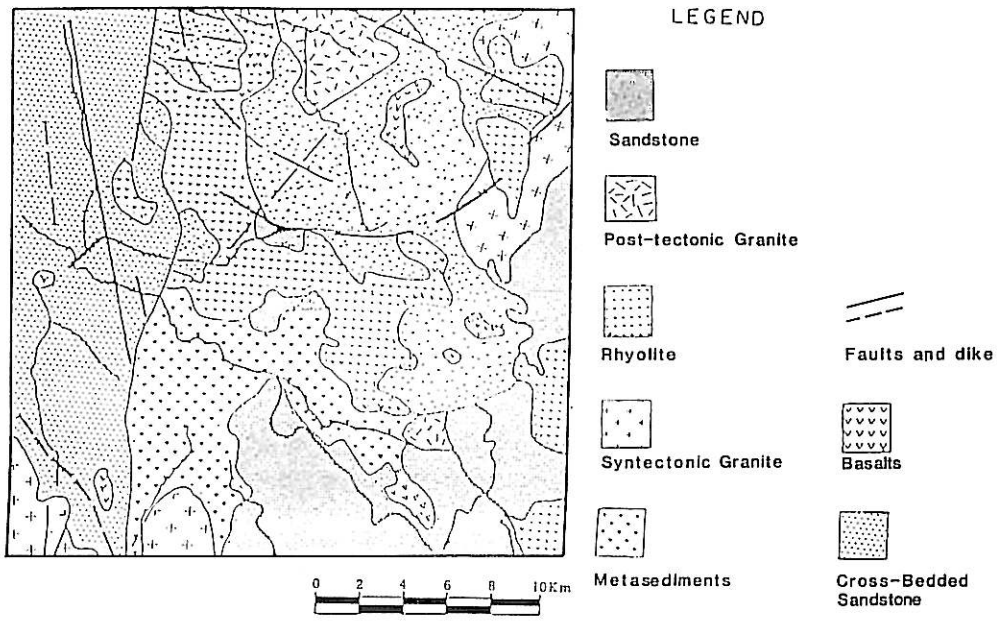


FIG. 2. Geological map of the area (simplified after Missilati *et al.*, 1979).

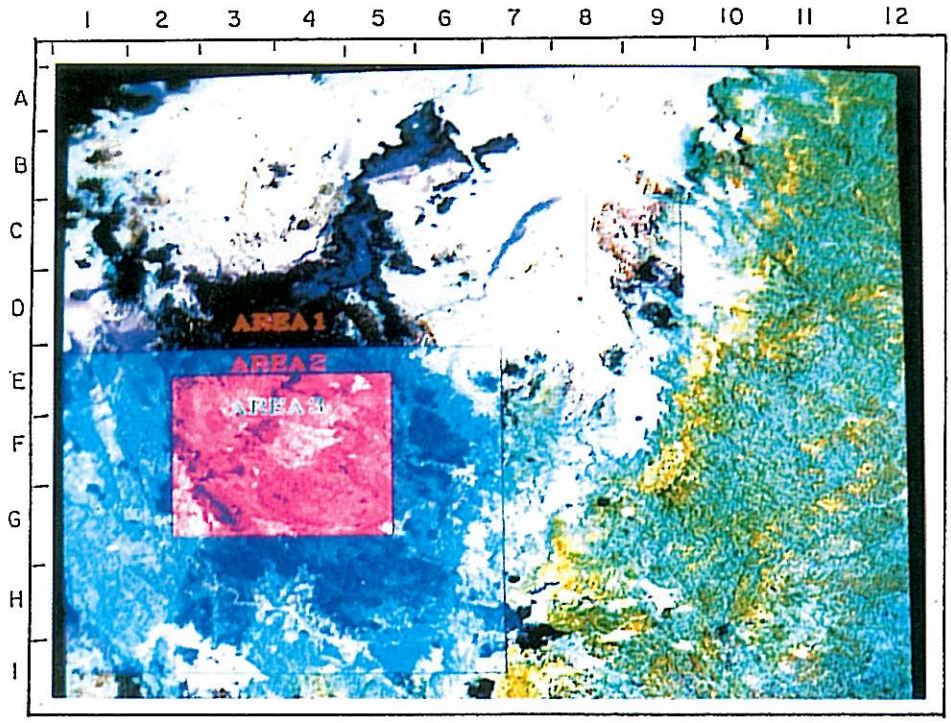


PLATE 1. Location of the selected areas used in this work.

combination of spectral and textural characteristics is used to identify and map the rock units.

DISCUSSION OF THE PRELIMINARY GEOLOGIC MAP

Precambrian metamorphic rocks, which include meta-volcanic and meta-sediments, are the oldest exposed rock unit identified and plotted in (Fig. 3).

It was very difficult to identify this unit due to its mixing with the surrounding units especially rhyolite. In the images produced, these units have similar shades of colour except in Plate 2 where the metamorphic rock units appear as blue and rhyolite unit appear pink and in some places dark yellow when mixed with some sediments. The fractures of dikes in the rhyolite unit is an alternative way to distinguish these units. Precambrian diorites to gabbros unit is identified and labelled as the second rock unit according to age. This interpretation is based on the difference in spectral reflectance of this unit compared with the adjacent granite unit. In previous studies this unit was included with the granite unit. It appears completely different from the adjacent granitic unit. It is darker than the granitic unit due to the richness of this unit in Fe and Mg.

The third unit identified in this map is the granitic unit which includes the syntectonic and post-tectonic granites. This unit appears very clear in Plate 3 as yellow colour. The fourth rock unit is Ordovician rhyolite covering most of the central part of the area. It is completely mixed with the metamorphic and the basaltic flow units. It is difficult to distinguish between them. In Plate 2 it is possible to distinguish areas where rhyolite unit appears as pink to dark yellow and metamorphic rock unit appears as light blue colour where as basaltic flow units appear as deep red to dark blue. Another characteristic that is helpful in identifying these units, is the abundance of fractures and dikes (green lineaments) in the rhyolite unit (Plate 4). Palaeozoic sandstone is the fifth unit recognized in the area. It appears as green colour and deep yellow. This is due probably to variation in Fe-minerals.

Tertiary sandstones appear similar to Palaeozoic sandstones. The discrimination between them is very difficult and is based on previous studies which refer to this unit as Tertiary cross bedded sandstone. Extensive basaltic flows Tertiary cover most of the area. They appear as black to very dark blue (Plate 3) and also as deep red in Plate 2. In some places, when covered by aeolian material, they appear as grey colour. The youngest unit identified in this geologic map include Quaternary alluvium and Wadi sediments. They are deposited in the low areas and valleys distributed in various parts of the area and appear as white in colour. This white colour reflects the high albedo of this kind of material.

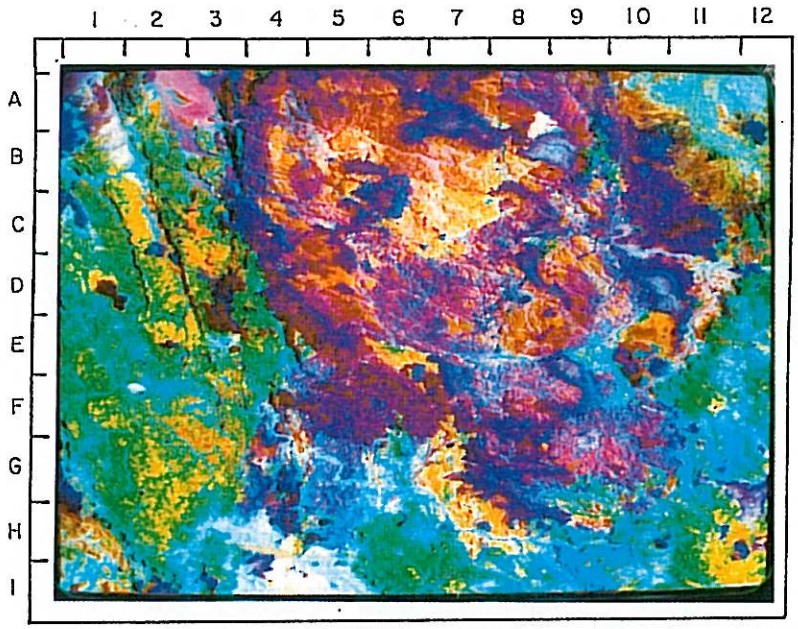


PLATE 2. Automatic stretched principal component image, Pc3, Pc1, Pc2 as RGB.

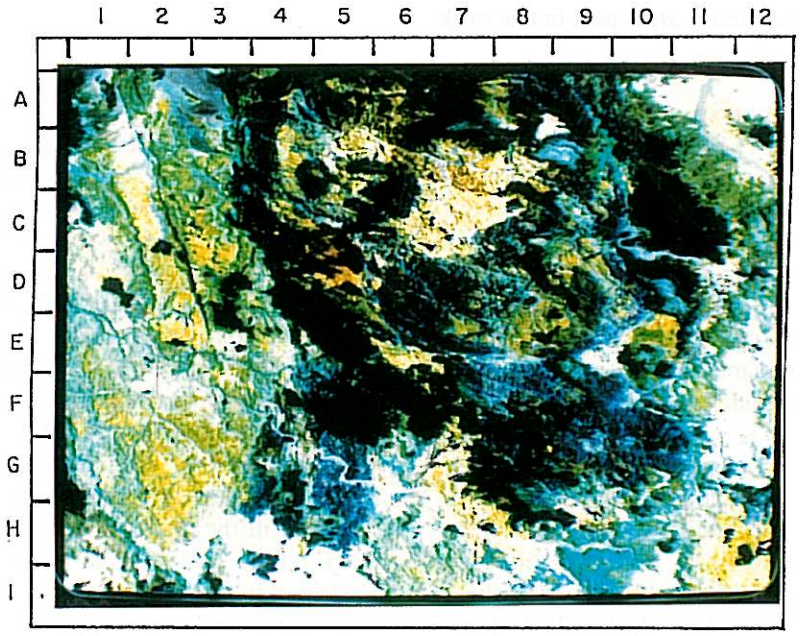


PLATE 3. Automatic stretched FCC image (bands 7, 5, 4 as RGB).

DISCUSSION OF THE PRELIMINARY LINEAMENTS MAP

Figure 4 shows the most clear lineaments which are recognized in Plate 5. These lineaments and edges are enhanced by using edge enhancement technique. Laplacian (3 × 3) filtering was applied which enhanced the edges in all directions. These lineaments reflect, to some extent, the structural style of the area.

As shown in this map the area is dominated by four kinds of structural features:

(1) Long lineaments (from 3–10 km) which reflect faults, dikes.
(2) Short lineaments (from hundreds of meters to 3km) which may represent small faults, dikes or fractures.
(3) Ring structure which reflects the complex structure in this area. It is a curved line and appears to be filled with green siliceous dikes.

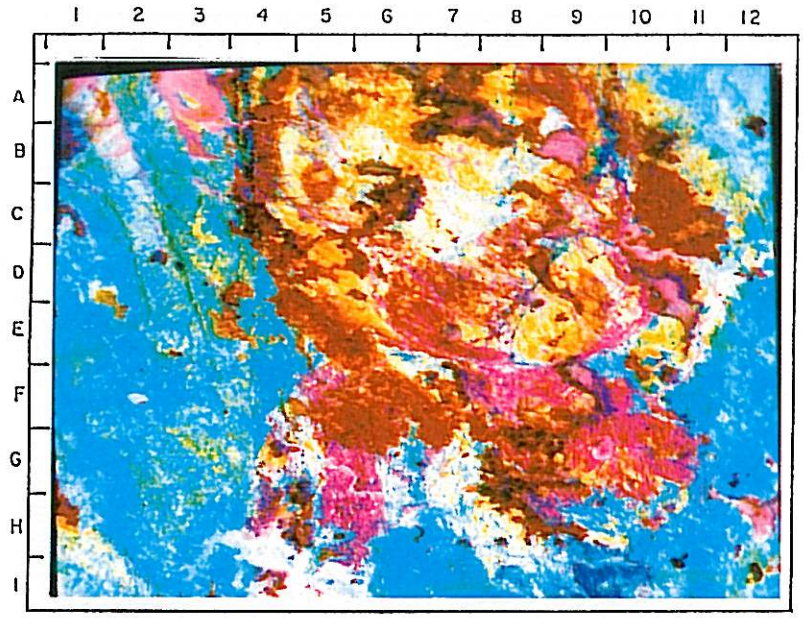


PLATE 4. Histogram equalization of the coloured image. (Ratios 7/5, 7/4 and TM band 4 as RGB.)

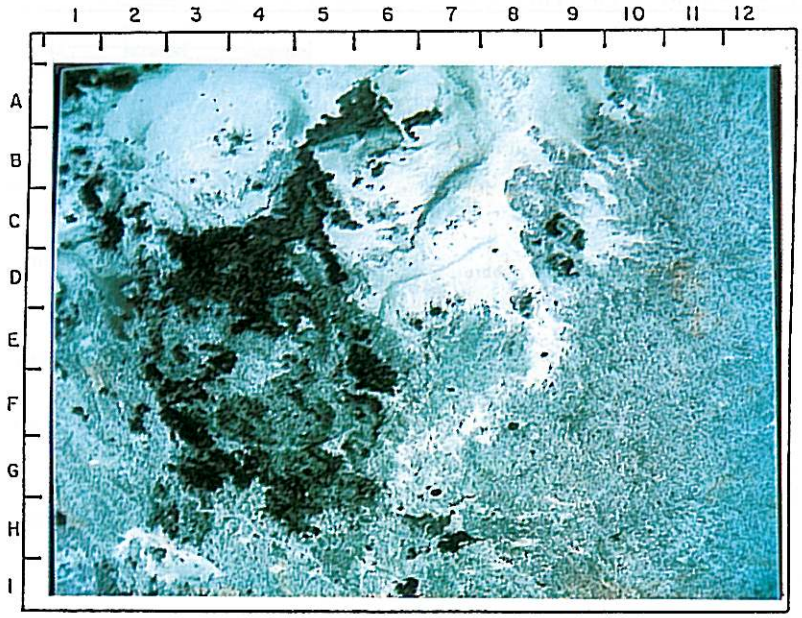


PLATE 5. Edge enhanced image of (Pc1) of the area. Laplacian (3 × 3) filter.

(4) Circular and semi-circular features concentrated mainly in the eastern part of the area and covered by Palaeozoic sandstone. The majority of these circular features are granitic intrusions which are uncovered partly or completely by erosion. They may represent intrusive bodies which have not quite reached the level of the present land surface. Such buried intrusives should make a promising target for mineral exploration.

This complex structure proves that the area under study has suffered many deformation phases. Three lineament trends are recognized; a NW–SE trend which is mainly dominant in Palaeozoic and Tertiary sandstones. Secondly few lineaments take NE–SW trend which is dominant in Palaeozoic and Tertiary sandstone. These two trends may belong to the main orogenies. The Caledonian orogeny took place from the beginning until the middle of Palaeozoic and takes NW–SE trend. The Hercynian orogeny took place through the middle of Palaeozoic until the beginning of Mesozoic Era. This orogeny takes a NE–SW trend. The third lineament is N–S trend and is mainly dominant in Precambrian metamorphic rocks.

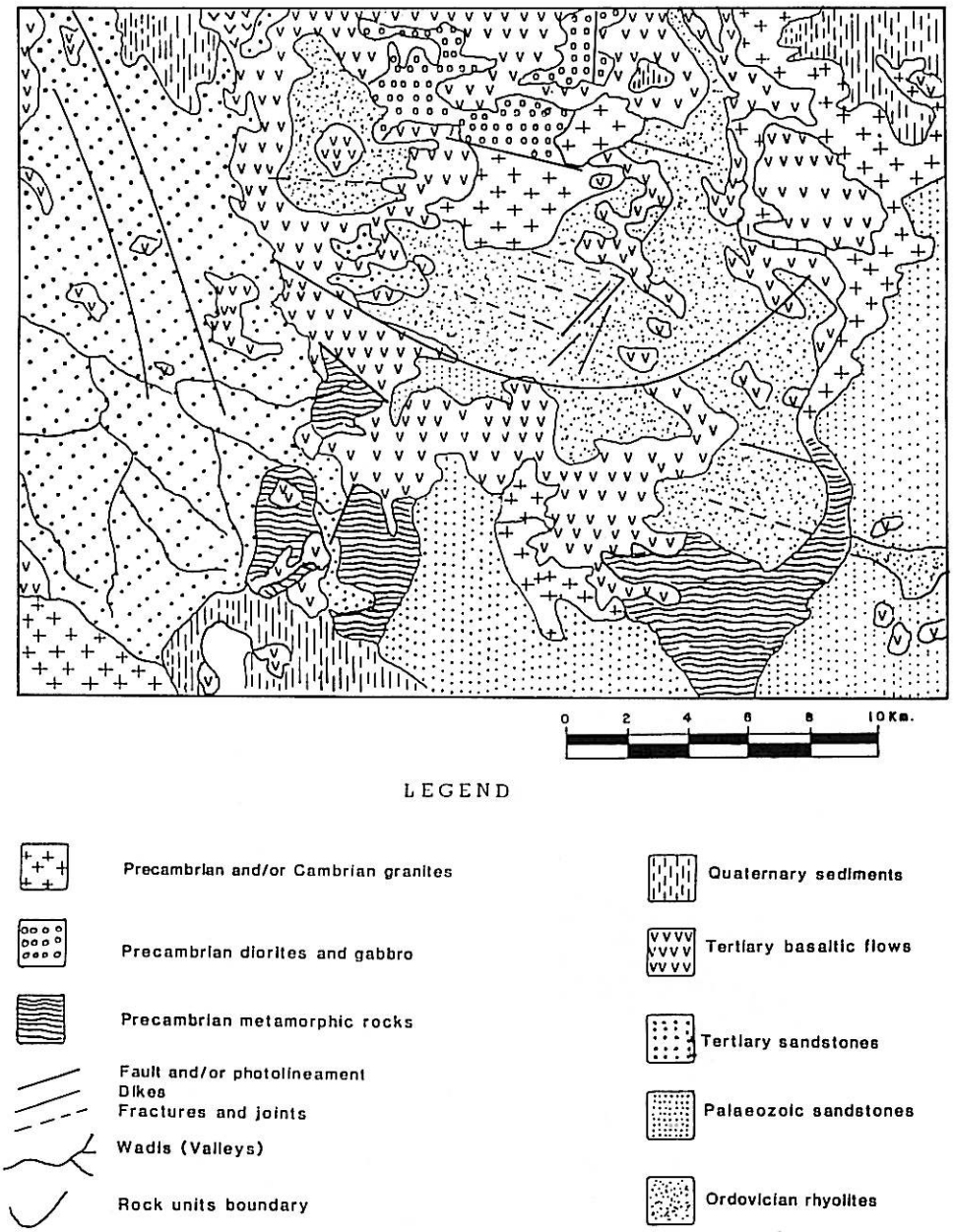


FIG. 3. Preliminary geological map of the area based on the interpretation of plates 2, 3 and 4.

COMPARISON OF GEOLOGICAL INFORMATION FROM LANDSAT TM IMAGERY AND AERIAL PHOTOGRAPHS

In order to compare data from Landsat TM Imagery and Aerial Photographs, four parameters are considered. These parameters are geometric accuracy, rock unit boundaries, lithology, and structure.

(1) *Geometric accuracy*

In this work Landsat TM images which are compared with aerial photographs proved more accurate. This is due to the fact that they are more stable than aerial photographs especially for areas of tens of kilometer or more. Using Landsat imagery it is possible to use only one image to study these scales instead of a large number of aerial photographs from which one has to build a mosaic to cover these scales. This mosaic is a major reason for loss of positional accuracy of the geological features. Also Landsat TM imagery has the advantage of digital geometric correction over aerial photographs.

(2) *Rock unit boundaries*

The use of satellite imagery can be helpful in rapid delineation of the boundaries between the rock units by virtue of its synoptic overview, multispectral and multitemporal coverage. The geological boundaries have been mapped with a high-contrast boundary with

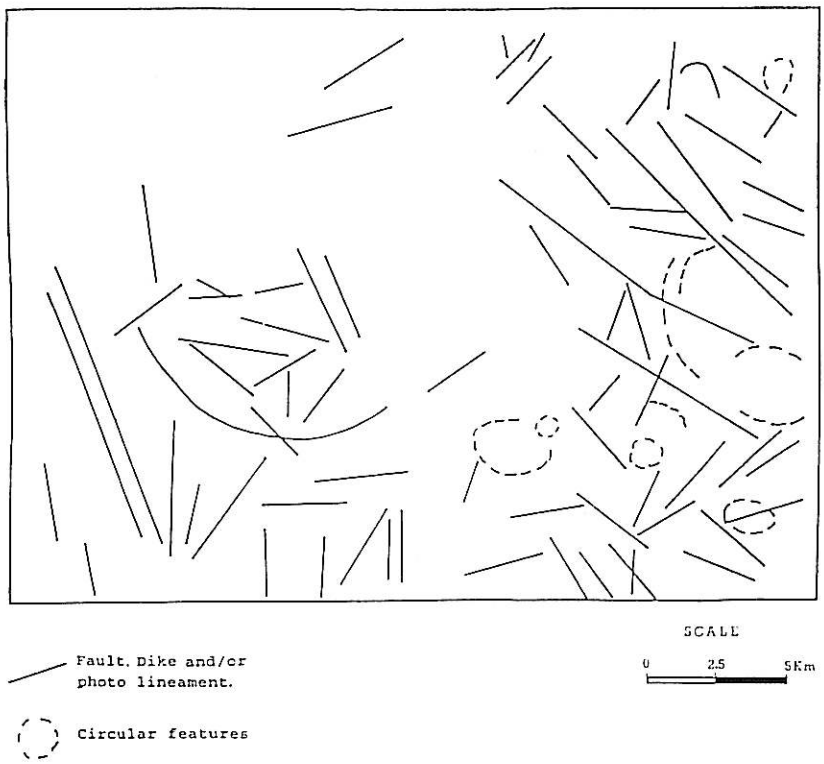


FIG. 4. Preliminary lineaments map of the area based on the interpretation of plate 5.

the aid of different bands of Landsat TM. Most rock units are well delineated, for example the boundaries between the granitic unit and diorites to gabbros unit in region B7,8 and C7,8 (Plates 2 and 3) have been clearly marked. These units appear as one unit in the aerial photographs.

(3) *Lithology*

The problem of differentiating between units exposed as small outcrops in the area has to be overcome by computer methods, using many image processing techniques. The most effective techniques are: principal component analysis which is very helpful in lithological discrimination. This can be seen in Plate 2 where the basaltic flows appear in two or three units and this colour difference may be indicative of the age of the rock. The other technique is ratio images which enhanced the differentiation even within one unit (Plate 4). Sandstone in the western part of this area appeared in green and yellow colours. These findings point out that satellite imagery, with the advantages of multispectral coverage and digital image processing, is more effective than aerial photography.

(4) *Structure*

Aerial photographs are more effective in delineating and determining the local structures mainly as a result of better spatial resolution and stereoscopic viewing. However Landsat imagery proved more effective in interpreting regional structures.

CONCLUSIONS

The use of more than one type of remote sensing technique is very effective. Aerial photographs proved useful in delineating the local structures, mainly as a result of better spatial resolution and stereoscopic viewing. Landsat imagery proved more effective in the regional structural analysis due to its ability to cover large areas. Circular features are detected easily by Landsat imagery. By using edge enhancement technique, most of the structural features are clearly mapped. High-contrast rock unit boundaries are mapped through the application of colour ratios and principal component analysis images. Unmapped lithologic unit labelled as diorites to gabbros is identified as a result of differentiation in its spectral reflectance over the surrounding rock units. The problem of locating and enhancing the small outcrops were overcome by computer methods, using many image processing techniques. A geologic map and a lineaments map were constructed in order to show most of lithological and structural features which appeared in the produced images. Eight rock units have been identified and plotted in the geologic map. The mapping was based on the spectral reflectance which gives different colours in false colour composite images used in this paper. Structurally, the area is dominated by two lineament trends with a few taking a trend of N–S direction as shown in the lineaments map. The common trend is NW–SE which takes place especially in Palaeozoic

and Tertiary sandstone to the east and west sides of the area.

The results achieved indicate that Landsat TM imagery is more effective than aerial photographs by virtue of its synoptic overview, multispectral and multitemporal coverage. It is also more simpler, faster and cost-effective.

ACKNOWLEDGEMENTS

The study was carried out at Dundee University, U.K. I am indebted to the Management of the Petroleum Research Centre, Tripoli, Libya, for their help. Also to Dr. R.A. Vaughan of Dundee University for guidance and advice and to Dr. M.J. Salem and Dr. A. El Makhrouf for reviewing and criticizing this work.

REFERENCES

Abdulnasser, K.M., 1992. Comparison of geological information from computer enhanced Landsat TM imagery and aerial-photography in Jabal Eighee area, south central Libya. Unpublished MSc thesis pp. 120, Dundee University.

Conant, A.C., and Goudarzi, G.H., 1977. Geological map of Libya 1:2,000,000 (2nd edition): Industry Res. Cent. Tripoli.

Crosta, A.P., and Moore, J.M., 1989. Geological mapping using Landsat Thematic Mapper imagery in Almeria province, south-east Spain. Int. J. Sen. v. 10, no. 3, pp. 505–514.

Drury, S.A., 1986. Remote sensing of geological structure in temperate agricultural terrains. Geol. Mag., no. 123, pp. 113.

El-Makhrouf, A.A., 1988. Tectonic interpretation of Jabal Eghei area and its regional application to Tibesti orogenic belt, south central Libya. Jour. Afr. Sci. v. 7, no. 7/8, pp. 945–967.

Industrial Research Centre, 1978. Total intensity aeromagnetic map of Jabal Nuqay area, Exploration and Geophysics Division, Department of Geological Research and Mining, IRC Tripoli-Libya.

Jensen, J.R., 1986. Introductory Digital Image Processing: A Remote Sensing Perspective. Prentice-Hall pp. 387.

Missallati, A., Prelant, A.E. and Lyon, R.J.P., 1979. Simultaneous use of geological, geophysical and Landsat digital data in uranium exploration. Rem. Wen. Envir. 8: pp. 189–210.

ABBREVIATIONS

TM	Thematic Mapper
MSS	Multispectral scanner
CCT	Computer compatible tape
B&W	Black and White
Pc	Principal component
RGB	Red, Green and Blue
FCC	False colour composite

PRJ, Vol. 6 (January 1994); P. 75–84, 11 FIGS, 1 TABLE.

RESERVOIR QUALITY ANALYSIS - AN OVERVIEW WITH EXAMPLES FROM THE SIRT BASIN

R.C. Thom*

تحليل جودة المكمن : نظرة عابرة مع أمثلة من حوض سرت

ر. سى. ثوم

يمكن تعريف جودة المكمن كتقدير كيفي لقابلية أي صخر لإنتاج الموائع ، التي تعتبر المواد الهيدروكربونية أفضلها. وعادة ما يتم تحديدها باستعمال وسائل الشرائح المجهرية الرقيقة والمجهر الإلكتروني الفاحص (SEM) والأشعة السينية المنكسرة (XRD).

تشمل المشاكل المرتقبة التي قد تؤثر على جودة المكمن ، هجرة الرواسب الدقيقة (الحجر الرملي بحقل المسلة) والحساسية للأحماض (تكوين خليفة) وإنتفاخ الطفلة.

ومن المهم تحديد نوع وكمية المعادن التي تهديدها قائم ، كذلك مواقع وأشكال هذه المواد بالنسبة لنظم الفجوات. هذا بالإضافة إلى أهمية المسامية والنفاذية بالنسبة لوجود المكمن. وعموماً ، فإن جيولوجي الإستكشاف والتطوير يستعملون المسامية المستمدة من تحاليل السرود ولبب الآبار (أي المسامية الكلية). وفي كثير من المكامن ، يتألف قسط مهم للفراغات من فراغات معزولة لا تساهم بشيء للنفاذية (تكويني خليفة وزلطن) إذا من المهم تحديد نسبة المسامية المؤثرة ألى المسامية غير المؤثرة.

يمكن إعتبار دشيش الحفر عينة مباشرة حول مكمن محتمل ولكن المعلومات المستمدة من هذه المواد لا تعتبر عادة ضمن العوامل التي تحدد استكمال البئر من عدمه. ويمكن الحصول أيضاً على معظم معلومات جودة المكمن المستمدة من عينات لبب الصخر، ومن فحص دشيش الحفر في الشرائح الرقيقة مجهرياً وباستعمال المجهر الألكتروني الفاحص ومن أمثلة ذلك الهيكل المعدني ، المجموعات المعدنية المتحورة ، وأنواع الفراغات (المسام) وهكذا.. في كثير من الحالات يمكن الحصول على النفاذية ومسامية تحليل لب الصخور بطريقة حسابية من فحص دشيش الحفر.

وقد تم توضيح تقنيات الفحص المجهري للصخور في تحديد جودة المكمن باستعمال أمثلة من تكوين خليفة وتكوين زلطن علاوة على الحجر الرملي بحقل المسلة.

ABSTRACT

Reservoir Quality can be defined as a qualitative estimate of a rock's ability to produce fluid, preferably hydrocarbon. It is generally determined using thin section petrography, scanning electron microscopy (SEM) and X-ray diffraction (XRD) techniques.

Potential problems which may affect reservoir quality include fines migration (Messla Field Santstone), acid sensitivity (Khalifa Formation) and swelling clays. The type and quantity of potentially damaging minerals, plus the position and morphology of this material with respect to the pore system is significant. In addition, porosity and permeability are obviously important with respect to reservoir quality. In general, exploration and development geologists use log and core analysis derived porosity (i.e. total porosity). In many reservoirs a significant proportion of the pore system consists of isolated pores which do not contribute to permeability (Khalifa and Zelten Formations). It is important to determine the proportion of effective vs non-effective porosity.

Drill cuttings can be small pieces of a prospective reservoir, though the information available from this material is not often incorporated into completion

*AGAT Laboratories Ltd. 3801-21 Street N.E., Calgary, Alberta Canada T2E 6T5.

decisions. Most reservoir quality information that can be obtained from core samples can also be obtained from thin section and SEM examination of drill cuttings, for example, framework mineralogy, diagenetic mineral suite, pore types, etc. In many cases, permeability and core analysis porosity can be empirically derived from cuttings.

The use of petrographic techniques in the determination of reservoir quality is illustrated using examples from the Khalifa and Zelten Formations plus the Messla Field Sandstone.

INTRODUCTION

Reservoir Quality and fluid sensitivity can be determined using a combination of thin section petrography, scanning electron microscopy (SEM) and X-ray diffraction (XRD) techniques (AGAT Laboratories, 1983).

Thin section petrography (core, drill cuttings, outcrop or sidewall plug samples) generally forms the basis of any reservoir quality study (Fig. 1), providing information on primary mineralogy (framework and matrix composition), diagenesis and pore types. This technique is also useful for determining the position of potentially reactive minerals with respect to the pore system (i.e. authigenic kaolinite within pores is far more likely to contribute to a fines problem than detrital kaolinite within argillaceous rock fragments).

Standard thin section petrography involves two dimensional examination of the sample under magnifications of 25× to 400×. In some cases, it is not possible to distinguish clays, fines or precipitates in the pore system and scanning electron microscopy (SEM) may be necessary.

SEM's are capable of magnifications between approximately 10× and 100,000×, while maintaining a great depth of field; thus, scanning electron microscopy provides high magnification three-dimensional views of the rock, which can be used to supplement or enhance information derived from thin sections. SEM samples generally consist of a 1 centimetre sample of freshly broken core or drill cuttings.

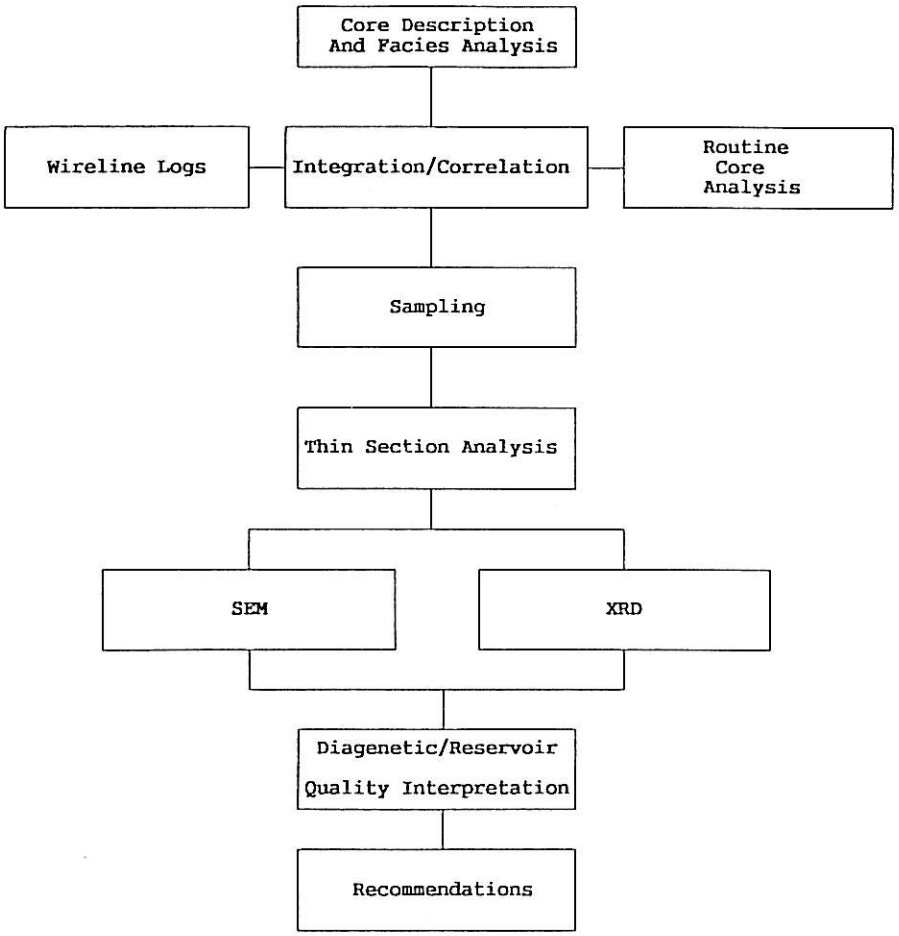


FIG. 1. Generalized flowchart of the reservoir quality analysis process.

SEM examination is particularly useful for the determination of pore and pore throat morphology, as well as the identification and distribution of clays and other fines in the pore system.

Most SEM's have an attached dispersive X-ray energy spectrometer (XES) which can be used to help identify minerals by determining the elemental composition. This instrument can be used to determine the elemental makeup at a single point (i.e. to look at zonal variations within a single grain) or within a selected area (incorporating more than one grain or crystal).

X-ray diffraction (XRD) is another analytical tool used to complement thin section petrography, XRD can determine the type and approximate abundance of minerals in a powdered rock sample, and is particularly good at clay identification. This technique is based on the characteristic reflection of X-rays by crystal lattice planes within minerals. Each mineral has diagnostic X-ray pattern with known peak locations and intensities. Amorphous (non-crystalline) material (e.g. bitumen) will not diffract X-rays and will not be identified by X-ray diffraction analysis.

Both bulk and clay-fraction XRD analyses are normally run on a rock sample. The bulk analysis is performed on the entire powdered sample to provide the relative mineral percentages. In a clay-fraction analysis the clays are concentrated by separating the less than 4 micron size fraction (using centrifuge and decanting techniques) from the bulk sample. This concentration of clays is necessary because these potentially reactive minerals are often present in small amounts and their presence would be masked by the abundance of other minerals in a bulk sample. Clay-fraction samples are commonly glycolated (to identify swelling clays), heated and/or acid washed (to distinguish between kaolinite and chlorite).

XRD is very useful for identification of minerals, particularly clays; however, the position of these minerals with respect to the pore system cannot be determined by this technique. In addition, XRD analysis cannot distinguish between minerals with the same composition (e.g. monocrystalline quartz, chert and silica within rock fragments will all show as quartz).

A comparison of the benefits and limitations of thin section petrography, SEM and XRD techniques is provided in Table 1. It is important to realize that only a small portion of the reservoir is being examined and that the selection of representative samples is critical.

FINES MIGRATION

Permeability reduction as a result of migration of formation fines, can be significant when drilling, completing and/or producing a reservoir (Gabriel and Inamdar, 1988). Loosely attached fines (detrital clays, authigenic kaolinite, authigenic illite, silicate fines-disaggregation of lithic clasts, carbonate fines-dolomite, siderite, calcite) may be mobilized and move from the interior of pores and/or pore walls to collect at pore throats, thus reducing permeability.

Table 1. Comparison of Petrological Techniques

Equipment	Uses/Benefits	Limitations
Polarized Microscope	– mineralogy – types and quantity – framework grains – matrix – cements, some clays – porosity/permeability controls – diagenetic modifications – grain size determination	– upper limit mágnification ×400 – two-dimensional – can't identify fine matrix/clay minerals – thin sections take at least 1 day to prepare
Epi-Fluorescent Microscopy	– porosity distribution – fracture/matrix/vug relationships – effective porosity – microfractures	– same as polarizing microscope – best for carbonates – requires fluorescent dye
X-ray Diffraction	– rapid analysis of mineralogy – bulk sample, whole rock – clays in clay fraction	– semi-quantitative – accuracy dependent on mineral crystallinity – no information on mineral distribution
Scanning Electron Microscopy	– detailed examination of pore system – high magnification – mineral identificaton with XES system – use in conjuction with displacement tests – metallurgical samples	– small sample may not be representative

The following points have been stated regarding fines migration:

- Migration will only occur if the phase that wets the fines is mobile, i.e. in a water-wet zone producing oil or gas, fines migration will only occur when water is produced (Muecke, 1979).
- The relationship between the sizes of pore throats and fines is another factor affecting the degree of permeability reduction as a result of fines migration. Fines can collect at pore throats if their diameter is 1/3 or more of the throat diameter.
- The fluid production (or injection) rate at which significant fines migration initiates permeability reduction is termed the "critical velocity". Critical velocity is not attained when only the non-wetting phase is flowing, indicating the importance of wettability. It has been determined that fines are mobilized even at subcritical velocities, but that pore throats are not blocked in sufficient quantities to create significant permeability reduction.
- Authigenic kaolinite migrates as "booklets" rather than as individual platelets and authigenic illite can act as "fishnets" to catch mobile fines (Porter, 1989).
- Selby *et al.* (1988) showed that fines flow in porous media was influenced by:
  (i) the initial amount of fines
  (ii) the fluid flow rate
  (iii) the size and shape of the framework grains
  (iv) the size and density of the fines
  (v) the overburden pressure
- Migration can occur if the salinity of injection water is lower than formation water, or if the divalent ion concentration is reduced or replaced by monovalent ions (Gray and Rex, 1966). Changes in pH can promote migration and gradual changes in the salinity of injection water tend to minimize migration (as compared to significant migration if the zone is "shocked" with water of very different salinity to the formation brine).

Thin section petrography can be a useful "first step" in the identification of formation fines. SEM examination is often used to determine the type and distribution of fines plus the size of fines in relation to pore throats. XRD analysis is used for identification of clay types and, in conjunction with thin section work, gives an approximate abundance of clays.

Following the identification of a potential fines migration problem, core flow tests at reservoir conditions of temperature and pressure, can determine the degree of permeability reduction at different interstitial fluid velocities (Fig. 2a). The effect of water composition on fines migration and the "critical velocity" may also be determined in flow tests.

If production and injection rates are below the "critical velocity" then significant permeability reduction as a result of fines migration is not expected. In cases where it is not feasible to keep interstitial flow velocities below the "critical velocity", and where significant fines migration has already damaged a zone, a fracture stimulation will provide large flow paths and reduce near wellbore interstitial flowing velocities (thus minimizing potential fines migration) (Economides and Nolte, 1989).

Clay stabilizers have been used to prevent mobilization of clay fines (Sydansk, 1983). These stabilizing agents coat the surface of the clay particles and prevent them from "seeing" salinity changes during waterflooding or steamflooding. Hydroxyaluminum, polyacrylamides, asphaltenes and polyvinyl alcohol solutions have been used as stabilizers. Core flow tests at numerous laboratories suggest that many commercially available clay stabilizers cause more damage as a result of reduced pore volumes than fines migration would have caused in an untreated rock.

The Messla Field Sandstones are very fine to medium grained, moderately well sorted sublitharenites with significant proportions of authigenic kaolinite (Fig. 2b). This diagenetic clay has precipitated within the pore system and appears to be migratable to pore throat blocking positions.

ACID SENSITIVITY

Using acid in completion and stimulation can result in formation damage as a consequence of one or more of the following factors:

(i) precipitation of iron hydroxide gels
(ii) precipitation of fluoride and silicate gels
(iii) release of fines
(iv) fabric collapse
(v) creation of emulsions or "sludge"

(i) Reactions between spending treatment acid (either during a matrix acid squeeze or an acid fracture stimulation) and iron-bearing minerals can result in the precipitation of permeability-reducing iron hydroxide gels. Iron within the crystal lattice of these minerals (chlorite, siderite, ferroan carbonate, hematite) goes into solution and may subsequently precipitate as the acid spends; ferric (Fe^{3+}) iron precipitates when the pH exceeds 2.2, whereas ferrous (Fe^{2+}) iron will only precipitate in the 7 to 9 pH range. Ferrous iron is easily converted to the ferric state if oxygenated fluids are present. Iron scale from corroded tubulars (drill pipe, tubing and casing)

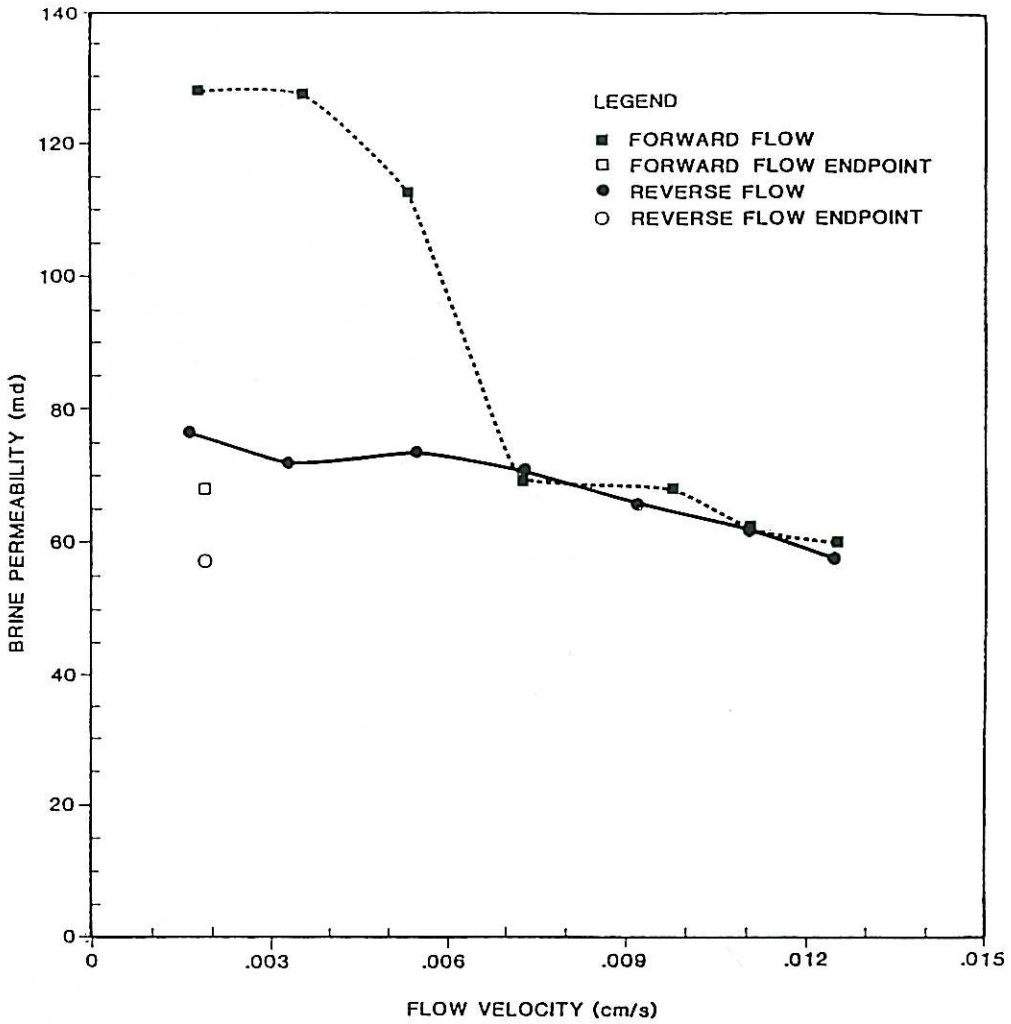


FIG. 2(a). Fines mobilization results showing significant damage (glauconite formation).

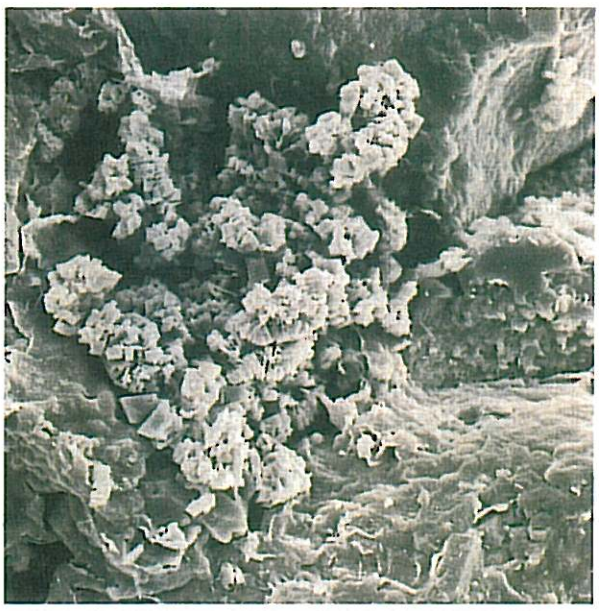


FIG. 2b. SEM view of the Messla Field sandstone showing potentially migratable authigenic kaolinite.

is also a major source of iron hydroxide precipitation.

Iron sequestering (chelating) agents can be effective in preventing iron hydroxide gel precipitation (Smith, *et al.*, 1965), forming a stable complex with dissolved iron and keeping it in solution. Oxygen scavengers prevent conversion of ferrous iron to the more dangerous ferric iron. It is important to determine the optimum concentration of sequestering agents, overuse may result in severe gel precipitation (Smith, *et al.*, 1965). Organic acids such as acetic, citric and lactic acids are commonly used as sequestrants in hydrochloric (HCl) acid treatments. If the treatment acid is recovered rapidly, the pH may not rise above 2 and dissolved iron can be maintained in solution without a sequestrant. Once iron precipitation has damaged the near wellbore area, a small-scale fracture treatment may bypass the damage.

(ii) Hydrofluoric (HF) acid is normally used in conjunction with hydrochloric (HCl) acid to remove

drilling mud damage in sandstones (Hendrickson, 1965). HF acid will dissolve silicates (including quartz, feldspar and clay) and carbonates though the reaction rate is low compared to the reaction of HCl acid with limestone. The most common combination of the two acids (often called "Mud Acid") is 12% HCl–3% HF. Hydrochloric acid (acts as a converter to produce HF acid from ammonium salt), dissolves HCl-soluble material to prevent the HF acid from spending too rapidly and prevents the precipitation of calcium fluoride (CaF_2).

In poorly designed "Mud Acid" treatments, calcium fluoride (CaF_2), sodium fluoride (NaF) and/or sodium silicate (Na_3SiO_6) precipitates may significantly reduce near wellbore permeability. Unless carbonate material is removed prior to injection of HF/HCl acid into a zone, significant fluoride precipitation will result. Therefore, mud acid is not used in carbonate reservoirs and it should always be preceded by an HCl acid preflush in a sandstone to remove carbonate material. Reactions between sodium-rich formation fluids, feldspars, clays and HF acid can result in sodium silicate and fluosilicate precipitates; therefore, the use of HF/HCl acid treatments should be considered carefully.

(iii) Release and subsequent movement of "fines" to pore throats may create severe permeability drops in carbonates and carbonate-cemented sandstones. Carbonate material may be only partially dissolved, resulting in mobile carbonate remanat "fines" which could block pore throats.

(iv) Excessive dissolution of carbonate zones can result in significant permeability reduction from fabric collapse.

(v) Hydrochloric acid may react with oil to form solid or semi-solid particles called sludge; this material can severely restrict or completely plug the near wellbore area. Sludge problems are most common in Alberta and California.

Viscous emulsions (a mixture of two immiscible liquids) may form when treatment acid (water-based) contacts reservoir oil, severely inhibiting production.

Both sludges and emulsions may be removed by using appropriate surfactants (surface active agents), which reduce interfacial and surface tension and resulting a more miscible mixture of oil and water (acid).

In certain areas, the base of the Khalifa Formation is a ferroan dolomite cemented arkosic sandstone (Fig. 3). Iron within the dolomite cement may react with spending treatment acid to precipitate permeability – reducing iron hydroxide gels.

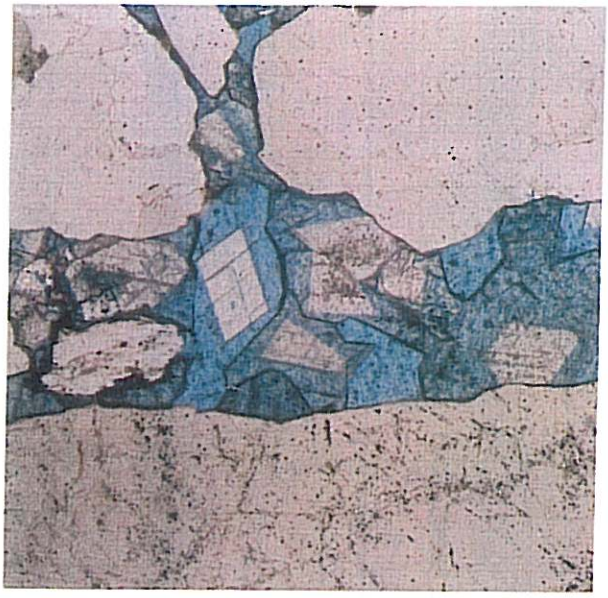


FIG. 3. Thin section view of a ferroan dolomite (stained blue) cemented arkosic sandstone with the Khalifa Formation. Iron within the dolomite could react with spending treatment acid to precipitate damaging iron hydroxide gels.

WATER SENSITIVITY

Within a reservoir, clay minerals are in equilibrium with interstitial brine and are generally in a flocculated, non-expanded state. Introduction of fresher water into a water sensitive reservoir may result in significant permeability reduction as a consequence of one or both of the following phenomena:

(i) clay swelling
(ii) clay deflocculation

(i) If fluid with a lower cation concentration (fresher water) is introduced into a zone with swelling (smectitic) clays, significant swelling and dispersion of these clays may result in severe permeability reduction. In addition, large volumes of fluid trapped within the expanded clay lattice may indicate a high water saturation (Sw) on logs, even though the zone could produce water-free hydrocarbon.

Expandable clays include all those in the smectite group, including mixed-layer clays such as smectite-illite (the most common) and smectite-chlorite (corrensite). Smectite, the only clay that swells, has weak internal bonding within its crystal lattice which allows cations such as Na^+, Ca^{2+} and K^+ to occupy interlayer positions. These cations are readily displaced by water molecules, which occupy a greater volume than the displaced cations, thus resulting in significant expansion of the lattice (from 10A to 20A). The degree of swelling is dependent on the

original cations and the composition of the pore water.

The most effective and inexpensive clay stabilizer is KCl (potassium chlorite), generally in brine concentrations of approximately 3%. Potassium can replace sodium and calcium cations within the crystal lattice, resulting in stronger interlayer bonding. Cationic polymers (hydroxyaluminum, zirconium oxychloride), have also been used as clay stabilizers, but are expensive.

(ii) Kaolinite and illite, the most common clays in sandstones, do not swell if contacted by relatively fresh water; however, severe permeability reduction may occur as a result of deflocculation and subsequent migration of these clays. Johnson and Norton (1941) have proposed a double-layer concept to explain flocculation and deflocculation. When clays are submerged in water containing an electrolyte, an inner layer of negatively charged hydroxyl ions (OH) and an outer layer of positively charged cations, forms on the surface of the clay. The clay is flocculated when the cation is close to the clay surface and deflocculated when the cation is relatively distant. Apparently Ca^{2+}, Mg^{2+} and H^{+} cations promote flocculation whereas Na^{+} creates deflocculation.

Core flow tests have shown that problems related to clay deflocculation are most severe when a rock is "shocked" by flowing significantly fresher water through the pore system (Mungan, 1965). If the salinity of the injected water is gradually reduced from the original formation salinity to fresh, permeability reduction is minimal (Khiler, *et al.*, 1983).

Commercially available clay stabilizers (polyacrylamides, asphaltenes and resins, polyvinyl alcohol, hydroxyaluminum, etc.) coat clay surfaces, isolating them from changes in pore fluid composition (Sydansk, 1983). However, these stabilizers may themselves result in permeability reduction by taking up pore volume.

PORE TYPES

With respect to hydrocarbon production there are basically two types of pores:

1. Effective Pores:
   - Intergranular/Intercrystalline
   - Secondary Dissolution (Granomoldic)/ Biomoldic
2. Non-Effective Pores:
   - Secondary Dissolution (Granomoldic)/ Biomoldic
   - Microporosity

Obviously it is very important to determine the proportion of these two pore types in a reservoir in order to accurately predict reserves, sweep efficiency, etc.

EFFECTIVE PORES – Intergranular pores are generally well connected to each other and the associated permeability in a "clean" (clay-free) porous sandstone is usually high. Intercrystalline pores represent the carbonate equivalent of intergranular pores. Secondary dissolution pores are created by the leaching of unstable framework grains (feldspar, chert, rock fragments). If these pores are connected by a network of intergranular pores they contribute to permeability and are effective. The same is true for effective biomoldic (vuggy) pores, created by dissolution of fossil fragments and connected by intercrystalline pores.

In pore systems dominated by effective porosity, there is a "normal", roughly linear relationship between porosity and permeability, i.e. one increases with the other.

NON-EFFECTIVE PORES – In cases where secondary dissolution or biomoldic pores are the dominant or only pore type, the permeability may be anomalously low because of the generally isolated character of these pores.

Microporosity, commonly associated with detrital and authigenic clays, is generally non-effective with respect to hydrocarbon production, as a consequence of the very high capillary pressure forces at the small pore throats. These micropores may contain significant volumes of bound (connate) reservoir brine or hydrocarbon. "Dirty" (argillaceous) sandstones may contain large proportions of connate water in micropores, leading to a "wet" response on the resistivity log, yet the zone may produce water-free oil or gas. In argillaceous sands, the amount by which core analysis (total) porosity exceeds thin section (effective-visible) porosity is generally considered to be representative of microporosity.

Where pore systems are dominated by isolated non-effective pores, the relationship between porosity and permeability can be complex and non-linear. At low porosity values, the relationship with permeability may be linear, suggesting that this portion of the pore system is interconnected and effective. As porosity increases there is very little increase in permeability, indicating that this portion of the pore system is non-effective (either micropores or isolated dissolution/biomoldic pores).

Pitman (1979) suggested that there are four basic pore types in sandstones: intergranular (effective), dissolution (effective to non-effective), micropores (non-effective) and fractures (effective). The first three pore types can be called matrix related porosity. Understanding the pore geometry is essential in predicting the productive capability (recovery efficiency) of a reservoir. Logs cannot distinguish between effective

and non-effective pores, the distribution of which affects the recovery efficiency, reserves, sweep efficiency, etc.

Another excellent paper on pore systems was written by Wardlaw and Casan (1978), in which they attempted to estimate recovery efficiency by quantifying visual characteristics of pore systems. They considered the following parameters to be of prime importance with respect to oil recovery: pore to throat size ratio; throat to pore coordination number; and type and degree of nonrandom heterogeneity.

The impetus for their work was the lack of relative-permeability data (which is required to estimate oil-recovery efficiency), because of the high cost of these tests. Using their visual method a large number of samples can be examined cheaply, providing a more representative sample base for relative-permeability measurements.

The Zelten Porosity Zone of the South Nasser Reservoir in the Sirt Basin, Libya is predominantly a foraminifera and echinoderm packstone with a pore system dominated by intercrystalline microporosity (Fig. 4a). Larger, intraparticle, vuggy and moldic pores, constitute a relatively minor part of the pore system and are isolated from each other by the micropores in the micritic matrix (Fig. 4b). As a result, permeabilities are anomalously low (generally less than 40 mD) compared to the high porosity values (20% to 28%) and recovery efficiencies are also expected to be low.

The Khalifa limestone also has a pore system dominated by micropores, with isolated molds and vugs (Fig. 4c).

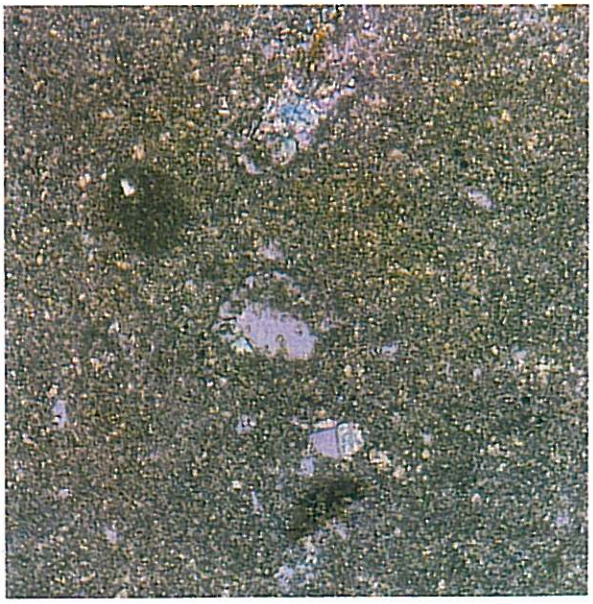


FIG. 4a. Thin section photomicrograph of the Zelten Porosity Zone in the South Nasser Reservoir, Libya, showing a pore system dominated by intercrystalline microporosity.

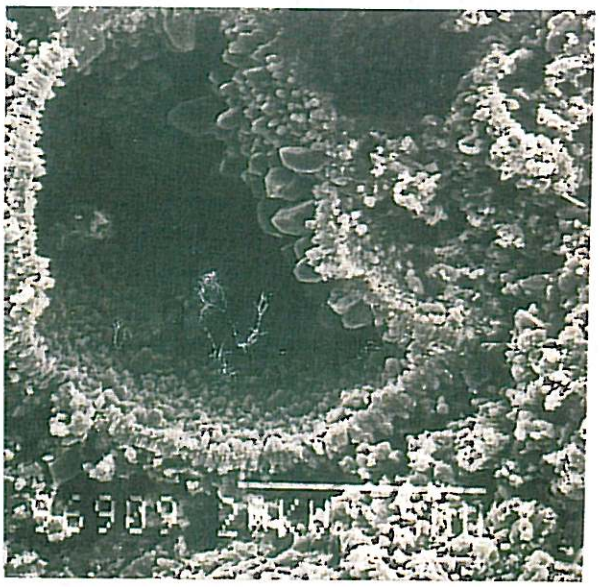


FIG. 4b. SEM view of intraparticle vugs within a foram test. Note the microporous intercrystalline porosity surrounding the vugs.



FIG. 4c. The Khalifa limestone also has a pore system dominated by micropores with isolated molds and vugs.

DRILL CUTTINGS

To an ever increasing extent, drill cuttings form the basis for reservoir quality and fluid sensitivity studies. This is an encouraging sign, suggesting that more and more geologists realize the value of these tiny pieces of reservoir.

Unlike cores, which only represent a small section of the wellbore, drill cuttings are usually caught over most productive zones. In addition, while only about one in three wells are cored, drill cuttings are caught

on most wells. It is easy to see that humble drill cuttings hold a lot of potential.

A wealth of extremely useful information can be obtained from thin sections and scanning electron microscopy (SEM) examination of drill cuttings. This includes: framework mineralogy; diagenetic mineral suite; clay component; pore types and much more. In many cases, permeability and core analysis porosity can be empirically derived from cuttings by comparing them to data from adjacent cores.

Preparing thin sections from drill cuttings is relatively quick and easy. The initial step involves the selection or "highgrading" of cuttings assumed to be representative of the reservoir section. This is accomplished by using a binocular microscope, a good pair of tweezers and a pair of "sharp" eyes. Approximately twelve to fifteen drillchips are placed on a glass slide, impregnated with blue epoxy and ground to a thickness of 30 microns. SEM preparation requires selection of representative drill chips, mounting on an aluminum stub and gold coating prior to examination.

In general, cuttings represent the more competent, better cemented part of the reservoir; the proportion of diagenetic cements is anomalously high and porosity values are conservative with respect to the situation in the reservoir. As a consequence, the accuracy of porosity and permeability determinations based on drill cuttings is highly dependent on the experience of the interpreter.

Empirical derivation of permeability and core analysis porosity from drill cuttings can be accomplished by comparing data from drill cutting thin sections (Figs. 5a and 5b) with thin sections from an adjacent and equivalent cored zone.

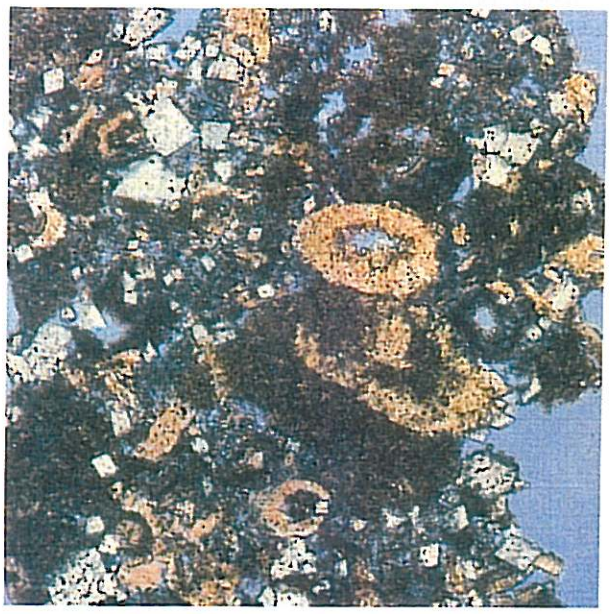


FIG. 5a. Thin section photomicrograph of a peloidal echinoderm grainstone drill cutting in the initial stage of dolomitization.

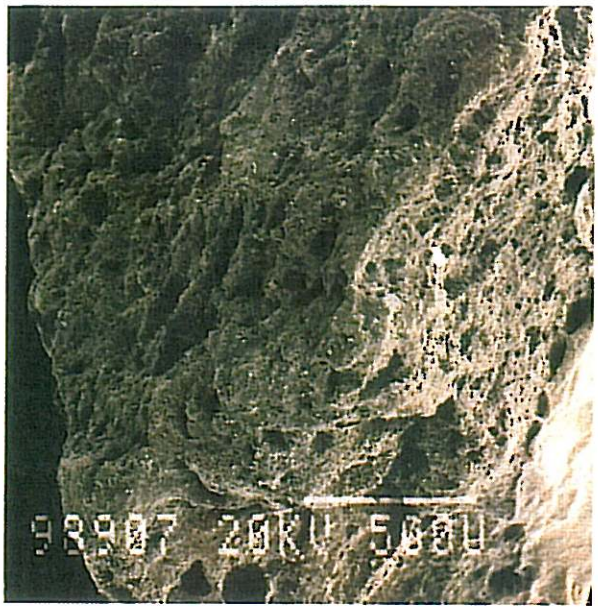


FIG. 5b. SEM view of a dolomite drill chip with isolated micro-vuggy porosity.

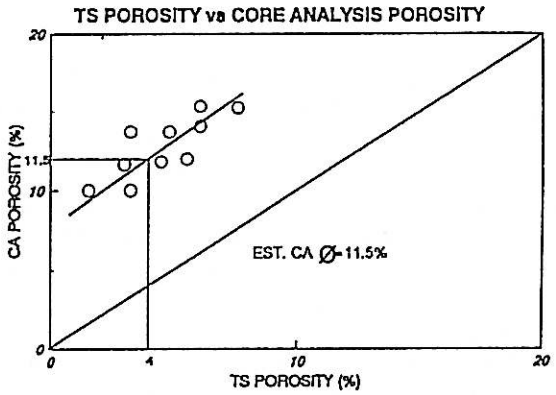


FIG. 5c. Thin section data from an adjacent cored section is plotted to provide a trend line relating core analysis porosity to thin section porosity. Core analysis porosity can then be derived by cross-plotting thin section porosity from the drill cuttings.

Core analyses porsity and permeability will be available for the thin sections prepared from core. These parameters can be plotted against thin section porosity which is obtainable from the drill cutting thin sections.

Initially, core analysis porosity is plotted against thin section porosity for the cored section to derive a trend line relating the two parameters (Fig. 5c). Thin section porosity for the drill cutting samples is then plotted to the trend line to obtain an equivalent core analysis porosity.

The empirical core analysis porosity for the drill cuttings (checked against log porosity for accuracy) is then plotted to the trend line relating per-

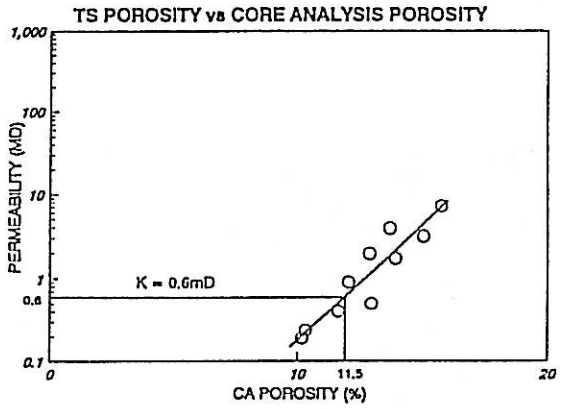


FIG. 5d. The empirical core analysis porosity derived from the drill cuttings (check against log porosity for accuracy) is then cross-plotted to provide permeability for the drill cuttings.

meability and core analysis porosity (Fig. 5d) to provide an empirical permeability value for the drill cuttings.

SUMMARY

Reservoir Quality analysis, incorporating thin section petrography, scanning electron microscopy and X-ray diffraction techniques, is very useful for predicting potential fluid sensitivity problems within reservoirs. These potential problems include fines migration (Messla Field Sandstone), acid sensitivity (Khalifa Formation) and swelling clays. Also, distinguishing between effective and non-effective porosity (Khalifa and Zelten Formations) can be accomplished using thin section petrography. Determining the propotion of effective porosity within a reservoir is obviously important with respect to reserves, sweep efficiency, recovery efficiecy, etc.

Thin section and SEM examination of drill cuttings is very useful for determining reservoir quality and fluid sensitivity of prospective reservoirs. Framework mineralogy, diagenetic mineral suite, pore types, permeability and core analysis porosity can often be derived from drill cuttings.

REFERENCES

AGAT Laboratories., 1983, Reservoir Sensitivity and Completion Procedures Project.

Economides, M.J. and Nolte, K.G., 1989, Reservoir Stimulation, 2nd Ed., Schlumberger Educational Services, Prentice Hall.

Gabriel, G.A., Inamdar, G.R, Oct. 1988, "An Experimental Investigation of Fines Migration in Porous Media", SPE 12168.

Gray, D.H. and Rex, R.W., 1966, Formation Damage in Sandstone Caused by Clay Dispersion and Migration. Clay and Clay Minerals, v. 26.

Hendrickson, A.R. and Smith, C.F., Feb. 1965, "Hydrofluoric Acid Stimulation of Sandstone Reservoirs, JPT.

Johnson, A.L. and Norton, F.H., 1941, Mechanism of Deflocculation in Clay – Water Systems. J.Am.Cer.Soc., v. 24.

Khiler, K.C., Fogler, H.S. and Ahlawalia, J.S., 1983, "Sandstone Water Sensitivity. Existence of a Critical Rate of Salinity Decrease", Chem. Eng. Sci.

Muecke, T.W., April 1979, "Formation Fines and Factors Controlling their Movements in Porous Media", JPT.

Mungan, N., "Permeability Reduction Through Changes in pH and Salinity", SPE 1283, (October 1965).

Pittman, E.D., 1979, Porosity, Diagenesis and Productive Capability of Sandstone Reservoirs. SEPM Sp. Pub. 26, p. 159–173.

Porter, K.E., 1989, An Overview of Formation Damage, JPT.

Selby, R.J. and Ali, S.M.F., 1988, Mechanics of Sand Production and the Flow of Fines in Porous Media. JCPT.

Smith, C.F. and Hendrickson, A.R., Feb. 1965, "Hydrofluoric Acid Stimulation of Sandstone Reservoirs", JPT.

Smith, C.S., Ross, W.M. and Hendrickson, A.R., Oct. 3–6, 1965, "Hydrofluoric Acid Stimulation Development for Field Applications", paper SPE 1284 presented at the SPE Annual Fall Meeting, Denver.

Smith, C.F., Crowe, C.W. and Noland, T.J., Sept. 1969, "Secondary Deposition of Iron Compounds Following Acidizing Treatments, JPT.

Wardlaw, N.C. and Cassan, J.P., 1979, Oil Recovery Efficiency and the Rock – Pore Properties of some Sandstone Reservoirs, Bul. Can. Petrol. Geol., v. 27, no. 2, p. 117–138.

PRJ, Vol. 6 (January 1994); P. 85–90, 3 FIGS, 5 TABLES.

BIOREMEDIATION OF TERESTRIAL FUEL SPILLS

I. Ahmad*, M. Gaja* and N. Kumar*

الإصلاح البيولوجي للتربة من الوقود المنسكب

إفتخار أحمد ، مصطفى قاجة و ن . كومار

إن تصدع الأنابيب وإنهيار الخزانات وغير ذلك من عمليات الإنتاج وكذلك حوادث التخزين والنقل تلوث التربة بالهيدروكاربونات ، وأحياناً على نطاق واسع . يلفت الإصلاح البيولوجي حالياً الكثير من الإنتباه كتقنية إصلاحية .

تهدف الدراسة إجراء تجارب في نطاق المختبر لمعرفة أي منسكب من الوقود يمكن تنظيفه بعملية معالجة للتربة بالاصلاح البيولوجي وبسعر اقتصادي .

إن المعالجة بالإصلاح البيولوجي تتكون من تعديل الرقم الهيدروجيني للتربة ومن ثم تسميدها وفلاحتها . وقد تم تقييم فعالية الإصلاح البيولوجي ، في نطاق المختبر ، على تنظيف التربة من الملوثات كوقود الطيران ووقود الديزل والوقود الثقيل . المتغيرات العملية هي درجة حرارة الإحتضان واللامعالجة والمعالجة بالإصلاح البيولوجي ومراقبة التبخر السام .

تم تحديد المتبقى من الهيدروكربونات باستخدام كروماتوغرافيا الغاز وفي حالة الوقود الثقيل بطريقة تحديد الوزن المتبقى .

لقد تم الحصول على قيم النقاط الخمس الموجودة على المنحنيات من التغيرات العملية المذكورة آنفاً . إن نواتج التقطير الوسطي ووقود الطيران ووقود الديزل المتزايدة مع الإستمرارية تستجيب للمعالجة بالإصلاح البيولوجي تحت شروط التجربة العملية .

بفضل المعالجة بالإصلاح البيولوجي يمكن تخفيض مستوى التلوث الهيدروكاربوني للتربة إلى أدنى مستوى في فترة موسم زراعي واحد .

ABSTRACT

Pipeline rupture, tank failures and various other production, storage and transportation accidents create hydrocarbon contaminated soils, occasionally on a large scale. Bioremediation is currently attracting a lot of attention as a remedial technique. This study is designed to test, on the laboratory scale, what type of fuel spills could be cleaned up by a cost-effective bioremediation approach based on a land treatment process.

A bioremediation treatment that consisted of pH adjustment of soil, fertilisation, and tilling was evaluated on the laboratory scale for its effectiveness in cleaning up a soil contaminated by jet fuel, diesel oil, or heavy fuel oil. Experimental variables included; no treatment, incubation temperature, bioremediation treatment, and poisoned evaporation controls. Hydrocarbon residues were determined by gas chromatography or, in the case of heavy fuel oil, by residual weight determination. Five-point depletion curves were obtained for the prescribed experimental variables. The medium distillates, jet fuel and diesel oil increased in persistence in the listed order but responded well to bioremediation treatment under test conditions. With bioremediation treatment, it is possible to reduce hydrocarbons to insignificant levels in contaminated soils within one growing season.

*Petroleum Research Centre, P.O. Box 6431, Tripoli, G.S.P.L.A.J.

INTRODUCTION

Pipeline rupture, tank failures and various other production, storage and transportation accidents create hydrocarbon contaminated soils, occasionally on a large scale. Soil that is accidentally contaminated by petroleum fuel spills is classified as hazardous waste [1]. Hydrocarbon contaminated soil fails to support plant growth and is a source of ground water contamination. The currently accepted cleanup and

disposal method, by excavation and incineration or transport and burial of the soil secure chemical landfills, is prohibitively expensive when large amounts of soil are involved. This often results in cleanup delays while the contaminated soil continues to pollute scarce ground water resources [2].

Bioremediation is currently attracting a great deal of attention as a remedial technique. This is because other techniques, by themselves, are either inadequate, do not permanently solve the problem or have the potential to be very expensive. Bioremediation is being evaluated by both industry and the US–EPA as one technology for cleaning up hazardous waste sites. The process usually involves the stimulation of indigenous subsurface microorganisms to degrade chemicals on-site, although there have been cases in which microorganisms with some specialised metabolic capabilities have been added. One advantage of this process is that soil excavation is not required.

This study is designed to test, on the laboratory scale, what type of fuel spills could be cleaned up by a cost effective bioremediation approach based on a land treatment process and optimised for oil sludges [3]. Petroleum hydrocarbon disappearance rates were compared in contaminated but otherwise untreated soil, in bioremediation treated soil, and in soil poisoned in order to suppress biodegradation [4].

EXPERIMENTAL

Fuels

Jet fuel, diesel fuel and heavy fuel oil were selected for use in this study. All fuel products were received from a Libyan refinery. The fuel products were initially characterised and the results are shown in Tables 1 to 4.

Table 1. Analysis of Jet Fuel used in Spill Bioremediation Study

Test Method	Test Description	Result
ASTM D1298	Specific gravity at 15/15°C	0.7969
ASTM D3242	Total acidity, mg KOH/g	0.003
ASTM D1266	Total sulphur, wt.%	0.015
ASTM D1219	Mercaptan sulphur, wt.%	0.0001
ASTM D86	Distillation	
	Initial boiling point, °C	151
	10% Vol. recovered at °C	171
	20% Vol. recovered at °C	178
	50% Vol. recovered at °C	198
	90% Vol. recovered at °C	233
	Final boiling point, °C	250
ASTM D2386	Freezing point, °C	−53
ASTM D445	Viscosity at −20°C, CSt	4.3
ASTM D240	Calorific value, kcal/kg	10987
IP 57	Smoke point, mm	28

Table 2. Analysis of Diesel Fuel Used in Spill Bioremediation Study

Test Method	Test Description	Result
ASTM D1298	Specific gravity at 15/15°C	0.8323
ASTM D445	Kin. viscosity at 37.8°C, CSt	3.48
ASTM D93	Flash point, °C	63
ASTM D97	Pour point, °C	0
ASTM D129	Total sulphur, wt.%	0.27
ASTM D3242	Total acidity, mg KOH/g	0.053
ASTM D86	Distillation	
	Initial boiling point, °C	202
	10% Vol. recovered at °C	260
	20% Vol. recovered at °C	275
	30% Vol. recovered at °C	285
	40% Vol. recovered at °C	294
	50% Vol. recovered at °C	302
	60% Vol. recovered at °C	311
	70% Vol. recovered at °C	321
	80% Vol. recovered at °C	335
	90% Vol. recovered at °C	353
	Final boiling point, °C	365
ASTM D240	Gross calorific value, kcal/kg	10945

Table 3. Analysis of Heavy Fuel Oil Used in Oil Spill Bioremediation Study

Test Method	Test Description	Result
ASTM D1298	Specific gravity at 15/15°C	0.9210
ASTM D129	Total sulphur, wt.%	0.966
ASTM D93	Flash point, °C	94
ASTM D445	Kin. Viscosity at 50°C, CSt	105
ASTM D445	Kin. Viscosity at 82.8°C, CSt	28.6
ASTM D97	Pour point, °C	30
ASTM D482	Ash content, wt.%	0.017
ASTM D1796	Water content, Vol.%	0.15
ASTM D240	Gross calorific value, kcal/kg	10537

Sample Treatment

Soils were selected from the area near to the fuel storage tank form. Soils were freshly collected for each experiment. They were partially but not completely air dried to allow sieving (2 mm diameter openings) for uniform consistency, but without damaging their biological activity. Lime ($CaCO_3$) was added to semidry soil prior to column packing for adjusting [5] the pH to 7.5. The sieved soils were packed into glass columns (outer diameter, 25 mm; length, 250 mm) at the bulk density of cores collected from the field. The resulting columns were 22 mm in diameter, and 150 mm in length. The lower end of the columns were closed with a plug and a closable drain spout. After packing, water was added to the top of the column to adjust the moisture content of the soil to 50% of its holding capacity.

Nitrogen (NH_4NO_3) and phosphorous (K_2HPO_4) fertilisers were added to keep 60 μmol N and 5 μmol of P per gram of soil, respectively. They were dissolved in water that was used for adjusting, moisture

Table 4. Compositional Analysis of Fuel Products Used in the Spill Bioremediation Study

Fuel Product	Class Composition			Carbon Range
Jet Fuel	Saturates 87.7	Olefins 0.0	Aromatics 12.3 (by Vol.%)	C8-C15
Diesel Fuel	Non-Aromatics 81.8		Aromatics 18.2 (by wt.%)	C10-C25
Heavy Fuel Oil	Saturates 74.8	Aromatics 22.1	Polar 3.1 (by wt.%)	Not analysed

content. Soil columns were fed by fuel products on top of the columns and allowing them to infiltrate by gravity flow. The maximal application rate (100 mg per g of soil) was chosen so that it would not result in either fuel or water flowing out from the soil column. The evaporation of water during incubation was compensated by addition of weighed distilled water. Weekly tilling of the soil columns was performed by inserting the stainless steel wire into the soil column 15 times. This treatment was much less effective in aerating the soil than conventional tilling in the fields.

2% mercuric chloride was used as biologically inactive poisoned control to differentiate losses from biodegradative losses [4]. The poisoned controls showed the maximum evaporative loss that may occur under the incubation conditions. However, biodegradation and evaporation compete in the removal of petroleum hydrocarbon. The difference between the loss of hydrocarbons from the poisoned controls and the loss observed in active soil samples strongly underestimates the true contribution of biodegradation.

ANALYTICAL PROCEDURES

For each point of analysis, the fuel in the soil of an entire column was extracted. Jet fuel, diesel oil and heavy fuel oil were soxhelet .extracted by methylene chloride for 6 h. Anhydrous sodium sulphate was added to the extraction of heavy fuel oil which has no highly volatile components, the solvent was evaporated in a preweighed dish, and the residual was determined gravimetrically. Extracts of jet fuel and diesel oil were brought to volume and the extracts were analysed by gas chromatography using the Chrompack Packard Gas Chromatograph model 439 equipped with flame ionisation detector. The column used was 25 m long capillary column packed with Cp-Cil 5CB WCOT. Nitrogen was used as carrier gas. The flow rate of carrier gas was adjusted at 1 ml/min. The temperature of the detector and injection port was maintained at 300°C.

For class separation, jet fuel was separated into saturates, olefins and aromatics using the relevent standard procedure [6]. A jet fuel sample (0.75 ml) was introduced into a glass adsorption column packed with silica gel. The upper small layer of the silica gel contains a mixture of fluorescent dyes. When all the sample has been adsorbed on the gel, isopropyl alcohol was added to desorb the sample and force it down to column. The hydrocarbons were separated according to their adsorption affinities into aromatics, olefins and saturates. The fluorescent dyes were also separated selectively, with the hydrocarbon types and made the boundaries of the aromatics, olefins and saturate zones visible under ultraviolet light.

Diesel fuel was separated into aromatics and non-aromatics by using the standard procedure described in ASTM D2549 method [7]. A weighed amount (10 g) of sample was charged to the top of a glass chromatographic column packed with activated bauxite and silica gel. Normal pentane (150 ml) was added to the column to elute the non aromatics. When all of the non-aromatics were eluted, the aromatic fraction was first eluted by additions of diethyl ether (100 ml), then chloroform (100 ml) and by ethyl alcohol (175 ml). The solvents were completely removed from the extracts and the residues were weighed and calculated as aromatics and non-aromatics fractions of the sample.

For class separation of heavy fuel oil, it was fractionated on a silica gel column. The silica gel (100–200 mesh) was activated at 105°C for 12 h. The glass column (2 by 28 cm) was packed with silica gel suspended in hexane. The 0.5 g hydrocarbon samples were adsorbed on 3 g of silica gel and placed on the column. A 3 g layer of anhydrous sodium sulphate was placed over the sample to absorb any water and to prevent the disturbance of the sample with the solvents. The class fractions of heavy fuel oil was accomplished by successive elution in a discontinuous solvent gradient of increasing polarity. The saturated, aromatic, and asphaltic classes were eluted with 120 ml of hexane, benzene, and chloroform-methanol (1:1; vol./vol.), respectively.

RESULTS AND DISCUSSION

The studies generated a five-point depletion curve for each fuel type under a variety of incubation conditions (untreated soil, bioremediation treated soil, poisoned soil). The disappearance pattern of fuel hydrocarbons are shown in Figs. 1 to 3. Although the classical pattern of material depletion shows exponential behaviour but not exactly first order kinetics. Because of diffusion limitations and increase in the degrading microbial populations, the depletion of a homogeneous substrate in soil is rarely a first order but, rather it is an intermediate between first order (exponential) and zero order (linear)

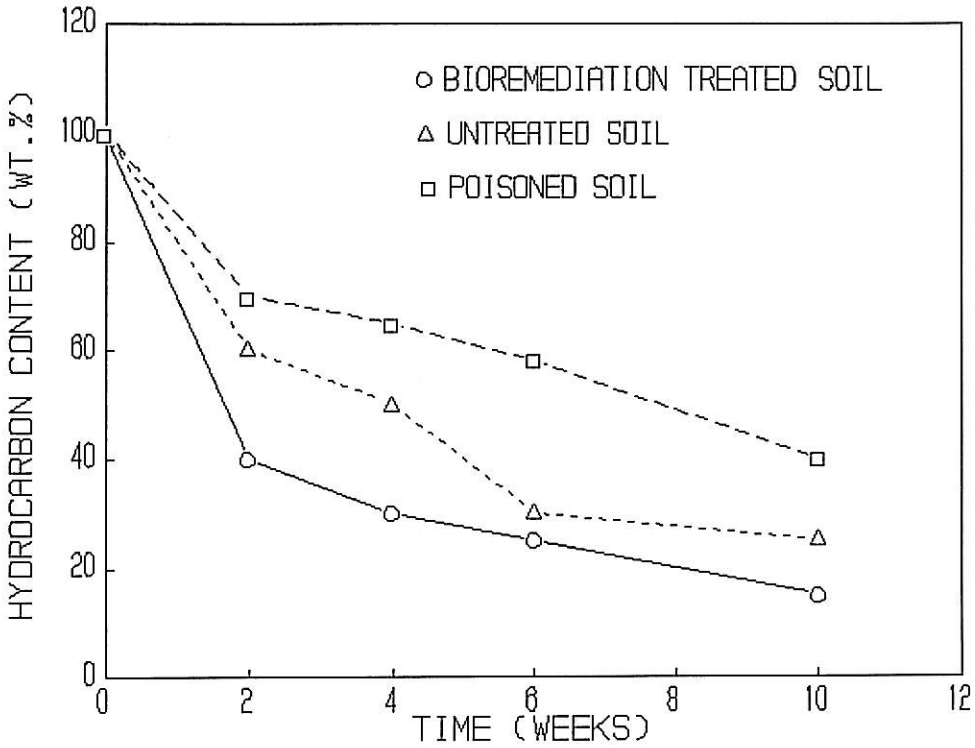


FIG. 1. Disappearance of jet fuel hydrocarbons.

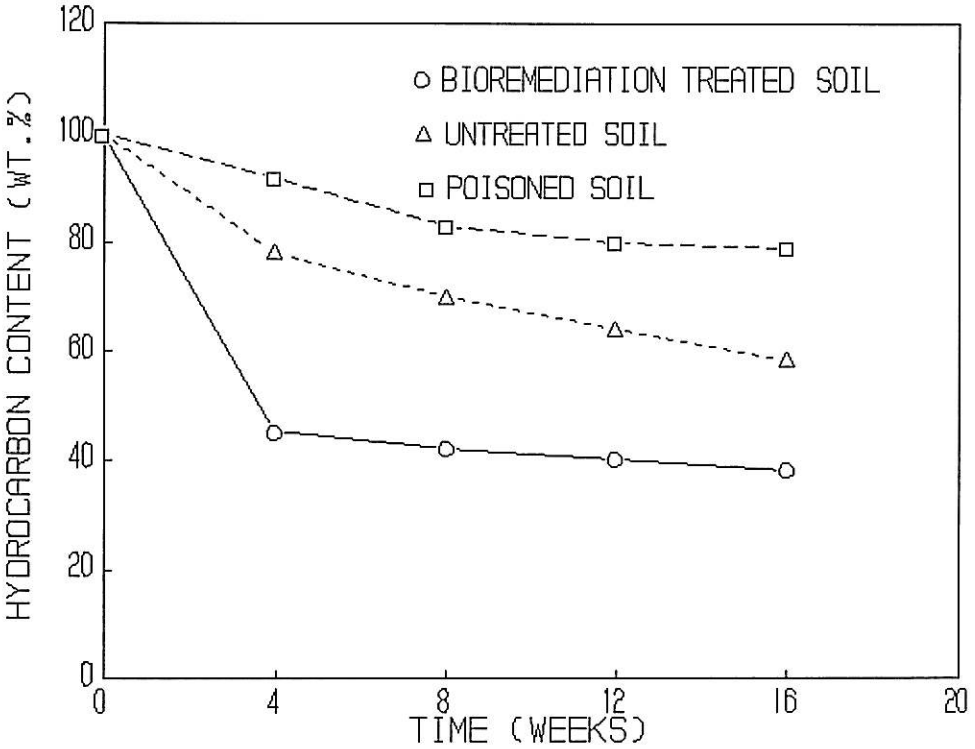


FIG. 2. Disappearance of diesel fuel hydrocarbons.

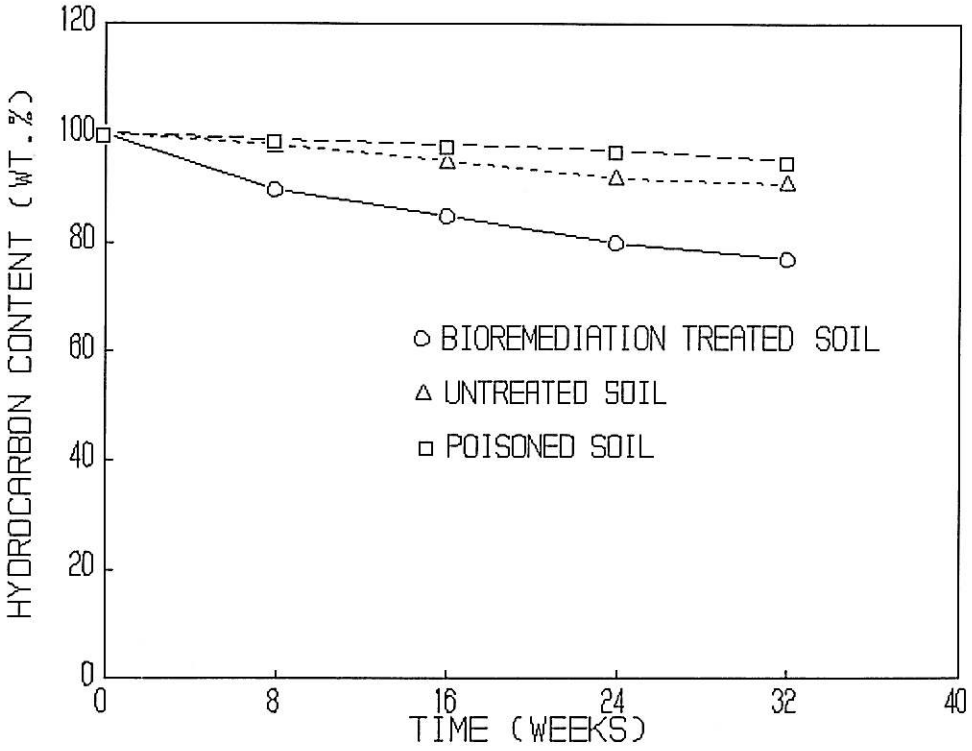


FIG. 3. Disappearance of fuel oil hydrocarbons.

kinetics. The kinetics are further complicated in the case of fuels by the fact that there consist of numerous individual hydrocarbons, each of which degrade at a different rate. The slowing tendency of utilisation is caused not only by substrate depletion but also by the fact that the remaining hydrocarbons are structurally less degradable than the ones already disappeared [8, 9]. To some extent this is compensated by the increasing numbers (enrichment) of the hydrocarbon-degrading microorganisms in the soil with time. For the reasons described above, there is no precise way to convert the curves obtained in this study to constants.

Table 5. Half-Lives of Fuel Disappearance in Soil under Incubation Conditions

Fuels and incubation conditions	Half-life
Jet fuel	
Poisoned soil	7 weeks
Untreated soil	4 weeks
Bioremediation treated soil	1.7 weeks
Diesel Fuel	
Poisoned soil	>16 weeks
Untreated soil	16 weeks
Bioremediation treated soil	3.8 weeks
Heavy Fuel Oil	
Poisoned soil	>32 weeks
Untreated soil	>32 weeks
Bioremediation treated soil	>32 weeks

Table-5 represents the half-lives of fuels under various incubation conditions. The half-life is simply the time needed to reduce the total fuel concentration in soil to 50% of the initial amount. In case of a 50% reduction is not achieved within the time period of the experiment, Table-5 indicates this fact as half-life > 16 weeks. The half-lives used in this table give a useful comparison on the relative biodegradability of the fuels and the environmental conditions that favour or restrict the process.

ACKNOWLEDGEMENT

The authors are grateful to PRC management for providing facilities and encouragement.

REFERENCES

[1] Bartha, R. and Bossert, I., 1984, The treatment and disposal of petroleum refinery wastes, Atlas, R.M., Ed., Petroleum Microbiology, Macmillan, New York, pp. 553–577.

[2] Pye, V.I. and Patrick, R., 1983, Ground water contamination in the United States, Science, 221: 713–718.

[3] Dibble, J.T. and Bartha, R., 1979, The effect of environmental parameters on the biodegradation of oil sludge, Appl. Environ. Microbiol. 37: 729–739.

[4] Pramer, D. and Bartha, R., 1972, Preparation and processing of oil samples for biodegradation studies, Environ. Lett., 2: 217–224.

[5] Pramer, D. and Schmidt, E.L., 1964, Experimental soil microbiology, Burgess Publishing Co., Minneapolis, pp. 6–13.

[6] ASTM D1319, 1990., Standard method of test for hydrocarbon types in liquid petroleum products by fluorescent indicator adsorption, Annual Book of ASTM Standards, Vol. 5.01, pp. 509–514.
[7] ASTM D2549, 1990, Separation of representative aromatics and nonaromatics fractions of high boiling oils by elution chromatography, Annual Book of ASTM Standards, Vol. 5.02, pp. 252–257.
[8] Bartha, R., 1986, Biotechnology of petroleum pollutants of biodegradation, Microb. Ecol., 12: 155–172.
[9] Bossert, I. and Bartha, R., 1984, The fate of petroleum in the soil ecosystem, Atlas, R.M., Ed., Petroleum Microbiology, Macmillan New York, pp. 435–473.

PRJ, Vol. 6 (January 1994); P. 91–95, 1 FIG, 3 TABLES.

Short Note

EFFECT OF THE GRAVITY SEDIMENTATION AND CHEMICAL PRECIPITATION ON THE CONCENTRATION OF HEAVY METALS IN THE REFINERY EFFLUENT

M.A. Khawaja*, M.N. Oun* and S. Alosta*

تأثير التراكم التثاقلي والترسب الكيميائي على تركيز المعادن الثقيلة في منصرف معامل التكرير

م. خواجة ، م. ن. عون و شعبان الأسطى

تم تقدير تركيز المعادن الثقيلة في منصرف معامل التكرير بواسطة جهاز طيف الإمتصاص الذري. كما إختبرت معملياً بعض المخثرات الكيميائية — مثل أكسيد الكالسيوم وحامض الكبريتيك وكبريتات الألومنيوم المائية — لدراسة كفاءتها على الحد من تركيز المعادن الثقيلة في المنصرف المعنى. وجد أن إضافة أكسيد الكالسيوم أو كبريتات الألومنيوم المائية بتركيز 500 جزئ/المليون ثم ترك عينات المنصرف لمدة 24 ساعة للسماح بترسب المادة المخثرة ، قد أدى إلى خفض تركيز المعادن الثقيلة بنسبة أكبر من التراكم التثاقلي على حدى. إضافة حامض الكبريتيك أدى إلى خفض تركيز الحديد والكروم والنحاس ، بينما كان التأثير معاكس بالنسبة للنيكل والخارصين والرصاص.

INTRODUCTION

Some of the heavy metals are among the list of harmful elemental substances, such as iron, chromium, copper, nickel, lead and zinc. These elements can be found in the industrial discharge, such as refinery effluent.

Our study mainly concentrates in locating suitable, easily available and economical precipitating agents and determining their optimal concentration in which they can be used to achieve the maximum efficiency, regarding the reduction of percentage concentration of metallic constituents in the refinery effluents or in other industrial discharges.

Concentration of heavy metals in the refinery effluent were estimated by using Atomic Absorbtion Spectrometric Technique. Some known chemical coagulants were tested to estimate their efficiency for reduction the heavy metals level in the effluent. These are calcium oxide, sulphuric acid and aluminium sulphate octadecahydrate. It was found that the calcium oxide or hydrated aluminium sulphate, when added in the refinery effluent, in the concentration of 500 ppm as coagulant and simultaneous sedimentation for a period of 24 hours, reduced the percentage concentration of the contained heavy metals more than the reduction caused by the sedimentation alone. In case of sulphuric acid, reduction in concentration of iron, chromium and copper have been obtained while it has an opposite effect with nickel, zinc and lead metals. All experiments were carried out at laboratory scale.

*Petroleum Research Centre, P.O. Box 6431, Tripoli, G.S.P.L.A.J.

EXPERIMENTAL WORK

(a) Reagents and Materials

(i) Purity of reagents; the following chemicals of the ACS grade conforming to specifications of the Committee on Analytical Reagents of the American Chemical Society were used: concentrated hydrochloric acid, concentrated nitric acid, concentrated perchloric acid, concentrated ammonium hydroxide

(contains 30% ammonia), 8-hydroxyquinoline, diphenylthiocarbazone, methylisobutylketone and carbon tetrachloride.

(ii) Distilled water, conforming to the specification given in the ASTM standard (Roberta, 1988) was used throughout this work.

(b) Sampling and Preservation

Samples of the effluent for the above study were collected on three different days from the final discharge of the oil refinery, in 2.5 litres capacity, clean amber coloured bottles. 6 ml of concentrated HCl was added for adjusting the pH of the effluent to below 2. At this pH, metals remain in soluble form.

(c) Sample Analysis

Every time ten portions of effluent, 400 ml each, from the effluent samples were transferred into ten 500 ml capacity volumetric flasks identified as A1, A2, A3, A4, A5, A6, A7, A8, A9 and A10. Samples A1, A6 were analysed immediately for the estimation of heavy metals.

It was found that the samples contain Fe, Cu, Ni, Zn, Pb and Cr in the concentration, given in Tables (1–3). Samples A2, A7 were analysed for the estimation of the above mentioned metals, after a sedimentation period of 24 hours. 200 mg calcium oxide was added to samples A3 and A8, 200 mg concentrated sulphuric acid was added to samples A4 and A9, and 200 mg hydrated aluminium sulphate was added to samples A5 and A10. After proper mixing, the samples were stored for 24 hours, to allow the settlement of any coagulated material. After expiry of the sedimentation period the supernatant liquid portions were analysed for the estimation of heavy metals. The same procedures were followed to analyse samples collected on other days, to evaluate the aggregation effect of the precipitating agents on the identified metal ions. The following Standard Procedures were used, for digestion, chelation, solvent extraction and estimation of content.

(*i*) *Digestion*

20 ml of HNO_3 and $HClO_4$ mixture in the ratio of (3:1) was added to each 200 ml of the supernatant fluid of the above prepared samples. All the samples were heated to boiling point and kept at the same temperature until the volume was reduced to 20 ml. After cooling, the mixture was diluted by the addition of 50 ml of distilled water. The pH of the samples Al to A5 was adjusted to 6 by adding diluted HCl and HNO_3, to estimate Fe, Cu, Ni, Zn and Pb. The pH of samples A6 to A10 was adjusted to 2, to estimate Cr.

(*ii*) *Chelation and solvent extraction*

For the treated samples (A1 to A5), 10 ml of 1% solution of 8-hydroxyquinoline was added with constant shaking. The chelated samples were transferred to a separatory funnel and extracted with three portions of 10 ml methylisobutylketone. The combined organic extracts were evaporated to dryness and the residue was dissolved in 20 ml of distilled water. The resulting solution was filtered to remove any undissolved precipitate. Similarly in each digested sample (A6 to A10), 10 ml of 1% solution of diphenylthiocarbazone was added with constant stirring, and the resultant chelated samples were extracted with three portions of 10 ml carbon tetrachloride. The combined organic extracts were treated similarly.

(d) Identification and Estimation of Contained Metals

The above prepared solutions were analysed by Atomic Absorbtion Spectrophotometer. The change in the concentration of the contained metals, either by sedimentation alone or with the addition of the above mentioned precipitating agents and simultaneous sedimentation, for the period of 24 hours, were computed and summarized in Tables 1–3 and elaborated in Fig. 1.

RESULTS AND DISCUSSION

As discussed above, calcium oxide, sulphuric acid and hydrated aluminium sulphate were used as precipitating agents. The metal ions are present in the aqueous solution (effluent) in soluble or suspended form. The precipitating agents adsorb these microfine metal particles on their surface and settle under gravitational force. It was found that by addition of calcium oxide in the concentration of 500 ppm, in the refinery effluent and simultaneous sedimentation of the same effluent, for the period of 24 hours reduced the percentage concentration of iron, chromium, copper, nickel, zinc and lead approximately to 96, 48, 82, 52, 92 and 94 wt.% repectively. Reduction by the sedimentation alone was only 62, 21, 57, 18, 49 and 53 wt.% respectively. So, the addition of calcium oxide further decreased the concentration by 34, 27, 25, 34, 43 and 41 wt.% respectively.

On the other hand the addition of hydrated

Table 1. Effect of Aluminium Sulphate Octadecahydrate, Calcium Oxide and Sulphuric Acid on Precipitation of Iron and Chromium Present in the Refinery Effluent. Concentration was Estimated after 24 Hours Sedimentation

Sample No.	Metal content in ppm					Reduction in metal concentration, in samples type A,B,C, and D, in wt%.			
	In fresh samples	In sedimented samples containing no chemical coagulant (Samples A)	In sedimented samples containing 500 ppm CaO (Samples B)	In sedimented samples containing 500 ppm H_2SO_4 (Samples C)	In sedimented samples containing 500 ppm $Al_2(SO_4)_3.18H_2O$ (Samples D)	(A)	(B)	(C)	(D)
Fe 1	0.35	0.14	0.01	0.13	0.02	60.00	97.14	62.86	94.29
2	0.52	0.20	0.02	0.19	0.03	61.54	96.15	63.46	94.23
3	0.35	0.13	0.01	0.13	0.02	62.86	97.14	62.86	94.29
4	0.51	0.19	0.02	0.19	0.03	62.75	96.08	62.75	94.12
5	0.53	0.20	0.02	0.20	0.03	62.26	96.23	62.26	94.34
6	0.45	0.17	0.02	0.17	0.02	62.22	95.56	62.22	95.56
Average:	(0.45)	(0.17)	(0.02)	(0.17)	(0.03)	(61.94)	(96.38)	(62.74)	(94.47)
Stand. dev.	(+0.19)	(+0.03)	(+0.01)	(+0.03)	(+0.01)	(+1.06)	(+0.63)	(+0.46)	(+0.54)
Cr 1	0.34	0.27	0.18	0.24	0.13	20.59	47.06	29.41	61.76
2	0.36	0.29	0.19	0.26	0.13	19.44	47.22	27.78	63.89
3	0.34	0.27	0.18	0.24	0.13	20.59	47.06	29.41	61.76
4	0.36	0.29	0.19	0.26	0.13	19.44	47.22	27.78	63.89
5	0.35	0.27	0.18	0.25	0.13	22.86	48.57	28.57	62.86
6	0.36	0.27	0.18	0.24	0.13	25.00	50.00	33.33	63.89
Average:	(0.35)	(0.28)	(0.18)	(0.25)	(0.13)	(21.32)	(47.86)	(29.38)	(63.01)
Stand. dev.	(+0.01)	(+0.01)	(+0.01)	(+0.01)	(+0.00)	(+2.19)	(+1.20)	(+2.07)	(+1.05)

Table 2. Effect of Aluminium Sulphate Octadecahydrate, Calcium Oxide and Sulphuric Acid on Precipitation of Copper and Nickel Present in the Refinery Effluent. Concentration was Estimated after 24 Hours Sedimentation

Sample No.	Metal content in ppm					Reduction in metal concentration, in samples type A,B,C, and D, in wt%.			
	In fresh samples	In sedimented samples containing no chemical coagulant (Samples A)	In sedimented samples containing 500 ppm CaO (Samples B)	In sedimented samples containing 500 ppm H_2SO_4 (Samples C)	In sedimented samples containing 500 ppm $Al_2(SO_4)_3.18H_2O$ (Samples D)	(A)	(B)	(C)	(D)
Cu 1	0.38	0.16	0.07	0.15	0.04	57.89	81.58	60.53	89.47
2	0.11	0.05	0.02	0.04	0.01	54.55	81.82	63.64	90.91
3	0.38	0.16	0.06	0.15	0.04	57.89	84.21	60.53	89.47
4	0.44	0.19	0.08	0.18	0.05	56.82	81.82	59.09	88.64
5	0.45	0.19	0.08	0.18	0.05	57.78	82.22	60.00	88.89
6	0.46	0.20	0.08	0.18	0.05	56.52	82.61	60.87	89.13
Average:	(0.37)	(0.16)	(0.07)	(0.15)	(0.04)	(56.91)	(82.38)	(60.76)	(89.42)
Stand. dev.	(+0.30)	(+0.06)	(+0.02)	(+0.06)	(+0.03)	(+1.30)	(+1.05)	(+1.53)	(+0.80)
Ni 1	0.46	0.37	0.22	0.46	0.37	19.57	52.17	Nil	19.57
2	0.56	0.46	0.27	0.56	0.45	17.86	51.79	Nil	19.64
3	0.32	0.26	0.15	0.32	0.26	18.75	53.13	Nil	18.75
4	0.29	0.24	0.14	0.29	0.24	17.24	51.72	Nil	17.24
5	0.28	0.23	0.13	0.28	0.23	17.86	53.57	Nil	17.86
6	0.31	0.25	0.15	0.31	0.25	19.35	51.61	Nil	19.35
Average:	(0.37)	(0.30)	(0.18)	(0.37)	(0.30)	(18.44)	(52.33)	(–)	(18.74)
Stand. dev.	(+0.11)	(+0.09)	(+0.06)	(+0.11)	(+0.09)	(+0.93)	(+0.82)	(–)	(+0.99)

Table 3. Effect of Aluminium Sulphate Octadecahydrate, Calcium Oxide and Sulphuric Acid on Precipitation of Zinc and Lead Present in the Refinery Effluent. Concentration was Estimated after 24 Hours Sedimentation

Sample No.	Metal content in ppm					Reduction in metal concentration, in samples type A,B,C, and D, in wt%.			
	In fresh samples	In sedimented samples containing no chemical coagulant (Samples A)	In sedimented samples containing 500 ppm CaO (Samples B)	In sedimented samples containing 500 ppm H_2SO_4 (Samples C)	In sedimented samples containing 500 ppm $Al_2(SO_4)_3.18H_2O$ (Samples D)	(A)	(B)	(C)	(D)
Zn 1	0.62	0.32	0.05	0.47	0.17	48.39	91.94	24.19	72.58
2	0.62	0.32	0.05	0.47	0.18	49.11	91.94	23.81	71.45
3	0.66	0.34	0.06	0.50	0.18	48.48	90.91	24.24	72.73
4	0.68	0.35	0.06	0.52	0.18	48.53	91.18	23.53	73.53
5	0.64	0.33	0.05	0.49	0.17	48.44	92.19	23.44	73.44
6	0.64	0.33	0.05	0.49	0.17	48.44	92.19	23.44	73.44
Average:	(0.64)	(0.33)	(0.05)	(0.49)	(0.18)	(48.57)	(91.73)	(23.76)	(72.86)
Stand. dev.	(+0.18)	(+0.01)	(+0.01)	(+0.02)	(+0.01)	(+1.27)	(+0.55)	(+0.24)	(+0.08)
1	0.88	0.41	0.05	0.57	0.04	53.41	94.32	35.23	95.45
2	0.92	0.43	0.05	0.60	0.04	53.26	94.57	34.78	95.65
3	0.68	0.32	0.04	0.44	0.03	52.94	94.12	35.29	95.59
4	0.68	0.32	0.04	0.44	0.03	52.94	94.12	35.29	95.59
5	0.68	0.31	0.04	0.44	0.03	54.41	94.12	35.29	95.59
6	0.66	0.31	0.04	0.43	0.03	53.03	93.94	34.85	95.45
Average:	(0.75)	(0.35)	(0.40)	(0.49)	(0.03)	(53.33)	(94.20)	(35.12)	(95.55)
Stand. dev.	(+0.12)	(+0.05)	(+0.01)	(+0.08)	(+0.01)	(+0.56)	(+0.22)	(+0.20)	(+0.08)

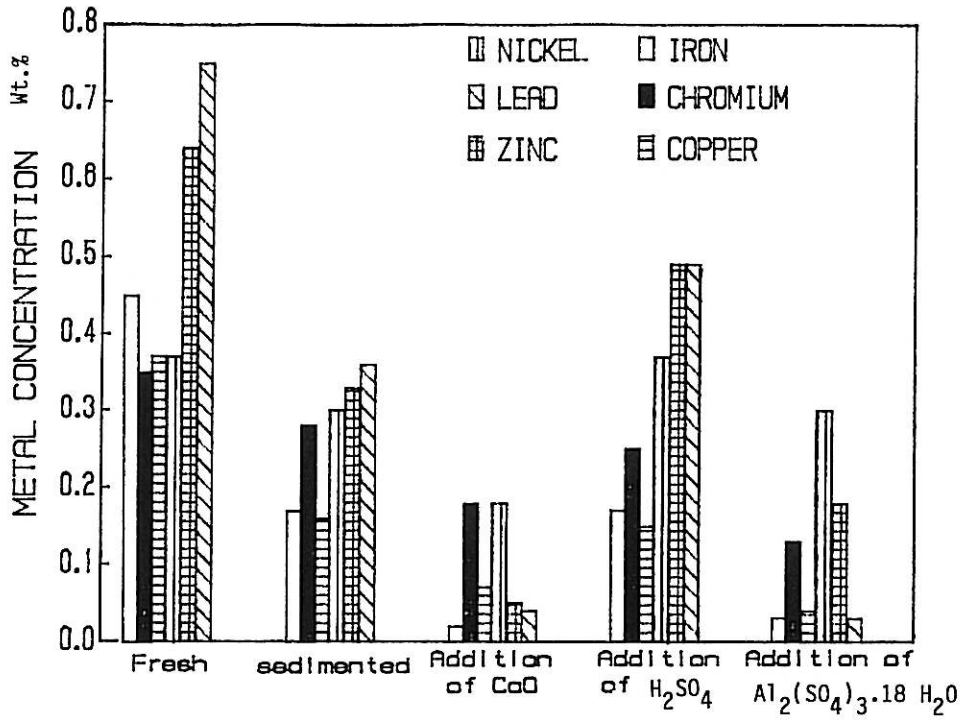


FIG. 1. Reduction of metal concentrations by sedimentation and the addition of coagulants.

aluminium sulphate in the concentration of 500 ppm, in the effluent and simultaneous sedimentation for a period of 24 hours reduced the percentage concentration of these metal ions approximately to 94, 63, 89, 19, 73 and 96 wt.% respectively. The increase in the percentage reduction was calculated to be 32, 42, 32, 1, 24 and 43 wt.% respectively.

The addition of sulphuric acid in the effluent, in a concentration of 500 ppm and simultaneous sedimentation for 24 hours, reduced the percentage concentration of the metals approximately to 63, 29, 61, zero, 24 and 35 wt.% respectively. Further reduction in the percentage concentration of iron, chromium and copper was observed while an oppo-

site effect was found in case of nickel, zinc and lead metals.

Regarding the degradation mechanism, calcium oxide and aluminium sulphate octadecahydrate, upon disolution in aqueous medium, are converted into insoluble hydroxides. These hydroxides act as metal scavangers and adsorb the microfine metal ions from the medium. The following model equations explain the aggregation of metal ions as metal hydroxide. Metal hydroxide in the aqueous medium converts into positive or negative charged particles depending on the pH of the medium, as shown below:

$$M(OH)_n + H^+ \rightarrow [M(OH)_{n-1}(OH_2)]^+$$

$$M(OH)_n - H^+ \rightarrow [M(OH)_{n-1}(O)]^-$$

The postive charged particles of the metal hydroxide assist in aggregating the negative charged metal ion complexes. The negative charged metal hydroxide ion attracts the positive charged metal ions and bring out their sedimentation. Metal ions which carried ligands form bonds with metal hydroxide by displacement of either hydrogen ion or hydroxil ion, depending on the pH of the medium. The possible metal ligand bonding may be as follows:

$$\begin{matrix} M-OH \\ \\ M-OH \end{matrix} \quad + Mt^{z+} \longrightarrow \quad \begin{matrix} M-O \\ \diagdown \\ Mt^{z-2} + 2H^+ \\ \diagup \\ M-O \end{matrix}$$

Mt^{z+} = Metal pollutants

or

$$M(OH)_n + Mt^{z+}L \overset{-H^+}{\rightleftharpoons} M(OH)_{n-1} \cdot OMt^{z-1}L$$

$$M(OH)_n + Mt^{z+}L \overset{+H^+}{\rightleftharpoons} M(OH)_n \cdot HMt^{z+1}L$$

But there is a reversible equilibrium between the metal ions or metal complexes already sorbed by the metal hydroxide and the metal ions or complexes present in the aqueous medium. The change in concentration of any of the species brings change in the concentration of other species in the reaction vessel, as shown below:

$$\begin{matrix} Mt^{z+}\ (\text{sorbed}) & \rightleftharpoons & Mt^{z+}\ (\text{aqueous}) \\ \uparrow\downarrow & & \uparrow\downarrow \\ Mt^{z+}L\ (\text{sorbed}) & \rightleftharpoons & Mt^{z+}L\ (\text{aqueous}) \\ \uparrow\downarrow & & \uparrow\downarrow \\ L\ (\text{sorbed}) & \rightleftharpoons & L\ (\text{aqueous}) \end{matrix}$$

Sulphuric acid acts as precipitating agent only if the medium is able to convert sulphate ions into sulphide ions. These sulphide ions are metal precipitants, which convert metal ions into insoluble metal sulphides. Desulfovibrio bacteria are responsible microorganisms for the conversion of sulphates ions into sulphides ions. From the experimental results, it has been found that the effluent does not contain these bacterias and sulphate ions remain in the medium as such. Due to the high concentration of sulphate ions, metal ions are converted into soluble metal sulphates.

CONCLUSION

It has been proved that calcium oxide and hydrated aluminium sulphate are suitable precipitants for metal ions present in the refinery effluent and can be added in concentration of 500 ppm in the refinery effluent, for reducing the concentration of heavy metal ions, when they exceed the thresh-hold limits. These chemical substances are cheaper and available. They have appreciable efficiency when used in the concentration mentioned.

ACKNOWLEDGEMENT

We thank Petroleum Research Centre Management for their assistance and encouragement and permission to publish this work.

REFERENCES

Al-Khatib, E. and I.I. Esen, 1980, Pollution Control in the Shuaiba Industrial Area in Kuwait. Treatment and Disposal of Liquid and Solid Industrial Wastes, Pergamon Press, p. 369–381.

Al-Meida, S.A.S. and R.G. Ludwig, 1980, Economic Design of Industrial Wastewater Treatment System in Brazil. Treatment and Disposal of Liquid and Solid Industrial Wastes, Pergamon Press, p. 475–484.

Manahan, S.E., 1990, Removal of Heavy Metals, Environmental Chemistry, 4th Edition, Lewis Publisher, Inc., p. 211.

O'Haver, T.C., 1976, Chemical Aspects of Elemental Analysis, Trace Analysis, Spectroscopic Methods for Elements, vol. 46, John Wiley and Sons, Inc. p. 63–77.

Sestini, U., 1980, Assistance to Small Industries in the Treatment of Their Wastewater. Treatment and Disposal of Liquid and Solid Industrial Wastes, Pergamon press, p. 181–187.